# *Technologies for Terahertz Frequency Sensing*

By

William James Otter

A thesis submitted for the Doctor of Philosophy degree and Diploma of Imperial College London

Imperial College London

Department of Electrical and Electronic Engineering

Optical and Semiconductor Devices Group

2015

## *Declaration of Originality*

*I hereby declare that that thesis entitled "Technologies for Terahertz Frequency Sensing", is an original work and any material used from other resources has been appropriately referenced*

*William J. Otter*

*For my family*

## Acknowledgements

Firstly my supervisor Dr. Stepan Lucyszyn, for providing me the opportunity to undertake a PhD and, then guidance, support and ideas he has added to the research I have undertaken.

I would like to thank Val O'Donoghue Charitable Trust which through Val O'Donoghue scholarship in Electrical and Electronic Engineering gave me the financial support to undertake this PhD.

Dr Stephen Hanham and Prof Norbert Klein within the Department of Materials for their help with experimental measurement of devices within their lab as well as the many fruitful research discussions and ideas. Prof. Andrew Holmes for his advice and assistance with the laser experiments. Nick Ridler at the National Physical Laboratory for allowing me to undertake numerous measurement campaigns in the labs at Teddington and teaching me about measurement uncertainty analysis. Dr. Fangjing Hu, Dr. Elpida Episkopu and Dr Stergios Papantonis for the many collaborative projects undertaken which resulted in interesting research ideas and more detailed knowledge of the research challenges. Dr. Werner Karl, Dr Alexey Denisov, Dr. Robert Hergert, Dr. Aifric Delahunty, Dr. Munir Ahmed and Dr. Steven Wright for teaching me how to fabricate structures within the cleanroom facilities. Dr. Marco Ribeiro for hosting me at ISCTE, Lisbon to work on the ongoing collaboration on the creation of THz stress sensors.

I would also like to thank Mark Brewington, Michael Gray and Graham Riley at KEGS for the help, the inspiration and encouragement during my schooling. On a similar note Julian Whybra, James Acton, John Senior and Jim Hind at GIFT for the invaluable lesson that I learnt and many new ideas that challenged my thinking at various courses.

I'd like to thank the LVA and, Prof. Moore and his team at Moorefields Eye Hospital as without their help I would not have been able to undertake this work.

Finally I'd like to thank my parents for always supporting my education, to aim high and not to give up. My sister for doing what sisters do.

## Abstract

Electromagnetic sensors provide information about the environment around us. Historically, THz has been used for astronomy and other scientific insturments. Within this thesis, the aim is to investigate a variety of technologies that have the potential to bring THz technology to a wider market, by creating either low cost devices or technologies that can been monolithically integrated.

Chapter 1 provides an introduction to THz and definitive material equations that underpin the simulations undertaken throughout the thesis. This is necessary as THz engineers and scientists come from a broad range of backgrounds where different definitions are deemed standard.

Chapter 2 looks at the use of plasmonic devices for THz. Initatilly, the proposed spoof plasmon structure is investigated as a benchmark for simulation comparison and, secondly, the use of semiconductor surfaces is studied to create frequency tuneable sensors with highly confined fields.

Chapter 3 moves towards more conventional quasi-optical metal mesh filters for low cost manufacture, comprising a single ultra thin metallic layer on a thick substrate. The chapter concludes with the initial design and simulations of a THz stress sensor based on the metal mesh filter.

Chapter 4 looks into the use of photonic crystal technology. Several state-of-the-art devices are demonstrated: resonators, switches and attenuators. These devices have the potential to provide the building blocks for a future monolithically integrated THz architecture.

# *Table of Contents*

# List of Figures

# List of Symbols

| Symbol | Description |
|---|---|
| $A, M$ | *Arbitrary matrix* |
| $a$ | *Type-A uncertainty* |
| $B$ | *Magnetic flux density* |
| $b$ | *Type-B uncertainty* |
| $\beta$ | *Propagation constant* |
| $c$ | *Speed of light* |
| $D$ | *Electric displacement field* |
| $E$ | *Electric field strength* |
| $E_g$ | *Band gap energy* |
| $e$ | *Euler's number* |
| $\varepsilon$ | *Permittivity* |
| $\varepsilon_{eff}$ | *Effective permittivity* |
| $\varepsilon_0$ | *Permittivity of free space* |
| $\varepsilon_r$ | *Relative permittivity* |
| $\varepsilon_{r,eff}$ | *Effective relative permittivity* |
| $\varepsilon_\infty$ | *Dielectric function at infinite frequency* |
| $f$ | *Frequency* |
| $f_0$ | *Resonant frequency* |
| $f_u$ | *Upper 3 dB cut-off frequency* |
| $f_l$ | *Lower 3 dB cut-off frequency* |
| $f_{0+}$ | *Maximum value at* $f_0$ |
| $f_{0-}$ | *Minimum value at* $f_0$ |
| $\varsigma$ | *Coverage factor* |
| $G$ | *Metal mesh filter lattice constant* |
| $H$ | *Magnetic field strength* |
| $h$ | *Metal mesh filter metal layer thickness* |

| | |
|---|---|
| $h$ | *Planck's constant* |
| $I$ | *Isolation* |
| $J_c$ | *Conduction current density* |
| $J_i$ | *Impressed current density* |
| $J_f$ | *Free current density* |
| $j$ | *Complex operator* |
| $K$ | *Metal mesh filter cross width* |
| $k_{\parallel}$ | *In-plane wave vector* |
| $\kappa$ | *Coupling factor* |
| $L$ | *Metal mesh filter cross length* |
| $L$ | *Linearity* |
| $\lambda_0$ | *Free-space wavelength* |
| $\lambda_R$ | *Resonant wavelength* |
| $\lambda_{Rfree}$ | *Free-space resonant wavelength* |
| $M$ | *Mismatch* |
| $m^*$ | *Effective mass* |
| $\mu$ | *Permeability* |
| $\mu_0$ | *Permeability of free space* |
| $n$ | *Number of samples* |
| $n$ | *Density of charge carriers* |
| $n$ | *Refractive index* |
| $\pi$ | *Pi* |
| $Q_D$ | *Dielectric Q-factor* |
| $Q_0$ | *Unloaded Q-factor* |
| $Q_L$ | *Loaded Q-factor* |
| $Q_{L\omega_0}$ | *Loaded Resonant Q-Factor* |
| $Q_{L\angle}$ | *Loaded Phase Q-Factor* |
| $q$ | *Elementary charge* |
| $R$ | *Random* |

| | |
|---|---|
| $R_s$ | *Surface resistance of a metal* |
| $S_{11}$ | *Forward voltage wave reflection coefficient* |
| $S_{12}$ | *Reverse voltage wave transmission coefficient* |
| $S_{21}$ | *Forward voltage wave transmission coefficient* |
| $S_{22}$ | *Reverse voltage reflection coefficient* |
| $\sigma$ | *Conductivity* |
| $\sigma_{eff}$ | *Effective conductivity* |
| $\sigma_0$ | *Intrinsic DC bulk conductivity* |
| $t$ | *Time* |
| $tan\delta_e$ | *Effective dielectric loss tangent* |
| $\tau$ | *Phenomenological scattering relaxation time* |
| $U$ | *Expanded uncertainty* |
| $u$ | *Standard uncertainty* |
| $\varphi$ | *Dielectric filling factor* |
| $\omega$ | *Angular frequency* |
| $\omega_0$ | *Resonant angular frequency* |
| $\omega_p$ | *Angular plasma frequency* |
| $\omega_{sp}$ | *Angular surface plasmon frequency* |
| $X_s$ | *Surface reactance of a metal* |
| $x, y, z$ | *Cartesian co-ordinate axes* |

# List of Abbreviations

| | |
|---|---|
| 1D, 2D, 3D | Spatial dimensions |
| BCB | Benzocylcobutene |
| CMOS | Complementary metal–oxide–semiconductor |
| DRIE | Deep Reactive- Ion Etching |
| DUT | Device Under Test |
| EM | Electromagnetic |
| FCB | Finite Conductivity Boundary |
| FET | Field Effect Transistor |
| IPA | Isopropanol |
| LED | Light Emitting Diode |
| LIB | Layered Impedance Boundary |
| HRS | High Resistivity Silicon |
| MOS | Metal Oxide Semiconductor |
| MPRWG | Metal-pipe rectangular waveguide |
| NPL | National Physical Laboratory |
| PC | Photonic Crystal |
| PEC | Perfect Electrical Conductor |
| PIMMS | Primary Impedance Microwave Measurement System |
| Q-Factor | Quality Factor |
| QCL | Quantum Cascade Laser |
| QD | Quantum Dots |
| RADAR | Radio Detection And Ranging |
| RAM | Random Access Memory |
| RF | Radio Frequency |

| | |
|---|---|
| RFID | Radio Frequency Identification |
| RLC | Resistor, Inductor and Capacitor |
| SEM | Scanning Electron Microscope |
| SPP | Surface Plasmon Polariton |
| TCP | Thermally Conductive Paste |
| TDR | Time-Domain Reflectometry |
| TE | Transverse Electric |
| THz | Terahertz |
| THz-TDS | Terahertz Time-Domain Spectroscopy |
| TIR | Total Internal Reflection |
| TM | Transverse Magnetic |
| TRL | Through, Reflect, Line |
| VNA | Vector Network Analyser |
| WR | Waveguide Rectangular |
| TOSM | Through, Offset-short, Short, Match |
| VSWR | Voltage Standing Wave Ratio |

# 1 Introduction to Terahertz

This short literature review provides a general introduction to terahertz (THz) technologies, design philosophies and covers material theory that underpins research in later chapters. For the specific technologies investigated in this thesis, a more detailed review covering each device is given at the start of the relevant section.

The THz frequency region is considered to be one of the most underutilized parts of the electromagnetic spectrum. It lies between 0.1 – 10 THz, where the performance of conventional electronics falls off and that of photonics increases, Fig 1. Due to this, it presents novel research challenges and has received increasing interest because of its unique properties. THz radiation is considered safe for humans because it is: non-ionizing, due to the low photon energy; power sources are normally limited to micro/milliwatts; and the depth of penetration does not extend beyond the thickness of human skin [1].

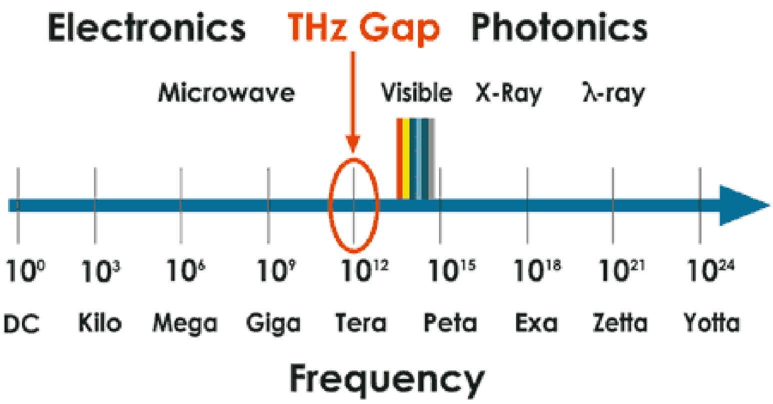


**Figure 1: Electromagnetic Spectrum showing where THz is [2]**

The low THz frequencies of up to 0.6 THz are able to penetrate most non-metallic materials (e.g. clothing and plastics) [3]. This makes it useful for stand-off imaging systems rather than using X-rays, which are a higher energy electromagnetic wave that can ionise molecules. THz waves above 0.6 THz excite molecular and atomic resonances and intra-band electron transitions in materials [4]. These result in frequency-domain “fingerprints”; frequency spectra that enable accurate spectroscopy to be performed on materials of interest, providing information unavailable at other frequencies. An example of this is shown in Fig. 2, where various spectra of explosives at THz frequencies are shown. This characteristic has allowed THz radiation to be useful for non-invasive and non-destructive testing. For example, it has already found its way into a number of civilian applications, including packaging failure analysis [5], quality control [6], food spoilage detection [7], historical art forensics [8] and pollution monitoring [9]. However all of these represent immature technology when compared to optical and RF hardware development. A good example of this seen Fig. 3, where there are three systems that provide a complete front-end system; as the operating frequency moves towards THz the solution becomes bench top scientific instruments.

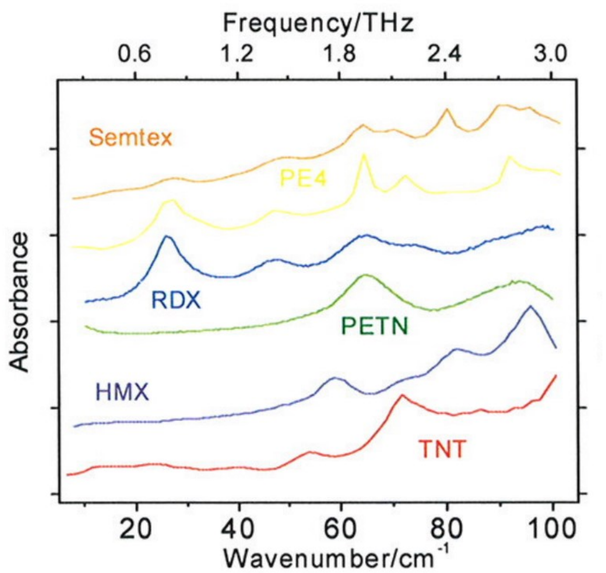


**Figure 2: Example THz spectrum of various explosives [10]**

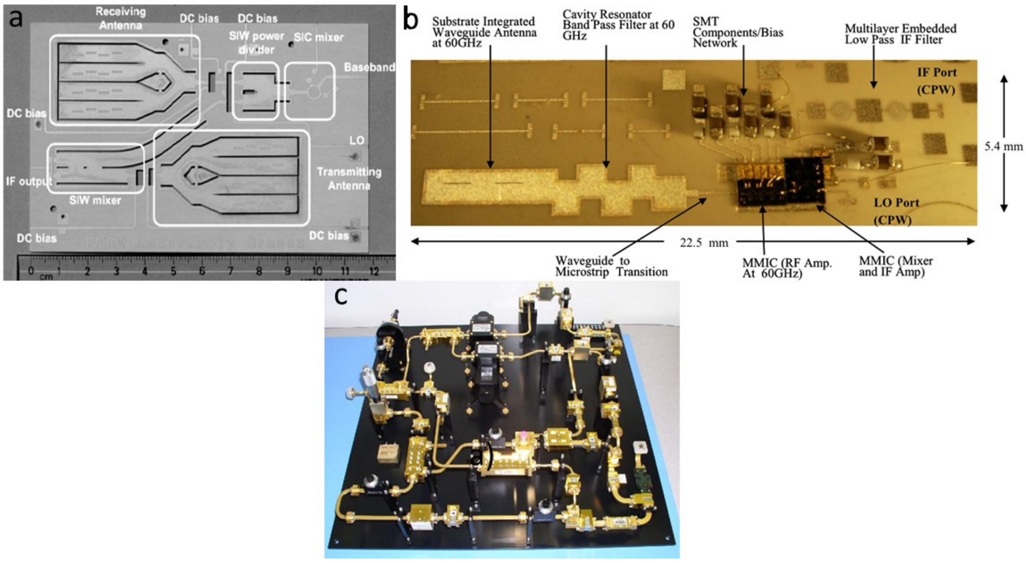


**Figure 3: Example front-end systems. a) 24 GHz Frequency Modulation Continuous-Wave Radar Front-End System-on-Substrate [11]; b) 60-GHz multi-chip module receiver employing substrate integrated waveguides [12]; c) 90 GHz optical bench medical imaging system [13]**

To develop new technologies at THz, we need to understand the historical applications and limitations. THz has been underused as the atmospheric losses are significant, when compared to RF and optical frequencies, as seen in Fig. 4. Also there is a gap in available sources known as the 'THz Gap', shown in Fig. 5. These limitations led to THz radiation being predominantly of just scientific interest, for applications such as astronomy [14].

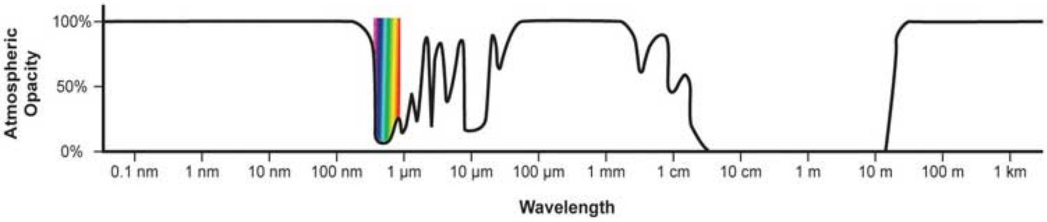


**Figure 4: Atmospheric attenuation of electromagnetic waves across the full frequency spectrum. [15]**

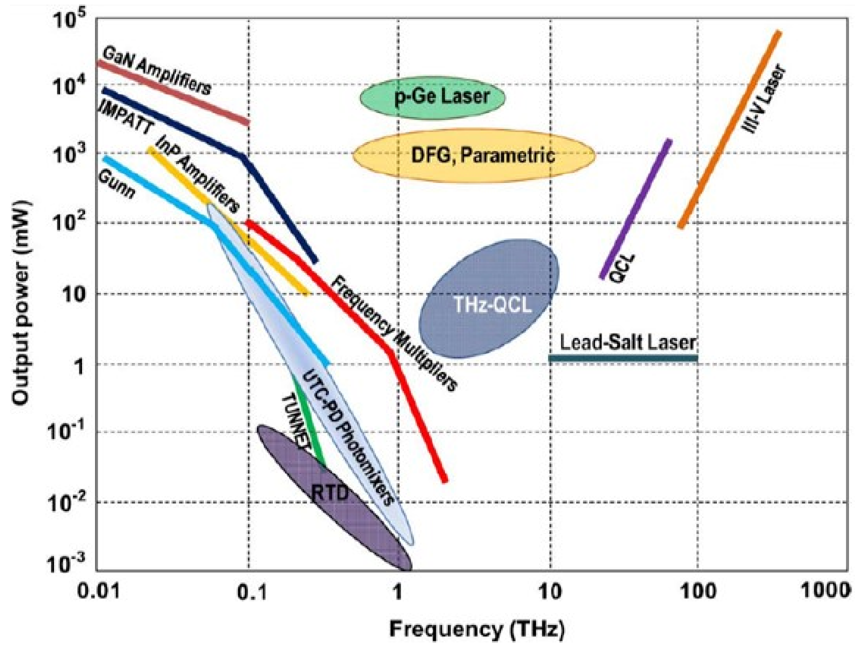


**Figure 5: The 'THz Gap' in sources, as seen by the decreasing output power of sources scaled from optics down in frequency and microwaves up in frequency. [16]**

Today, there is a sustained drive to promote the development of THz technologies and their applications. From the scientific community, new THz sources, detectors and material systems are being investigated, with ever improving performances. For THz sources, solid-state oscillators, amplifiers and frequency multipliers have been steadily increasing in frequency, output power and power efficiency; allowing operation in the lower band THz region [17]-[20]. At high THz frequencies, optical-to-THz down-conversion using photodiodes [21]-[22], photoconductors [23], or nonlinear optical effects [24] have been widely used. Moreover, the use of THz quantum cascade lasers (THz-QCLs) for THz carrier generation is being pursued intensively, ever since the first THz-QCL (operating at 4.4 THz) was demonstrated in 2002 [25]. Indeed, a great deal of effort has been made in reducing the frequency of operation; while also bringing up the working temperature from cryogenic towards room temperature. THz-QCLs can now be developed to cover a wide frequency range (0.84 to 5 THz) and operate at temperatures as high as 200 K [26]-[27].

Real progress has also been made in THz detectors. Here, cost-effective silicon-based field effect transistors (FETs), having submicron gate lengths, are used to sense the plasma frequency in the THz range [28]-[29]. Also, a single-photon THz detector has been invented, utilizing semiconductor quantum dots (QDs); this provides the highest sensitivity of any THz detector [30].

Many groups are currently investigating sources and detectors for THz as this is the key limiting factor for creation of ubiquitous THz devices. There is also some research going on in creating THz devices, including amplitude and phase modulators [31]-[32], spatial light modulators [33], filters [34]-[35] and sensors [36]. However, as with most THz devices, they are still in their infancy for real commercial exploitation. The current commercial market for THz devices is mainly test and measurement systems [36-38] or bespoke one-off systems [40]. There is an emerging trend to start research and development of low-cost THz engineering demonstrators to show the future capability of the technology, as shown by the three examples below, which show some of the unique capabilities of THz.

*A. THz TDR Tags*

There are countless tagging technologies, operating across the whole frequency spectrum, which have been commercially exploited; RFID tags and barcodes are the most common examples. However, their signals can be easily intercepted and reverse engineered. Simple THz engineering offers a new tagging technology, based on time-domain reflectometry, TDR [41]. This approach relies on a stack of dielectric sheets having embedded defects. The defect could be a change in thickness or a sheet with a different dielectric constant, to create a unique TDR 'key signature' response. The main advantage of this technology, over current technologies, is that it is much harder to identify and reverse engineer. Also, unlike RFID tags, they contain no metal and can be easily concealed.

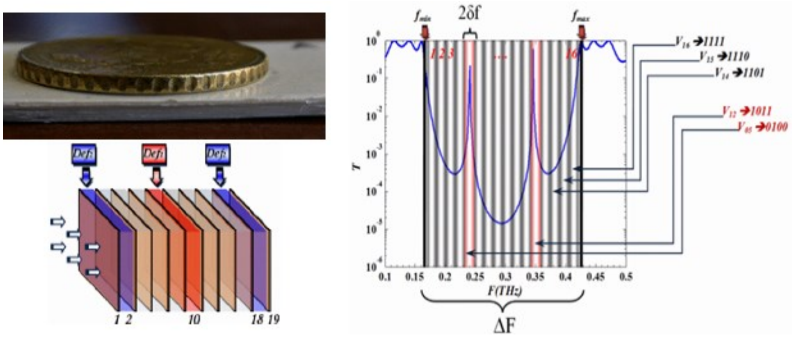


**Figure 6: Illustration of the Tag stack with spatial defects over the corresponding frequency response, showing the encoding capacity of 19 layers [41].**

*B. Handheld THz Time-domain Spectroscopy*

Time-domain spectroscopy has also been a driving application for THz technology. However, most systems are laboratory based and so this limits their potential deployment as a ubiquitous application. However, recent advances have enabled the development of a handheld, battery powered system [42]. This system operates from 0.1 to 2 THz with a >50 dB dynamic range and a standoff detection of 10 cm. This shows that THz systems are becoming mature enough to be deployed outside of the laboratory and yet still perform accurate measurements.

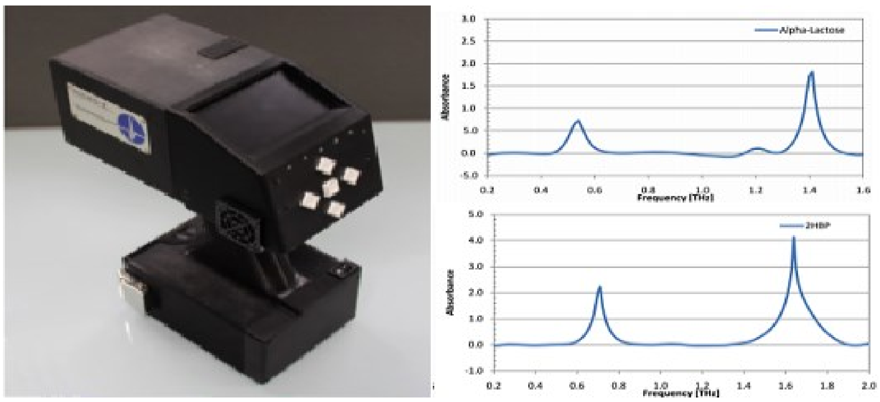


**Figure 7: Handheld THz Spectrometer and example chemical spectra [42].**

*C. Real-time CMOS THz Imagers*

There is considerable interest in developing low-cost security body scanners, for the screening of illegal substances and concealed weapons (e.g. capable of detecting hidden metals, plastic, liquids, gels, ceramics and narcotics concealed beneath a person's clothing). Most work in this area has shown that systems may take minutes to produce images. However, a recently reported THz imager that employs CMOS technology can produce real-time images (e.g. 25 frames per second) [43]. This imager contains 1,000 pixels operating between 0.6 to 1 THz. As CMOS is a mature and relatively low-cost technology, this type of imager could be easily integrated into existing systems for commercial exploitation.

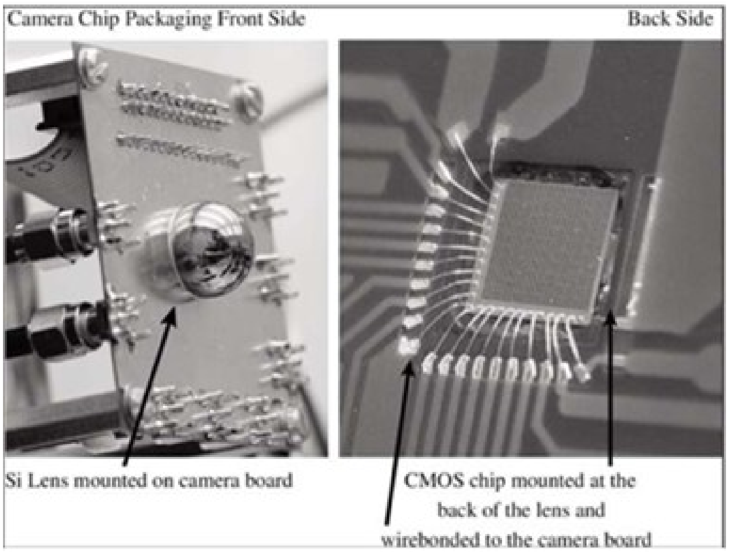


**Figure 8: Real-time CMOS THz imager operating from 0.6 to 1 THz [43].**

To create devices such as those illustrated, THz scientists and engineers have a unique set of tools (and challenges) at their disposal for engineering a solution. Broadly speaking, there are two approaches to every design problem. Firstly, devices can be scaled up in size from optics. The second, rather obvious, approach is to scale microwave components up in frequency and down in size to work at higher frequencies. There are two main problems with frequency scaling device. For example, an X-band MPRWG has an internal cross section of 22.86 mm x 10.16 mm, operating at 8.2 – 12.5 GHz; whereas, a low THz WR 2.2 waveguide, which operates from 0.33 – 0.5 THz is 0.559 mm x 0.279 mm. This means the waveguides are almost two orders of magnitude smaller. However, they are machined using the same technology. This means that losses, due to surface finish and misalignment, are greater as these do not linearly scale down in size. The second problem is the material assumptions made at low frequency, such as modelling metals as PEC, which introduce significant errors if they are applied at a higher frequency, as the material properties are frequency dependent.

## 1.1 Intrinsic and Effective Material Parameters [*J. (2)*]

Dispersion in the conductivity of metal-based structures can affect THz simulation results significantly and, therefore, they have to be properly taken into account when passive components are modelled. There are ambiguities in some definitions, due to the different backgrounds, when researching THz devices. Therefore, the theory that underpins frequency-domain solvers is presented here for unambiguous definition of materials used in models throughout this thesis. Frequency-domain solvers are only considered, as the majority of devices presented in this thesis have narrow spectral responses, making them more accurate to use when compared to time-domain solvers.

The relevant background to defining material parameters for frequency dispersive media starts with the generalised Ampere's law (where the associated variables have their usual meaning):

$$\nabla \times \boldsymbol{H} = \boldsymbol{J}_f + \frac{\partial \boldsymbol{D}}{\partial t} \tag{1}$$

where $\boldsymbol{J}_f = \boldsymbol{J}_i + \boldsymbol{J}_c$. Assuming that the impressed (external) current density $\boldsymbol{J}_i$ is zero, the free current density $\boldsymbol{J}_f$ reduces to the conduction current density $\boldsymbol{J}_c$. For an isotropic, linear and dispersive medium, the constitutive equations can be written using a Taylor series as:

$$\boldsymbol{D} = \varepsilon\boldsymbol{E} + \varepsilon_1\frac{\partial\boldsymbol{E}}{\partial t} + \varepsilon_2\frac{\partial^2\boldsymbol{E}}{\partial t^2} + \varepsilon_3\frac{\partial^3\boldsymbol{E}}{\partial t^3} + \cdots \tag{2}$$

$$\boldsymbol{B} = \mu\boldsymbol{H} + \mu_1\frac{\partial\boldsymbol{H}}{\partial t} + \mu_2\frac{\partial^2\boldsymbol{H}}{\partial t^2} + \mu_3\frac{\partial^3\boldsymbol{H}}{\partial t^3} + \cdots \tag{3}$$

$$\boldsymbol{J}_c = \sigma\boldsymbol{E} + \sigma_1\frac{\partial\mathbf{E}}{\partial \mathrm{t}} + \sigma_2\frac{\partial^2\mathbf{E}}{\partial t^2} + \sigma_3\frac{\partial^3\mathbf{E}}{\partial t^3} + \cdots \tag{4}$$

where $\varepsilon_q$, $\mu_q$ and $\sigma_q$ are weighting factors for the higher order terms. (1)-(4) can be expressed for the steady-state frequency domain (with $e^{+j\omega t}$ time harmonic dependence) as follows:

$$\nabla\times\boldsymbol{H} = \boldsymbol{J}_f + j\omega\boldsymbol{D} \tag{5}$$

$$\boldsymbol{D} = \varepsilon\boldsymbol{E} + j\omega\varepsilon_1\boldsymbol{E} - \omega^2\varepsilon_2\boldsymbol{E} - j\omega^3\varepsilon_3\boldsymbol{E} + \cdots \equiv \left(\underbrace{\varepsilon'(\omega) - j\varepsilon''(\omega)}_{\varepsilon(\omega)}\right) \tag{6}$$

$$\boldsymbol{B} = \mu\boldsymbol{H} + j\omega\mu_1\boldsymbol{H} - \omega^2\mu_2\boldsymbol{H} - j\omega^3\mu_3\boldsymbol{H} + \cdots \quad \equiv \left(\underbrace{\mu'(\omega) - j\mu''(\omega)}_{\mu(\omega)}\right)\boldsymbol{H} \tag{7}$$

$$\boldsymbol{J_c} = \sigma\boldsymbol{E} + j\omega\sigma_1\boldsymbol{E} - \omega^2\sigma_2\boldsymbol{E} - j\omega^3\sigma_3\boldsymbol{E} + \cdots \equiv \left(\underbrace{\sigma'(\omega) - j\sigma''(\omega)}_{\sigma(\omega)}\right)\boldsymbol{E} \tag{8}$$

where $\varepsilon(\omega)$ , $\mu(\omega)$ and $\sigma(\omega)$ describe the intrinsic bulk effects of polarization, magnetization and conductivity, in complex form, respectively. For standard metals at room temperature $\varepsilon(\omega) \cong \varepsilon_o$, the permittivity of free space; with non-magnetic materials $\mu(\omega) = \mu_o$, the permeability of free space; and with low frequency room temperature modelling of materials $\sigma(\omega) \cong \sigma_o$, intrinsic bulk conductivity at dc. In the more general case, (5)-(8) yield the following:

$$\nabla \times \boldsymbol{H} = \boldsymbol{J}_c + j\omega \boldsymbol{D} = \left( \underbrace{\sigma(\omega) + j\omega\varepsilon(\omega)}_{\sigma_{eff}(\omega)} \right) \boldsymbol{E} \; = j\omega \left( \underbrace{\varepsilon(\omega) - j\frac{\sigma(\omega)}{\omega}}_{\varepsilon_{eff}(\omega)} \right) \boldsymbol{E} \tag{9}$$

From (9), it is obvious that the effective parameters $\sigma_{eff}(\omega)$ and $\varepsilon_{eff}(\omega)$ can be used interchangeably; being related to each other by the textbook expression:

$$\sigma_{eff}(\omega) = j\omega\varepsilon_{eff}(\omega) \tag{10}$$

where the effective permittivity $\varepsilon_{eff}(\omega) = \varepsilon_o \varepsilon_{r,eff}(\omega)$ and $\varepsilon_{r,eff}(\omega)$ is the relative effective permittivity (this is commonly referred to as the dielectric function; although, this should not be confused with the dielectric constant, which represents only the real part of the relative effective permittivity).

Partitioning (9) into its real and imaginary parts, the following is obtained:

$$\begin{aligned} \nabla \times \boldsymbol{H} &= \left[ \left( \underbrace{\sigma'(\omega) + \omega\varepsilon''(\omega)}_{\sigma'_{eff}(\omega)} \right) - j \left( \underbrace{\sigma''(\omega) - \omega\varepsilon'(\omega)}_{\sigma''_{eff}(\omega)} \right) \right] \boldsymbol{E} \\ &= j\omega \left[ \left( \underbrace{\varepsilon'(\omega) - \frac{\sigma''(\omega)}{\omega}}_{\varepsilon'_{eff}(\omega)} \right) - j \left( \underbrace{\varepsilon'' + \frac{\sigma'}{\omega}}_{\varepsilon''_{eff}(\omega)} \right) \right] \boldsymbol{E} \end{aligned} \tag{11}$$

Then by rearranging (11) for $\varepsilon_{eff}(\omega)$ the effective dielectric loss tangent $tan\delta_e$ is defined (even for a metal [28]) as follows:

$$\begin{aligned} &\varepsilon_{eff}(\omega) = \varepsilon'_{eff}(\omega)(1 - jtan\delta_e) \\ &\text{where } tan\delta_e \equiv \frac{\varepsilon''_{eff}(\omega)}{\varepsilon'_{eff}(\omega)} = \frac{\varepsilon''_{r,eff}(\omega)}{\varepsilon'_{r,eff}(\omega)} = \frac{\sigma'_{eff}(\omega)}{\sigma''_{eff}(\omega)} \end{aligned} \tag{12}$$

As can be seen from (12), the dielectric loss tangent quantifies the losses for a non-magnetic material, but it does not distinguish the origin of different loss mechanisms. In other words, it does not give any information about the polarization or conductivity loss contributions separately. This means that when material parameters are being evaluated experimentally the effective parameters (including $tan\delta_e$) should be used. However, in the open literature, many authors loosely use the terminology "*complex permittivity*" or "*complex conductivity*" to describe the effective parameters, based on the fact that the effective parameters are complex numbers [44-48]. This can be confusing if not defined explicitly, since the intrinsic permittivity and conductivity themselves can be complex numbers. Thus, it may be ambiguous as to whether the authors are referring to the intrinsic parameters, $\varepsilon(\omega), \sigma(\omega)$, or to their associated effective parameters, $\varepsilon_{eff}(\omega)$ , $\sigma_{eff}(\omega)$; with the latter set always being complex numbers. When the former are represented by purely real quantities, as in the case where frequency dispersion of polarization can be neglected (e.g., metals having $\varepsilon'(\omega) \cong \varepsilon_o$ and $\varepsilon''(\omega) = 0$):

$$\varepsilon_{eff}(\omega) = \left(\varepsilon'(\omega) - \frac{\sigma''(\omega)}{\omega}\right) - j\left(\frac{\sigma'(\omega)}{\omega}\right) \qquad (13)$$

$$tan\delta_e = \frac{\sigma'(\omega)}{\omega\varepsilon'(\omega) - \sigma''(\omega)} \qquad (14)$$

To this end, (6)-(8) must always be compatible with the principle of conservation of energy, which in electromagnetic systems is expressed by Poynting's theorem. Also, the passivity of such materials implies that the power dissipated per cycle per unit volume must be non-negative. Thus,

$$\Re\left\{\frac{1}{2}\boldsymbol{E}\cdot\boldsymbol{J}_c^* + \frac{j\omega}{2}(\boldsymbol{B}\cdot\boldsymbol{H}^* - \boldsymbol{E}\cdot\boldsymbol{D}^*)\right\} \geq 0 \qquad (15)$$

with the equality only being valid for a lossless material. Substituting (6)-(8) into (15) and re-writing in quadratic form gives:

$$\Re\left\{[\boldsymbol{E}^* \quad \boldsymbol{H}^*]\begin{bmatrix}(\sigma'(\omega) + \omega\varepsilon''(\omega)) + j(\sigma''(\omega) - \omega\varepsilon'(\omega)) & 0 \\ 0 & j\omega(\mu'(\omega) - j\mu''(\omega))\end{bmatrix}\begin{bmatrix}\boldsymbol{E} \\ \boldsymbol{H}\end{bmatrix}\right\} \geq 0 \qquad (16)$$

Using the general relationship:

$$\Re\{\boldsymbol{A}^* \cdot \boldsymbol{M} \cdot \boldsymbol{A}\} = \boldsymbol{A}^* \cdot \mathbf{M}' \cdot \boldsymbol{A} \quad \text{where } \boldsymbol{M}' = \frac{\boldsymbol{M} + \boldsymbol{M}^\dagger}{2} \tag{17}$$

where † represents the conjugate transpose matrix and taking into account that (16) holds for arbitrary electric and magnetic fields, the matrix $\boldsymbol{M'}$ must be positive semi-definite. This is ensured by the following two conditions:

$$\sigma'_{eff}(\omega) = (\sigma'(\omega) + \omega\varepsilon''(\omega)) \geq 0 \tag{18}$$

$$\text{and } \mu''(\omega) \geq 0 \tag{19}$$

In order that (18) holds for arbitrary frequencies, the conditions where $\sigma'(\omega) \geq 0$ and $\varepsilon''(\omega) \geq 0$ have to be verified.

When the classical relaxation-effect model for normal metals at room temperature is used, the intrinsic bulk conductivity is given by the following expression [20, 28]:

$$\sigma(\omega) = \frac{\sigma_o}{1 + j\omega\tau} = \left(\underbrace{\frac{\sigma_o}{1 + \omega^2\tau^2}}_{\sigma'(\omega)}\right) - j\left(\underbrace{\frac{\sigma_o\omega\tau}{1 + \omega^2\tau^2}}_{\sigma''(\omega)}\right) \tag{20}$$

where $\tau$ is the phenomenological scattering relaxation time and both $\sigma'(\omega)$ and $\sigma''(\omega)$ are always positive numbers.

It is important to note that if a time dependence of the form $e^{-j\omega t}$ is used, the complex operator "$+j$" in all the previous equations must be replaced with "$-j$", resulting in material parameters being redefined by the forms $\varepsilon(\omega) = \varepsilon'(\omega) + j\varepsilon''(\omega)$, $\mu(\omega) = \mu'(\omega) + j\mu''(\omega)$, $\sigma(\omega) = \sigma'(\omega) + j\sigma''(\omega)$ and $\sigma_{eff}(\omega) = -j\omega\varepsilon_{eff}(\omega) = \sigma(\omega) - j\omega\varepsilon(\omega)$. While this point may seem obvious, errors will be introduced when parameters and equations that adopt different conventions (e.g. when originating from different sources) are inadvertently mixed during the modelling process. By default, the following standard commercial packages HFSS™ [51], CST MWS [52] and EMPro [53] adopt the $e^{+j\omega t}$ convention; while RSoft [54] adopts the $e^{-j\omega t}$ convention.

Furthermore, [49-50, 55] shows that from a comparison of metal cavities, metal-pipe rectangular waveguides and analytical models it is possible to understand what materials apply to which boundary conditions and the correct method of entering the data into the solver. Table I shows the correct practice as identified in [55].

TABLE I
Summary of different modelling strategies for metal structures using HFSS™ and CST MWS [55]

<table>
<tr><th colspan="2" rowspan="2"></th><th colspan="2">HFSS™</th><th colspan="2">CST MWS</th></tr>
<tr><th>Eigenmode Solver</th><th>Other solvers</th><th>Eigenmode Solver</th><th>Other solvers</th></tr>
<tr><td rowspan="4">Solid object definition</td><td>Input parameters</td><td colspan="2">$\sigma_o$ or data file of $\sigma'(f)$</td><td rowspan="4"></td><td>$\sigma_o$ or discrete points of $\sigma'(f)$ or $\omega_p$ and $\omega_\tau$</td></tr>
<tr><td>Error</td><td>significant</td><td>negligible</td><td>negligible/significant</td></tr>
<tr><td>Model</td><td colspan="2">(1) classical skin-effect<br>(2) simple relaxation-effect<br>(3) classical relaxation-effect*</td><td>(1) classical skin-effect<br>(2) simple relaxation-effect<br>(3) classical relaxation-effect</td></tr>
<tr><td>Comments</td><td colspan="2">without "solve inside" function enabled</td><td>For (1) and (2) the error is negligible, for (3) the error is significant</td></tr>
<tr><td rowspan="4">FCB<br>(HFSS™)<br><br>and<br><br>CWB<br>(CST MWS)</td><td>Input parameters</td><td>$\sigma_o$ or $\sigma'(f_I)$</td><td>$\sigma_o$ or data file of $\sigma'(f)$</td><td>$\sigma_o$</td><td>$\sigma_o$ or $\sigma'(f)$</td></tr>
<tr><td>Error</td><td>negligible /small</td><td>negligible</td><td>negligible</td><td>negligible</td></tr>
<tr><td>Model</td><td colspan="4">(1) classical skin-effect<br>(2) simple relaxation-effect</td></tr>
<tr><td>Comments</td><td>In general, $f_I$ is not known a priori so (2) is of limited use</td><td></td><td>Input parameters are ignored, lossy metals are considered as PEC and $\sigma$ is entered in the post-processing stage</td><td>Input parameters should be entered at each discrete frequency point</td></tr>
<tr><td rowspan="4">LIB<br>(HFSS™)</td><td>Input parameters</td><td>data file of $\varepsilon'_{r,eff}(f)$ and $\sigma'(f)$</td><td>data file of $\varepsilon'_{r,eff}(f)$ and $\sigma'(f)$</td><td rowspan="4"></td><td rowspan="4"></td></tr>
<tr><td>Error</td><td>may be significant</td><td>negligible</td></tr>
<tr><td>Model</td><td colspan="2">(1) classical skin-effect<br>(2) simple relaxation-effect<br>(3) classical relaxation-effect</td></tr>
<tr><td>Comments</td><td>In general, this is a two-run simulation</td><td></td></tr>
<tr><td rowspan="4">IB<br>(HFSS™)<br><br>and<br><br>SIM<br>(CST MWS)</td><td>Input parameters</td><td>$R_s(f_I), X_s(f_I)$</td><td>$R_s(f)$, $X_s(f)$</td><td colspan="2">Data file of $R_s(f), X_s(f)$</td></tr>
<tr><td>Error</td><td>negligible</td><td>negligible</td><td>negligible</td><td>significant</td></tr>
<tr><td>Model</td><td colspan="2">(1) classical skin-effect<br>(2) simple relaxation-effect<br>(3) classical relaxation-effect</td><td>(1) classical skin-effect<br>(2) simple relaxation-effect</td><td>(1) classical skin-effect<br>(2) simple relaxation-effect<br>(3) classical relaxation-effect</td></tr>
<tr><td>Comments</td><td>In general, $f_I$ is not known a priori so (2) is of limited use</td><td>Input parameters should be entered at each discrete frequency point</td><td>Input parameters are ignored, lossy metals are considered as PEC and $\sigma$ is entered in the post-processing stage</td><td></td></tr>
</table>

***** If the 'solve inside' function is disabled the results will not be correct. However, with the 'solve inside' enabled and with the input parameters shown later the results should be correct, although this approach is impractical as explained in the Discussion section.

The following chapter looks at the use of plasmonic devices for THz. Initially an overview of surface plasmon theory and follows with a study of correct electromagnetic modelling of a benchmark spoof plasmon structure from the literature. The chapter concludes by looking at the use of smooth silicon surfaces to create frequency tuneable sensors with highly confined fields for terahertz sensing.

Chapter 3 moves towards more conventional quasi-optical metal mesh filters for low cost manufacture as are created on electrically thick substrates rather than the high cost and fragile electrically thin substrates conventionally used. Two different filter structures are experimentally demonstrated that comprise a single ultra thin metallic layer on an electrically thick fused silica substrate. Both structures show excellent out of band rejection. The chapter concludes with a novel design and simulation of a THz stress sensor based on the metal mesh filter.

Chapter 4 looks into the use of photonic crystal technology. Several state-of-the-art devices are demonstrated: resonators, switches and attenuators. The resonators have been measured and demonstrated to have an unloaded Q-factor of ~9,000 that is limited by the dielectric substrate. The switches and attenuators work across the operating band of the W1 defect waveguide and show a maximum attenuation of 60 dB and up to 40 dB across the whole band. These devices along with waveguides and splitters provide the building blocks for a future monolithically integrated THz architecture with potential applications in liquid sensing, communications and imaging.

# 2 Surface Wave Filters

Surface waves have been of exploited for many applications over the years, for applications such as over-the-horizon-radar. However more recent use of surface waves is in the field of plasmonics [56]. In plasmonics, the surface wave is a highly confined surface wave, known as a surface plasmon. It has been proven at optical frequencies to have many sensing applications e.g. temperature [57], bio-sensing [58] and improving LED efficiency [59].

Within this chapter, the theory of surface plasmons and two possible methods for their realization at THz is presented. Firstly, a simulation study of 'spoof' surface plasmons, which shows that accurate modelling techniques are required to obtain the correct results and secondly surface plasmons on semiconductors.

## 2.1 Theory

Theory predicts a surface plasmon can exist at the interface between two materials with a change in sign of dielectric constant (real part of permittivity) at the interface as shown in Fig. 9.

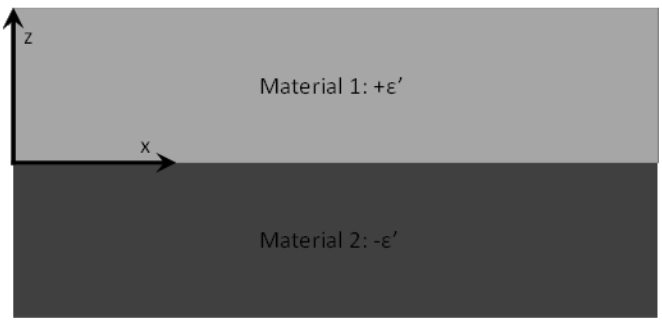


**Figure 9: Material Interface for Surface Plasmon**

Reference [60] gives an easy to follow derivation of this 2D problem, where the TM and TE modes are considered separately, to show the conditions required for a surface plasmon to exist. Presented here are the key parts of the TM mode derivation; other derivations can be found in [61].

Firstly, by solving the wave equation, the fields in the two medium are calculated (21)-(23) for the fields in material 1 and (24)-(26) for the fields within material 2 (with the material numbers defined in Fig. 9).

$$E_x(z) = jA_1 \frac{1}{\omega\varepsilon_0\varepsilon_1} k_1 e^{j\beta x} e^{-k_1 z} \tag{21}$$

$$E_z(z) = -A_1 \frac{\beta}{\omega\varepsilon_0\varepsilon_1} e^{j\beta x} e^{-k_1 z} \tag{22}$$

$$H_y(z) = A_1 e^{j\beta x} e^{-k_1 z} \tag{23}$$

$$E_x(z) = -jA_2 \frac{1}{\omega\varepsilon_0\varepsilon_2} k_2 e^{j\beta x} e^{k_2 z} \tag{24}$$

$$E_z(z) = -A_2 \frac{\beta}{\omega\varepsilon_0\varepsilon_2} e^{j\beta x} e^{k_2 z} \tag{25}$$

$$H_y(z) = A_2 e^{j\beta x} e^{k_2 z} \tag{26}$$

For a surface wave to exist, the fields must be continuous at the interface of materials 1 and 2. This condition is given in (27), by solving (21)-(26). Specifically, it shows that there must be a change in sign of dielectric constant across the interface, meaning that $\varepsilon_2' < 0$ when $\varepsilon_1' > 0$, and vice versa.

$$\frac{k_2}{k_1} = -\frac{\varepsilon_2}{\varepsilon_1} \tag{27}$$

As with all electromagnetic waves the fields must conform to the wave equation giving (28)-(29), which can then be combined to find the dispersion relation for surface plasmon mode (29).

$$k_1^2 = \beta^2 - k_0^2\varepsilon_1 \tag{28}$$

$$k_2^2 = \beta^2 - k_0^2\varepsilon_2 \tag{29}$$

$$\beta = k_0\sqrt{\frac{\varepsilon_1\varepsilon_2}{\varepsilon_1 + \varepsilon_2}} \tag{30}$$

A similar methodology can be presented for TE waves; however it will be found that surface plasmons cannot exist, as shown in [60-61].

A typical dispersion curve for an arbitrary conductor is near the light line at low frequency but diverges away from the light line as it asymptotically reaches the surface plasmon frequency, $\omega_{sp}$ (31), (with plasma frequency, $\omega_p$, of the material defined by (32)) where the wave becomes highly confined to the surface. Typical examples of these diagrams are seen in [60]-[61].

$$\omega_{sp} = \frac{\omega_p}{\sqrt{1 + \varepsilon_1}} \tag{31}$$

$$\omega_p = \sqrt{\frac{nq^2}{\varepsilon_0 m^*}} \tag{32}$$

It is known that metals have a dielectric function with $\varepsilon_r' < 0$ when the frequency of interest is lower than the plasma frequency. To accurately model the dielectric function of metals, the Drude Model (20) is used to calculate effective conductivity. This has been shown to be valid in [62] up to 100 THz depending on the metal. Above this frequency, the inter-band transitions effects become significant and further correction factors are required to describe this mathematically. Once the effective conductivity is found, the effective permittivity is calculated using (10). Initially gold is considered for the conducting medium (having the following room temperature parameters: $\sigma_o = 4.517{\cdot}10^7$ S/m, $\tau = 27.135$ fs [49]) and free-space is considered as the other medium.

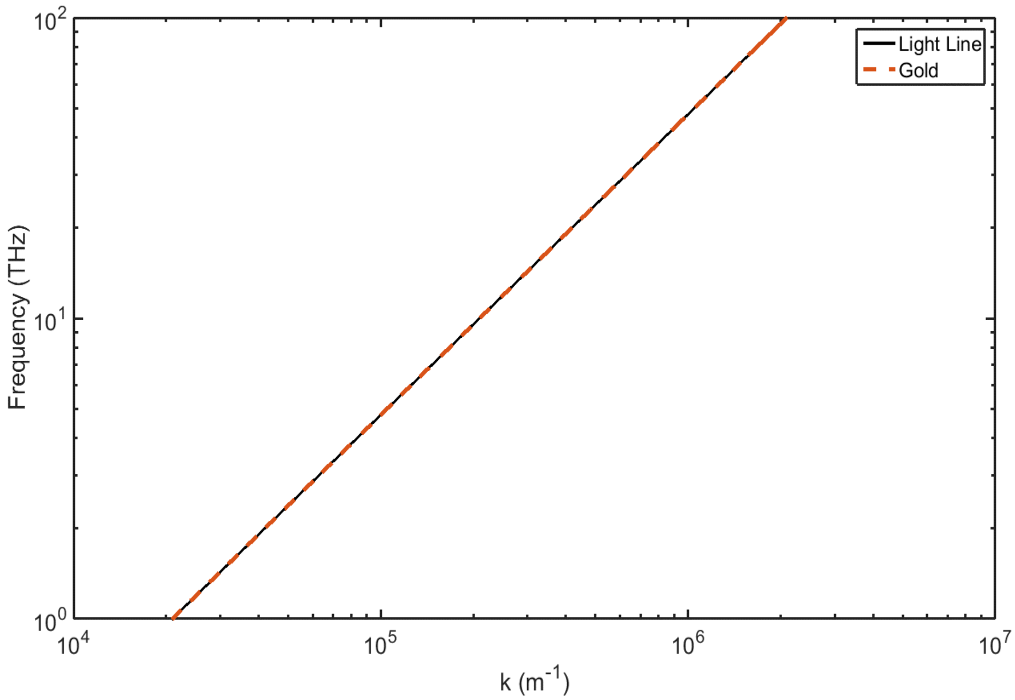


**Figure 10: Dispersion diagram for a gold/free space interface at THz**

Figure 10 shows the dispersion diagram for a gold/free space interface. It is clearly seen that the surface plasmon frequency ($\omega_{sp}$) is much greater than the 0.3-3THz band required, as there is little separation. This means that for a THz sensor, gold (or infact other smooth metal surface) is of no practical use as the fields are weakly confined to the surface, due to the k vector of the surface plasmon being so close to the light line.

There are several possible methods proposed to overcome this. The first is the use of spoof or designer surface plasmons. These create surface waves that are supported by a patterned metallic surface and have been widely modelled in various simulation domains

[63-65]. Within this section they are studied, to demonstrate how correct modelling practices must be used to generate the correct results using the various commercial frequency-domain software packages available. Time-domain codes are not considered, as they will introduce additional complications for causality, time gating and ringing (a good example of ringing is seen in Fig. 7 of [66]).

## 2.2 Qualitative simulation for Designer Surface Plasmons [*J. (2)*]

There are many results presented within the literature for designer surface plasmons at THz. Results presented in [65] show that it is possible for these ‘spoof’ surface plasmons to exist on a perfect electrical conductor boundary; meaning there is no field penetration into the conducting medium, whilst showing the same dispersion relation.

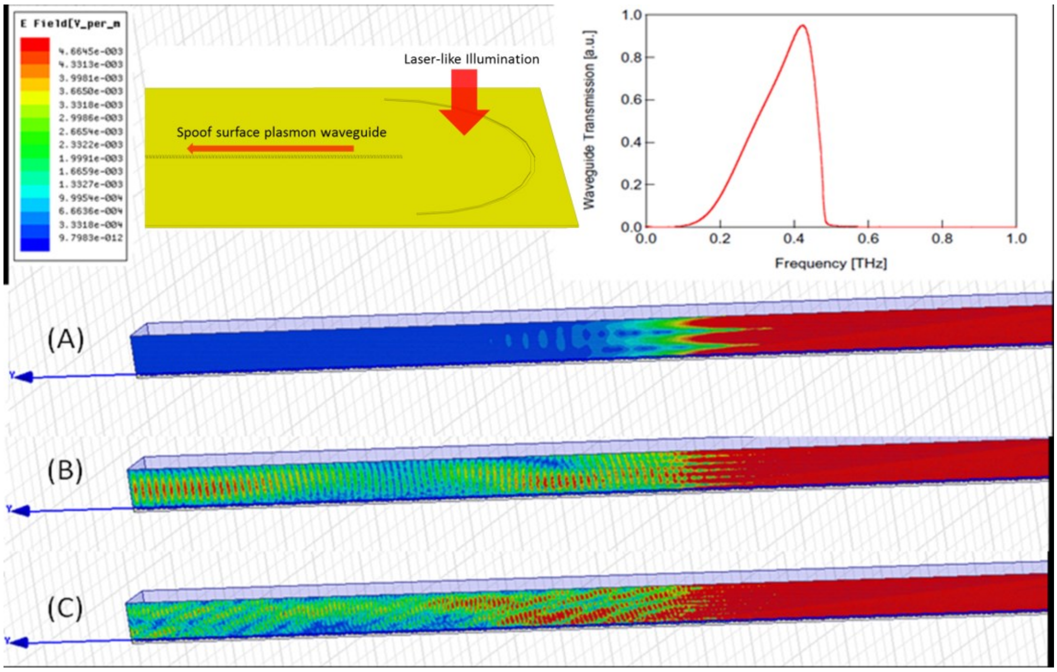


**Figure 11: Structure from [65] with 100 µm blind holes at: (a) 200 GHz; (b) 450GHz; and (c) 700 GHz, inserts show structure simulated in HFSS and the frequency response presented in [65]**

Figure 11 shows the results of simulations carried out to verify that a PEC surface with 100 µm deep blind holes, with a width and length of 500 µm and 150 µm, respectively, penetrating the metal surface so that it is able to support these ‘spoof’ surface plasmons at the THz band, as demonstrated in [65]. The surface wave was excited by a laser-like excitation, perpendicular to the direction that the surface wave travels.  It is shown that below the lower cut-off frequency there is very little transmission ,as shown by (a) at 200 GHz, however when the frequency is increased to 450 GHz (which is where peak transmission occurs) it is see that the waves couple to the surface (b) and finally when the frequency is above cut-off (c) the energy is re-radiated.

### *2.2.1 Benchmark Model Verification*

The simulation setup in Fig. 11 was useful for providing qualitative results to compare to [65]. However, due the large problem-space causing convergence issues within HFSS, the model is not completely accurate, due to mesh size limitations. To further study this structure and correct modelling procedures within the frequency domain solvers, a benchmark model was created. This is first compared to quantative results from [65].

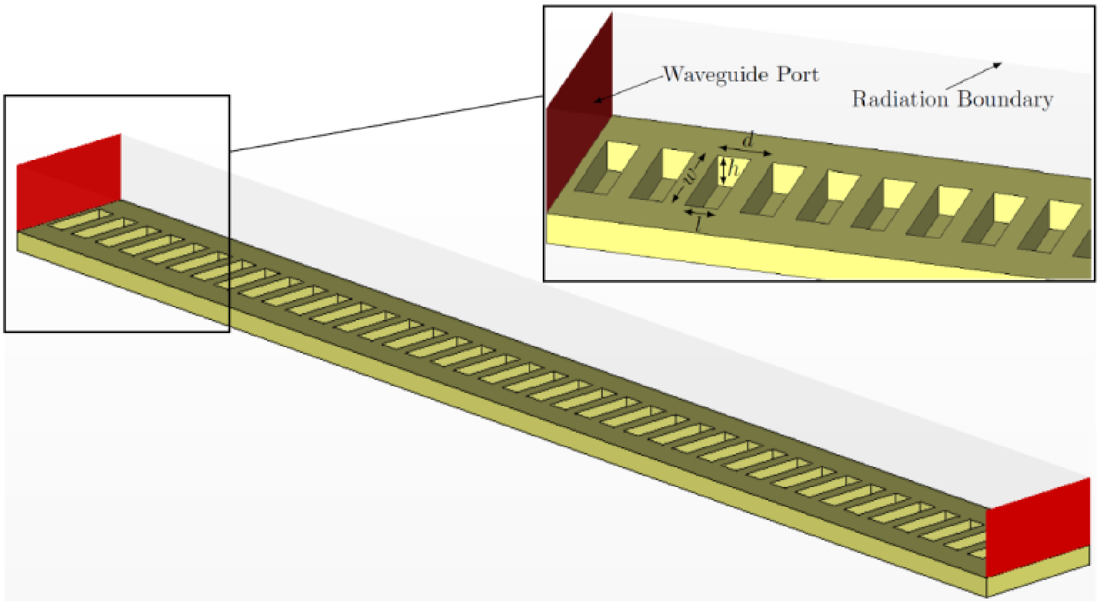


**Figure 12: Spoof plasmon benchmark structure**

The benchmark structure has periodically-spaced rectangular blind holes (i.e., open cavities) that do not completely perforate the metal film [65], as illustrated in Fig. 12. The width $w$ and length $l$ of the holes' aperture is 150 µm and 500 µm, respectively, with a periodicity $d$ of 250 µm and depth $h$ of either 100, 140 or 635 µm.

Figure 13 shows a comparison for PEC structures using the results from [65] and corresponding HFSS™ simulations using the benchmark model; while Fig. 14 shows a comparison of the experimental measured results from [65] and corresponding HFSS™ simulations using FCB (finite conductivity boundary) to model the fabricated aluminum structure. With $\sigma_0 = 3.767\text{x}10^7$ S/m and $\tau = 7.407$ fs [3.5], $\sigma'(f)$ was calculated for use with the simple relaxation-effect model [49] for the FCB.

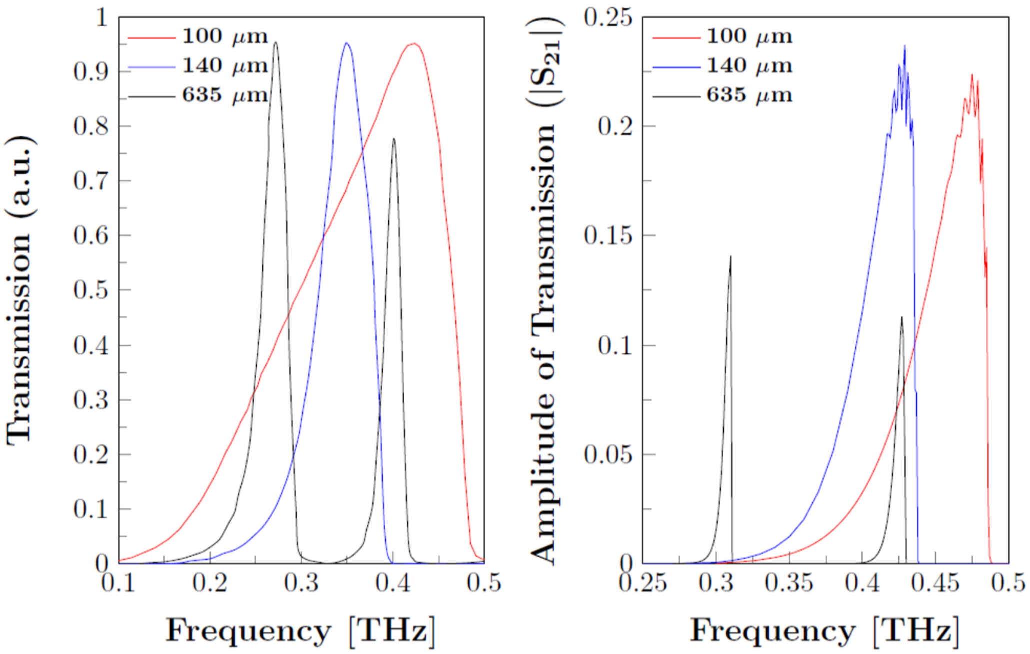


(a) (b)

**Figure 13: Simulated transmission results for PEC structure with different blind hole depths from: (a) results in [65]; and (b) HFSS™**

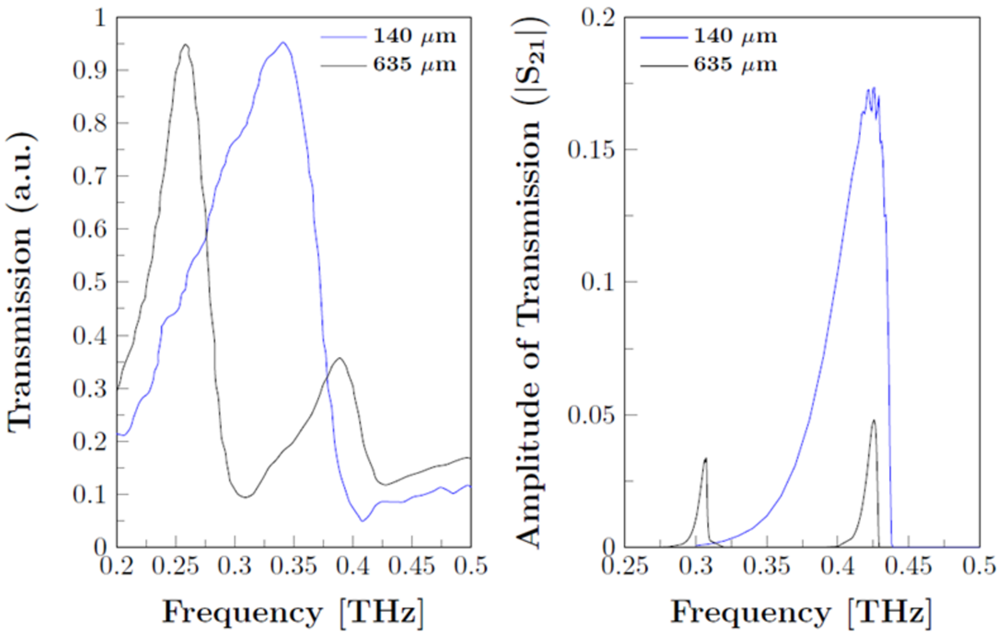


(a) (b)

**Figure 14: Transmission results for aluminium structure from: (a) experimental results in [65]; and (b) FCB simulation results using HFSS™.**

It is seen in Fig. 13 and Fig. 14 that HFSS™ predicts a much sharper upper cut-off frequency response than the corresponding results presented by [65], which in turn gives a slightly higher frequency for the peak in transmission. However, they do agree in that as depth increases the upper cut-off frequency of the dominant mode shifts down in frequency. The data presented also differs because transmission is calculated from the amplitude of the E-field component, along the propagation direction in [65], rather than by the $S_{21}$ in HFSS™. In addition, within the work from [65], the differences between their predicted and measured results shown in Fig. 13(a) and Fig. 14(a), respectively, is largely due to the introduction of the considerable ohmic losses (represented by the non-zero $R_s$) that degrades the slope of the cut-off frequencies and frequency detuning (represented by the non-zero $X_s$) that shifts the response down in frequency. In addition, there could be further detuning, attributed to poor fabrication tolerances from the non-micro fabrication nature of the manufacturing process. It should be noted that the data presented in [65] has been normalized with scaling factors that are not specified in their paper, so the HFSS™ results cannot be scaled accordingly to match those in [65].

### 2.2.2 Dominant Mode Variation

Since HFSS$^{TM}$ modelling has been shown to behave as expected, CST MWS and EMPro were also used to simulate the structure in Fig. 12, having blind holes in a gold substrate. The FCB boundary (or its equivalent) was used by all three software packages, as they were able to solve this problem in the frequency domain with waveguide excitations.

The results are given in Fig. 15. They show that initial simulations with just the single dominant mode $S_{21}$ provide widely varying predictions of performance from each software package. Further simulations were then performed with the lowest five modes excited at the ports, but with the results extracted for the dominated mode $S_{21}$, as shown in Fig. 15 It can be seen that the software packages agree when more modes are included.

The large discrepancies found with the frequency-domain solver in CST MWS have been attributed to the complicated broadband frequency response of the structure, and so the use of their transient solver was recommended [67].

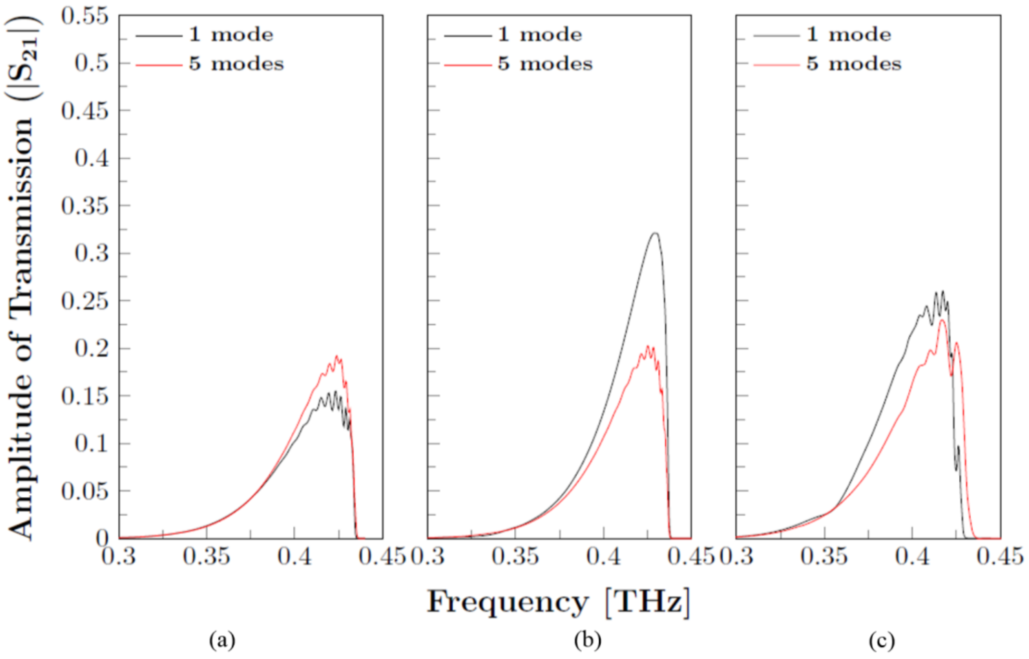


**Figure 15: Simulated transmission results for the spoof surface plasmon waveguide for the dominant mode using: (a) HFSS™; (b) CST MWS; and (c) EMPro.**

### *2.2.3 Boundary Condition Application*

Figure 16 shows that there is little difference between the various boundaries and frequency dispersion models employed when 5 modes are excited at the ports and then the total transmission is calculated by the linear summation of all the five $|S_{21}|$ values for the dominant port mode. Since the maximum simulation frequency is only 0.45 THz, the results obtained with FCB (using the classical skin-effect model) are almost identical to those obtained with the LIB (using the classical relaxation-effect model). However, with EMPro, there is a notable difference in the predicted transmission heights and levels of detuning.

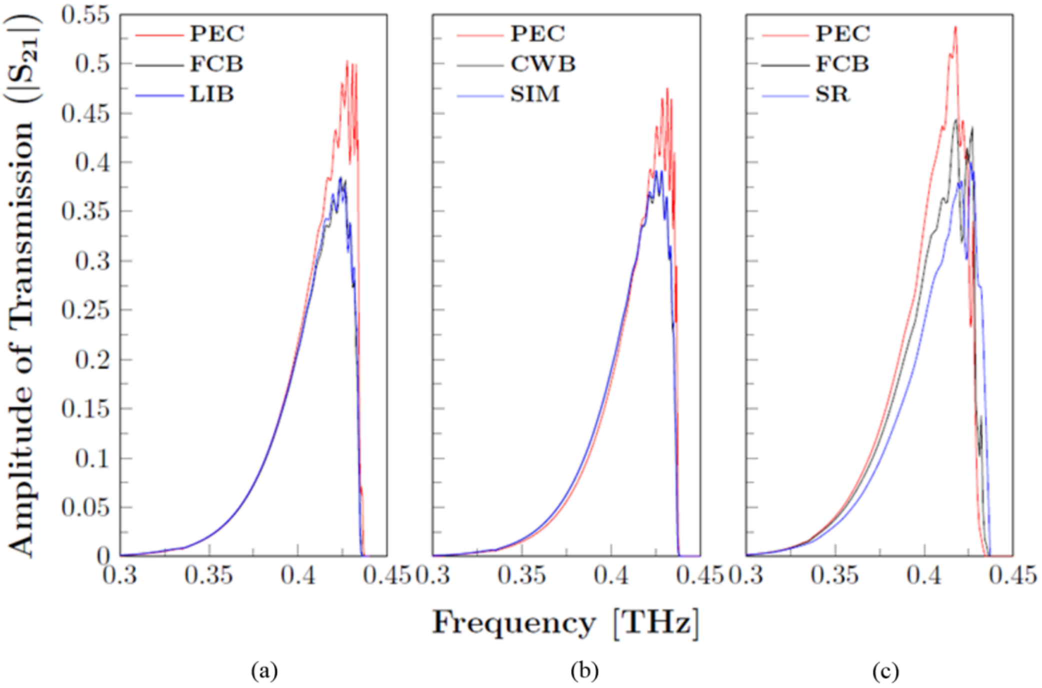


**Figure 16: Simulated transmission results for the spoof surface plasmon waveguide with 5 modes excited at the ports using: (a) HFSS™; (b) CST MWS; and (c) EMPro.**

This research has highlighted the need for multiple-mode excitation, even if only the results for the dominant mode are needed. If the computational burden is not significantly increased, more modes should be calculate at the output for each excited mode to achieve more accurate results. More conclusions have been found with regard to modeling of THz metals structures, such as waveguides and cavities,  are presented in full in [55, 68]. Since this study designer plasmon structures, have been demonstrated as a THz sensor discriminating between various liquids [69]. It should be noted that an alternative approach to describe spoof/designer surface plasmons is to describe them as coupled open cavities.

## 2.3 Surface Plasmons

As was previously shown in Fig. 7, metals cannot strongly confine a surface wave, due to their dispersion relation being close to the light line. As one moves nearer to the surface plasmon frequency, the confinement of the wave to the surface becomes much greater, which is ideal for a sensor. Equations (31)-(32) show that to lower the surface plasmon frequency one needs to reduce the plasma frequency. To do this, the material chosen must either have a reduction in the density of charge carriers ($n$) or an increase in the effect mass of the charge carriers ( $m*$ ) compared to metal. It should be noted that the sign of the charge on the carrier will not affect the plasma frequency. Within a semiconductor the amount of charge carriers can be controlled through dopants and the resulting region has a lower density of charge carriers compared to metals.

Silicon is a common example of a semiconductor. It has fewer free charge carriers than metals and the local density of the free carriers can be controlled through doping, photoconductivity and through a biasing structure. Silicon is also widely used in the electronics industry, which opens up the possibility that if THz plasmonic devices can be created, they could be monolithically integrated with current technology. Previous results of THz plasmonics [70]-[74] look at the patterning of the surface, in the same way as coupling spoof plasmons. However, as the following will show this adds unnecessary extra processing steps to create the blind holes, when it is possible to couple THz waves to a smooth silicon surface with careful selection of the silicon properties.

To show the potential of silicon to create terahertz devices, dispersion plots for the surface interface with free space with various doping levels are calculated and plotted. To do this, the plasma frequency must be calculated using (32), using the data shown in Table 1 [75] and the effective mass of the hole (weighted mean of heavy and light holes) and electron which are 0.36 and 0.26, respectively [76]. Equation (33) [60] can then be used to find the silicon's permittivity; dispersion curves for the surface plasmon modes are then calculated using (30).

$$\varepsilon(\omega) = \varepsilon_\infty - \frac{\omega_p^2}{\omega^2 - j\gamma\omega} \tag{33}$$

**Table 1: Carrier Concentration vs. Doped Silicon Resistivity**

| Resistivity (Ω·cm) | P-Type Majority Carrier Concentration ($cm^{-3}$) | N-Type Majority Carrier Concentration (cm-3) |
|---|---|---|
| 0.0001 | 1.20E+21 | 1.60E+21 |
| 0.001 | 1.70E+20 | 7.38E+19 |
| 0.01 | 8.94E+18 | 4.53E+18 |
| 0.1 | 2.77E+17 | 7.84E+16 |
| 1 | 1.46E+16 | 4.86E+15 |
| 10 | 1.34E+15 | 4.45E+14 |
| 100 | 1.33E+13 | 4.27E+13 |
| 1000 | 1.30E+13 | 4.20E+12 |
| 10000 | 1.30E+12 | 4.00E+11 |

The predicted dispersion curves having a surface plasmon frequencies that lie within the THz band are shown in Fig. 17. The surface plasmon frequency is lower in n-Type silicon for the same resistivity as p-Type silicon; this is due to the lower effective mass of the electrons in n-Type. These show the potential to make a THz sensor with a highly confined field as the surface plasmon frequency is in the THz region.

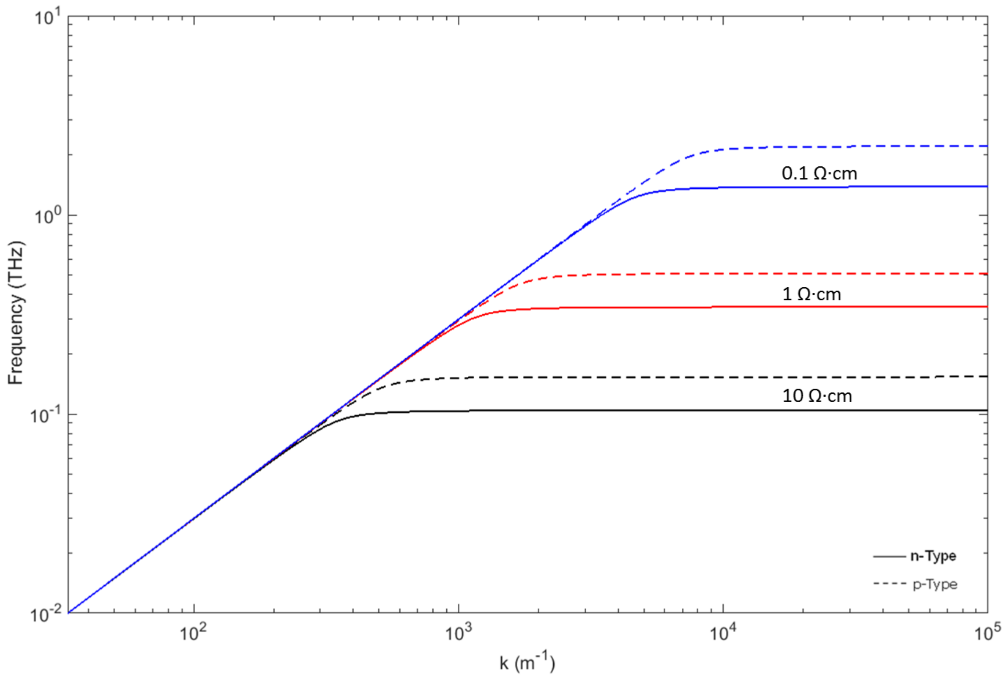


**Figure 17: Dispersion diagram for various silicon wafers**

To go on to experimentally verify these plots, a method to couple to the surface plasmon mode is required, as it lies away from the light line. There are three main methods to couple to the surface wave by matching k-vectors; (a) coupling gratings; (b) Otto method [77]; and (c) Kretschmann method [78], these are all shown in fig 18. Coupling grating [79] uses a periodic pattern etched into the surface and matches the incoming wave vector to the surface mode.

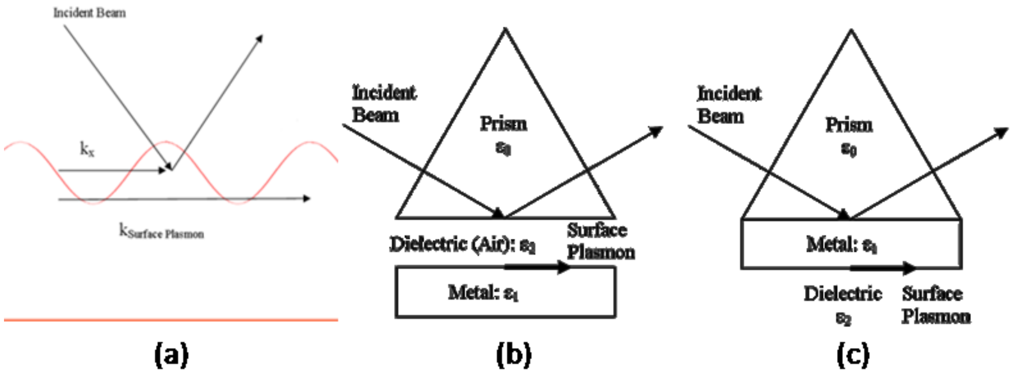


**Figure 18: Coupling mechanisms [80] (at optical frequencies hence metal) (a) grating coupler, (b) Otto Configuration, (c) Kretschmann Configuration.**

The Otto and Kretschmann methods are similar in the sense that they both use the frustrated total internal reflection of a prism' for coupling. Kretschmann coupling is the preferred method used at optical frequencies, as it requires a thin deposition of metal (through evaporation or sputtering) onto a prism. If this method was to be adopted for THz devices, it would require a much larger deposition of semiconductor on a prism made of materials like paraffin wax. This prism would be distorted through the temperatures involved with deposition of the semiconductor, making the Kretschmann method unfeasible for a THz device.

The Otto coupling method is impractical for ubiquitous optical devices, due to the alignment precision required between the prism and the substrate. However, it is practical for THz devices as the tolerances scale up in size. This is preferential to coupling gratings as extra fabrications steps are require for the latter, thereby becoming higher cost.

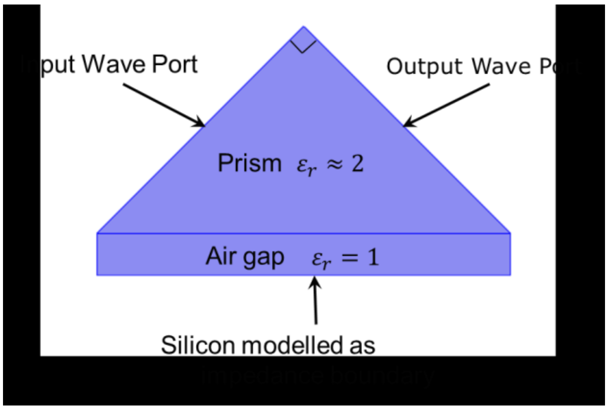


**Figure 19: Comsol 2-D simulation setup for Otto coupling to silicon**

Figure 19 shows the simulation setup used within Comsol for proof of concept. The prism is modelled as paraffin wax, with $\varepsilon_r' = 2$ [81], and the silicon is modelled as an impedance boundary condition. The excitation is provided by wave ports on either face of the prism. Figure 20 shows the results of the simulation, where the solid line shows the results with no silicon present, so the impedance boundary in Fig. 19 is set to a radiation boundary (as a reference). The dashed line shows the simulation when a $1\ \Omega \cdot cm$ n-Type silicon wafer is modelled as the impedance boundary condition. Both curves show a resonance superimposed on the transmission. This is caused by the Fabry-Perot resonance within the prism. At approximately 350 GHz, a sharp drop of 9 dB in transmission is seen. This is exactly as predicted by the numerical simulations in Fig. 21, where the dispersion line of the prism crosses the silicon surface plasmon mode dispersion curve. This means that energy is coupled into the surface plasmon mode on the silicon free space interface rather than being reflected off the prisms base.

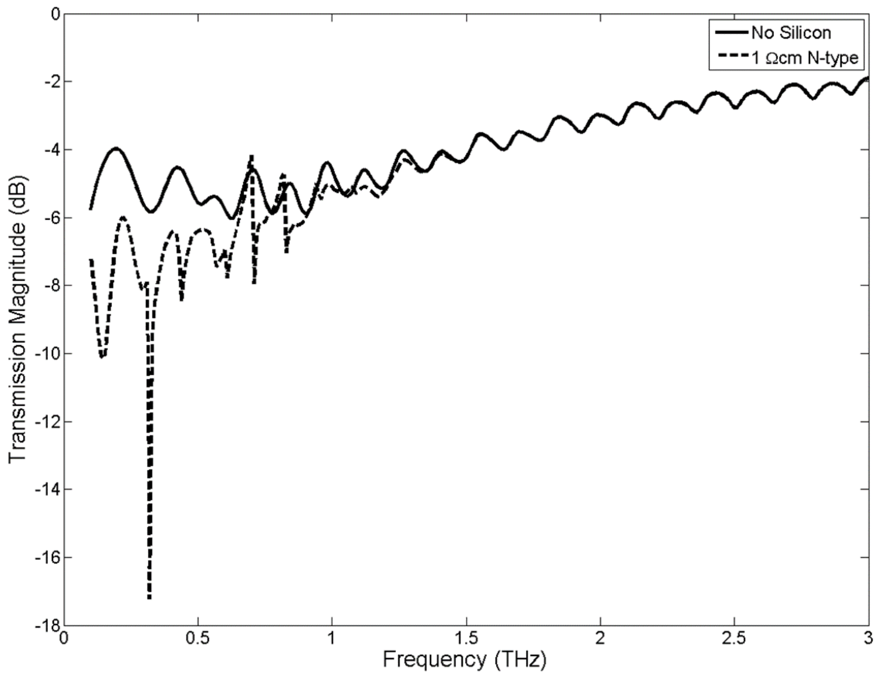


**Figure 20: Comsol simulation showing the predicted dropout at ~350 GHz when silicon is present**

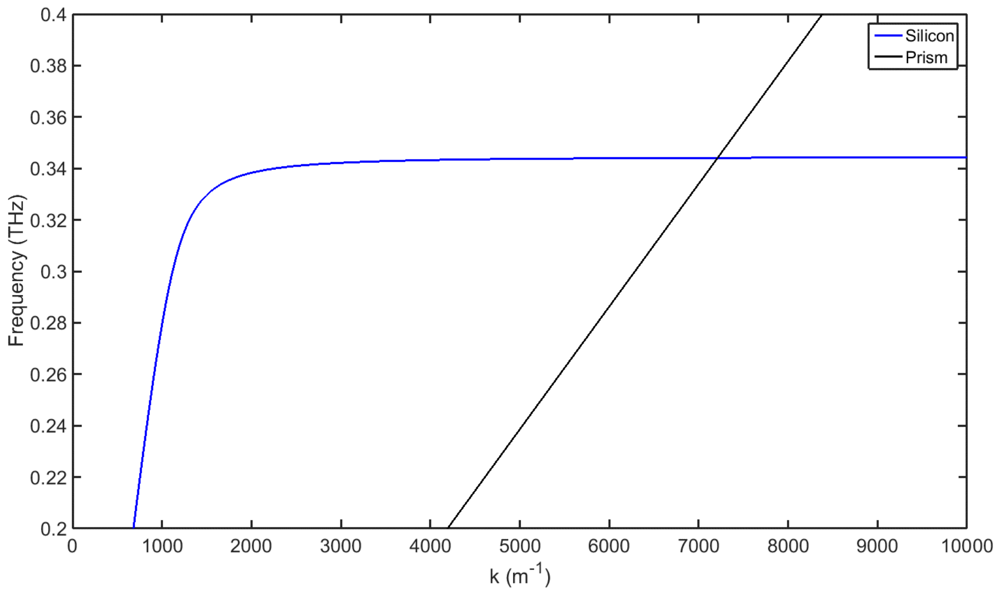


**Figure 21: Theoretical dispersion diagram of paraffin 1 Ω·cm -type silicon**

To demonstrate the possibility of using silicon as a sensor the 1 1 Ω·cm n-type silicon is used as a conductive medium and then the dielectric medium is swept from free-space $\varepsilon_r' = 1$ to $\varepsilon_r' = 10$ in integer steps. Figure 22 shows the predicted downwards frequency shift of the drop-out frequency, as $\varepsilon_r'$ of the dielectric medium increases. This demonstrates the possibility of using a planar silicon substrate as a THz sensor.

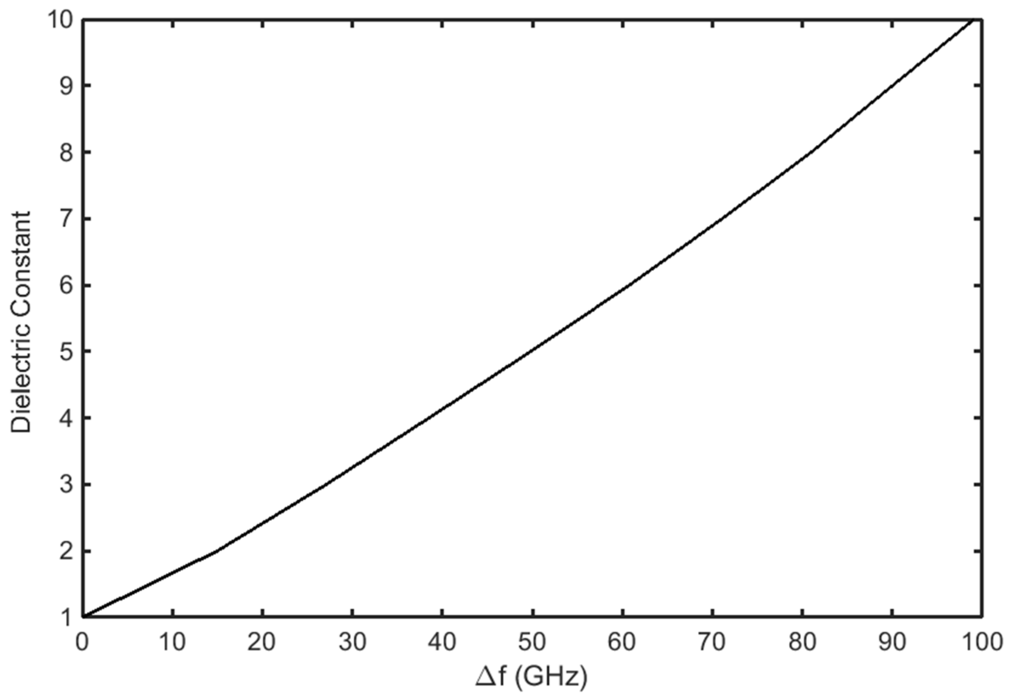


**Figure 22: Predicted frequency downshift for change in dielectric constant of medium 1**

## 2.4 Further Work

Within Section 2.3, theoretical work and simulations demonstrate coupling of a surface plasmon mode on a silicon dielectric interface at THz frequencies. The logical progression of this work is experimental verification of these results, where n-Type and p-Type silicon wafers of the same resistivity have different dispersion curves verify Fig. 17. This would be done through a similar setup employed with Comsol simulations

Beyond this, there are a wide variety of sensors already available using surface plasmon modes in the optical range. These sensor are all constrained by the conductivity of the metal, which is not easy to modify. Therefore, to interrogate a different frequency, the angle of the light incident on the base of the prism has to change, to get a different k-vector. However, at THz the conductive substrate is a semiconductor. It is well understood that the local conductivity of a semiconductor can be modified by biasing or illumination. By undertaking such a process, it will be possible to sweep the frequency as the change in conductivity causes a shift in the dispersion diagram; changing the frequency that is coupled to the surface plasmon mode. This was seen by looking at different wafers.

### 2.4.1 Electrostatic Sensor

The first method of locally modifying the conductivity of the silicon is to electrically bias the silicon. This has already been shown in many electronic devices and the simplest structure is the MOS capacitor. Figure 23 shows a concept device that has two top contacts and a bottom contact. By biasing the contacts, an electrostatic field will be generated. This will cause a movement of the free charges within the silicon which will oppose the field created. Using [82] to calculate the depth need to completely screen the field versus the silicon wafer resistivity, as shown in Fig. 24, it shows that this is a possible method to shift the frequency. For this sensor, a coupling grating would be integrated to couple to the surface plasmon mode, as seen in Fig. 18.

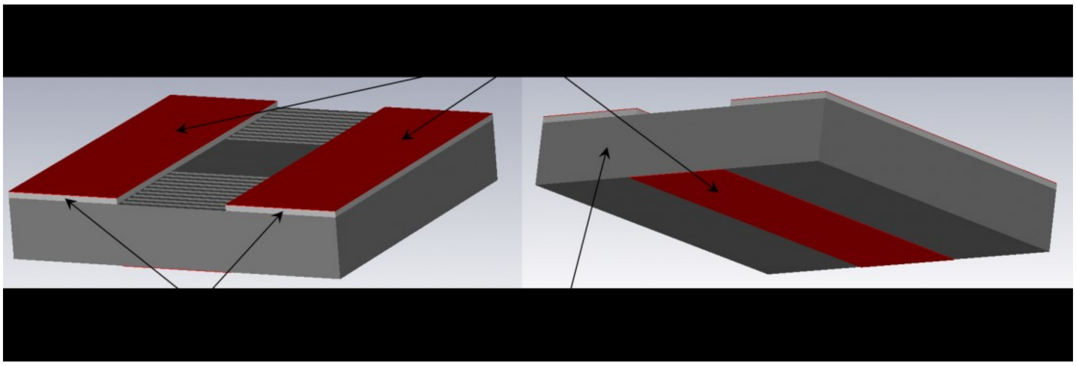

**Figure 23: Proposed electrostatic THz SPP sensor**

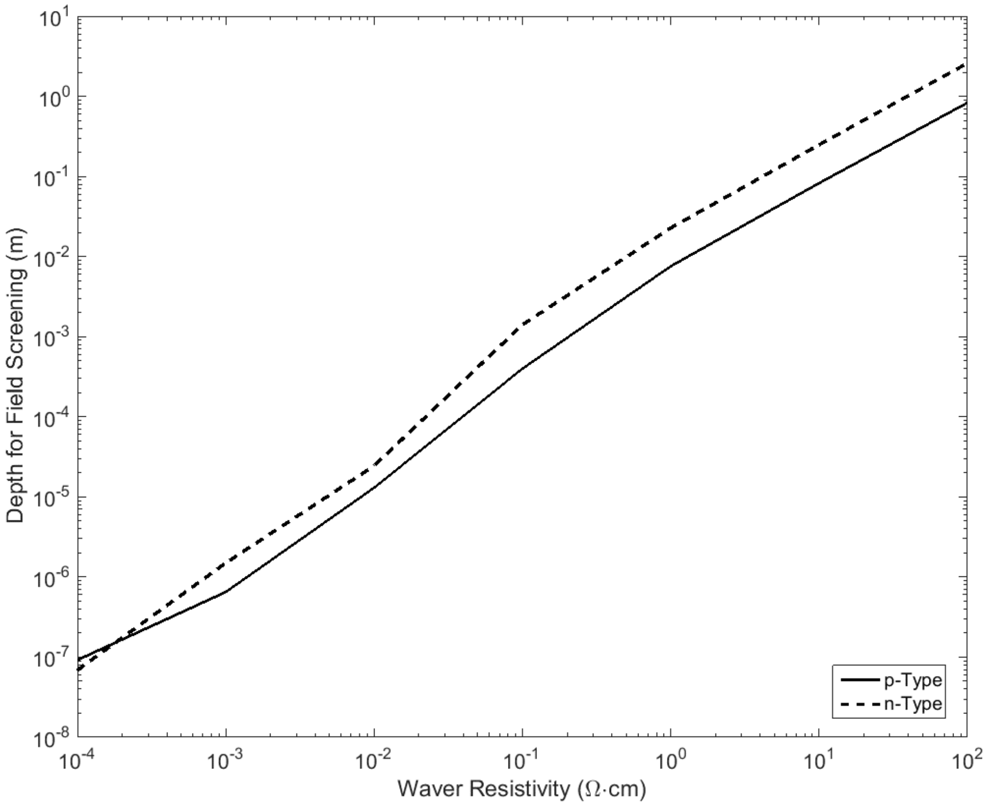


**Figure 24: Shielding depth for EM field in different resistivity wafers**

### *2.4.2 Photoconductive Sensor*

The second method to locally modify the conductivity of the silicon is to illuminate it with an electromagnetic wave, as silicon is a photoconductive material. This means that illuminating an area of silicon with an electromagnetic wave that has an energy greater than the silicon's bandgap energy will generate electron-hole pairs in the silicon, which will locally increase the conductivity. A conceptual diagram of such a sensor is shown in Fig. 25. A prism is used to couple to the surface plasmon mode, using the Otto coupling method. A laser beam incident from the side illuminates a spot under the prism, where the surface plasmon mode will couple. This sensor has the potential to become a ubiquitous THz sensor, in applications such as bio-sensing where disposable sensors are needed to avoid cross contamination; one only has to replace the silicon substrate, as everything else is isolated from the sample.

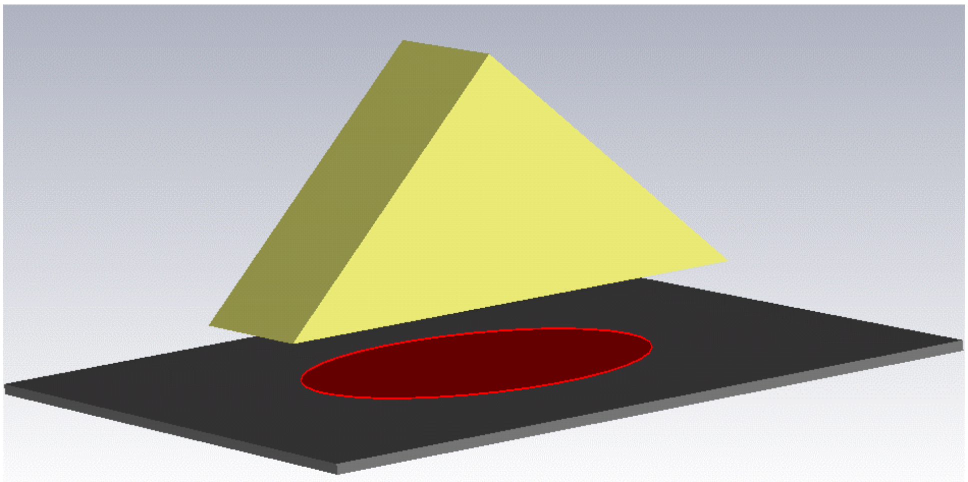

**Figure 25: Concept diagram of Otto coupled surface plasmon with laser spot modulating the silicon conductivity**

# 3 Metal Mesh Filters

Filters for sensing based on surface plasmons (discussed in the last chapter) are complex, as they require an accurate coupling method to excite the surface. A standard quasi-optical filter is a frequency selective surface, and so require no special coupling methods. The metal mesh filter, created through periodically patterning a metal film, is used in applications such as astronomy [83], sensors and imaging [84]. Their design varies from a single layer of metal [85] to stacks of metal and dielectric spacing layers [86]. By employing various different patterns in the metal, it is possible to produce all forms of filters [86]; band-pass, band-reject, low-pass and high-pass.

For THz there are several metal mesh filters commercially available, from 0.1 to 30 THz. Manufacturers typically do not show the out of band performance of the filters. For applications where good out-of-band rejection is vital, such as broadband spectroscopy. this performance information is critical to a systems engineer. Typical performance of QMC [87] and Lakeshore filters [88] are shown in Fig. 26 and Fig. 27, respectively. The filters from these two companies are regarded as state of the art, however they are expensiv;, often bespoke and made through a multilayer stack up process.

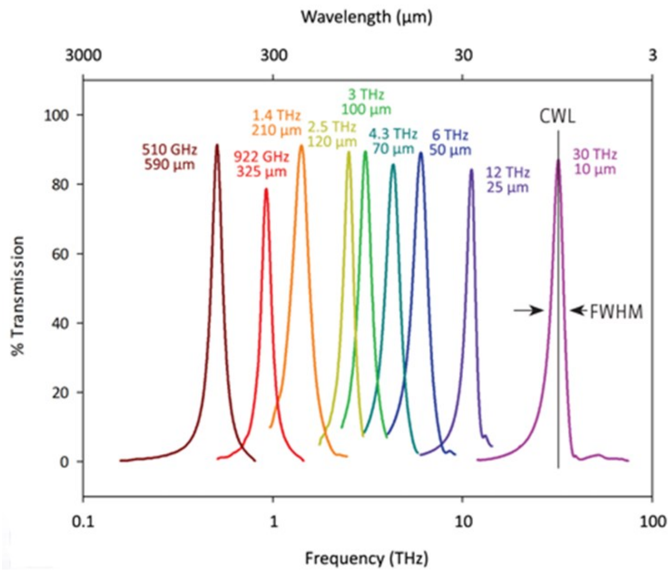


**Figure 26: Lakeshore state-of-the-art THz metal mesh filters [88]**

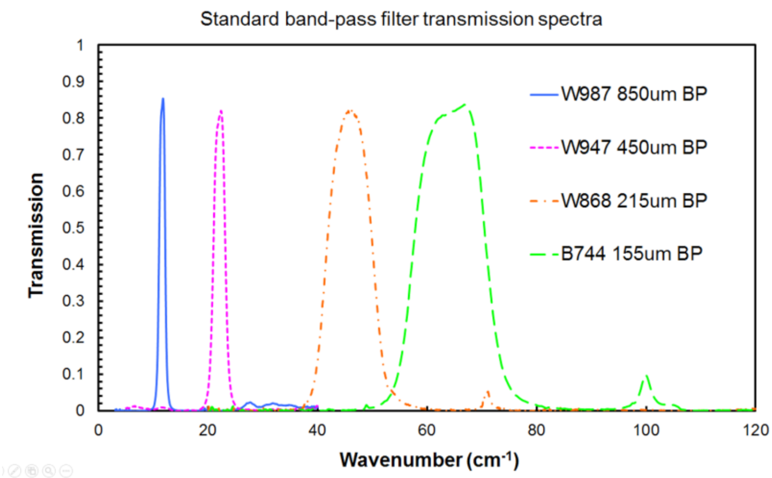


**Figure 27: QMC State-of-the-art THz metal mesh filters [87]**

These thin metallic films have been demonstrated on electrically thin substrates or encased within polymer layers to reduce the waveguide effect [89]. However, thin substrates are fragile and expensive and encasing the film within a polymer increases the cost due to the extra fabrication steps. The common alternative is to use self-supporting film designs, as demonstrated in lower frequencies [90]. However, at higher frequencies, for the filters to support themselves the metal becomes electrically thick. Therefore, unwanted waveguide modes can be excited within the structure [91].

This chapter demonstrates experimentally that, with careful design, standard 100 mm diameter and 525 µm thick wafers, which can be electrically thick, can be used for low cost, high performance and frequency-scalable ultra-thin metal mesh filters.

## 3.1 Design [*Int. Conf. (3)*]

The bandpass filter structure designed is based on a cross-shape cut out of the metal layer as illustrated in Fig. 28. Initial simulations were run for a freestanding ultra-thin metal layer. This is a well known and understood structure [92]; the effects of each parameter on the design was confirmed by parameter sweeps. Figure 28 gives an illustration of the metal mesh filter with the design parameters: lattice constant (*G*), length of the cross (*L*), width of the cross (*K*) and metal thickness (*h*). It is found that to tune the filter response these parameters have the following affects; increasing the lattice constant will decrease the bandwidth, increasing the length of the crosses will decrease the resonance frequency and increasing the width of the crosses will decrease the resonance frequency and decrease the bandwidth. Finally, the thickness of the metal was kept thin, to avoid unwanted waveguide modes within the crosses.

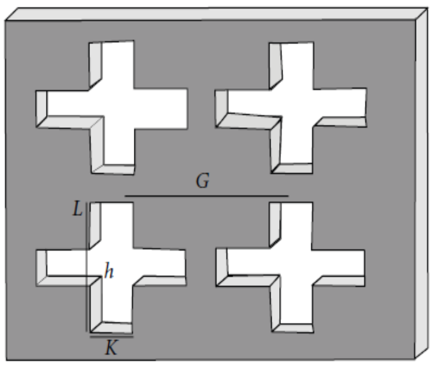


**Figure 28: [92] Cross shaped filter design parameters lattice constant (*G*), length of the cross (*L*), width of the cross (*K*) and metal thickness (*h*).**

The choice of substrate for the filters was limited by the following criteria: compatiblity with thin-film metallic processing (e.g. metal etchants, photolithography and sputter coating or evaporation), thick enough so as not to be too fragile during processing, rigid, and relatively low cost.

From these criteria, three substrate choices were identified: quartz or fused silica, sapphire and high resistivity silicon. All three are good THz materials, having relatively high transmittance. The dielectric constant for sapphire and high resistivity silicon are >11, whereas for fused silica the dielectric constant is 3.76. If a high permittivity substrate is chosen, a Fabry-Perot etalon will be created, as an electrically thick substrate is used. This will reducing out of band rejection and causing interfere with the mesh filter response. For this reason fused silica was chosen.

Figure 29 shows the stack up of the filter, as it would be used with the wave travelling from left to right, with $n_1$ being free space, $n_2$ the substrate and the filter is the thin metal mesh structure. When the substrate is added to the filter it detunes the filter from its free space response, due to dielectric loading. It is has been shown that $\lambda_R \rightarrow \lambda_{Rfree}\sqrt{0.5 \times (n_1^2 + n_2^2)}$, where $\lambda_R$ is the filter's resonant wavelength and $\lambda_{Rfree}$ is the filter's centre wavelength in free-space. This means that as a substrate is introduced where $n_2 > 1$ the filter is detuned to a longer wavelength as $n_2$ increases.


**Figure 29: Material Stack for filter**

Table 2 shows the optimised filters parameters to achieve resonances at 0.1 THz intervals over a 0.1 – 0.5 THz frequency band.  Simulations show that these produce the expected filter responses, as seen in Fig. 30. However, the out-of-band rejection for a simple cross shape filter is poor.

**Table 2: Conventional Metal Mesh filter optimal parameters**

| $f_R$ (THz) | G (µm) | K (µm) | L (µm) |
|---|---|---|---|
| **0.1** | 1150 | 100 | 975 |
| **0.2** | 680 | 50 | 423 |
| **0.3** | 440 | 30 | 293 |
| **0.4** | 360 | 20 | 210 |
| **0.5** | 290 | 15 | 160 |

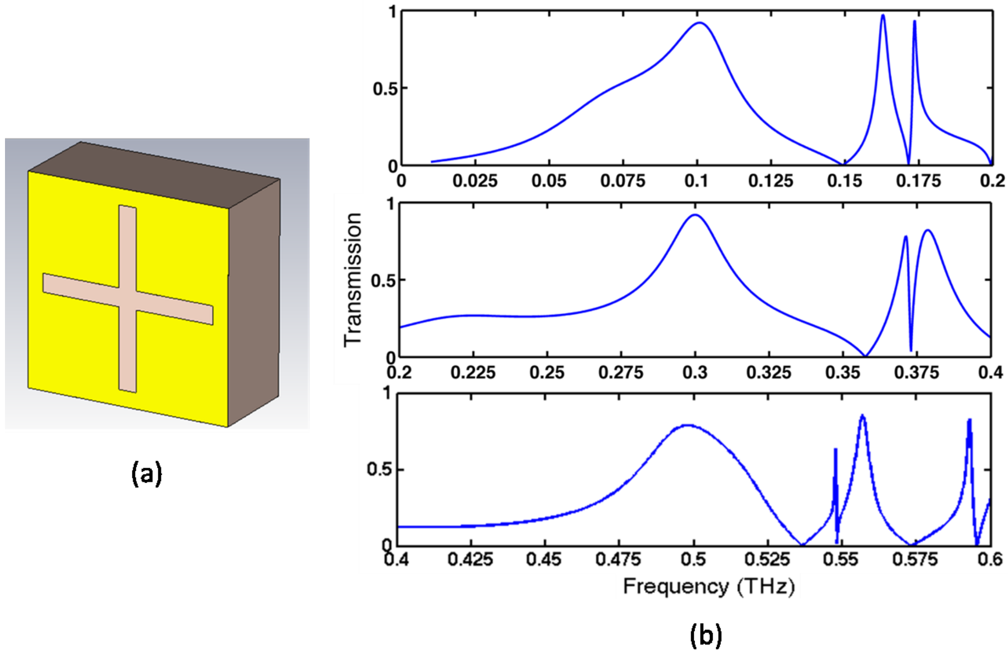


**Figure 30: Simulated unit cell (a); and (b) results of 0.1, 0.3 and 0.5 THz filters**

A method of improving the out-of-band rejection is to add an inner cross, causing a trapped mode excitation [93]. The inner cross has the opposite surface current to the outer structure, as shown in Fig. 31, causing this trapped mode. Table 3 shows optimised parameters for two designs at 0.1 and 0.3 THz. The designs were limited to 0.3 THz, as the planned manufacture method was to use an acetate mask, which limited the minimum feature size to 10 µm. The simulated performance is given in Fig. 32 and compared with the corresponding simulation of cross filters shown in Fig. 30. It can be seen that there is a greatly improved out of band performance.

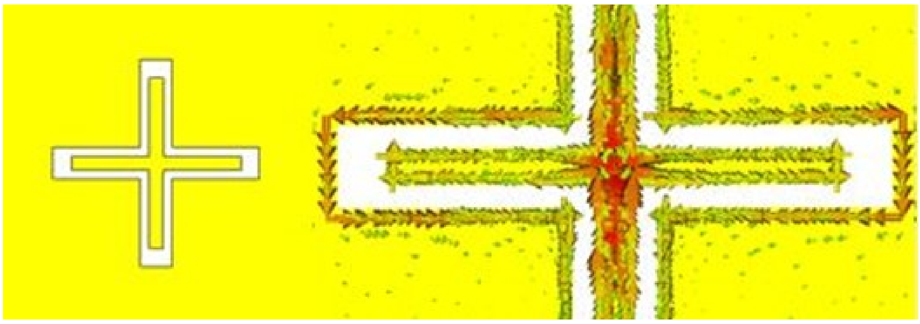

**Figure 31: (left) Trapped-mode filter shape and (right) current distribution in the metal.**

**Table 3: Trapped mode filter optimal parameters**

| $f_R$ (THz) | G (μm) | K (μm) | K2 (μm) | L (μm) | L2 (μm) |
|---|---|---|---|---|---|
| **0.1** | 978 | 92 | 51 | 744 | 540 |
| **0.3** | 365 | 36 | 16 | 234 | 193 |

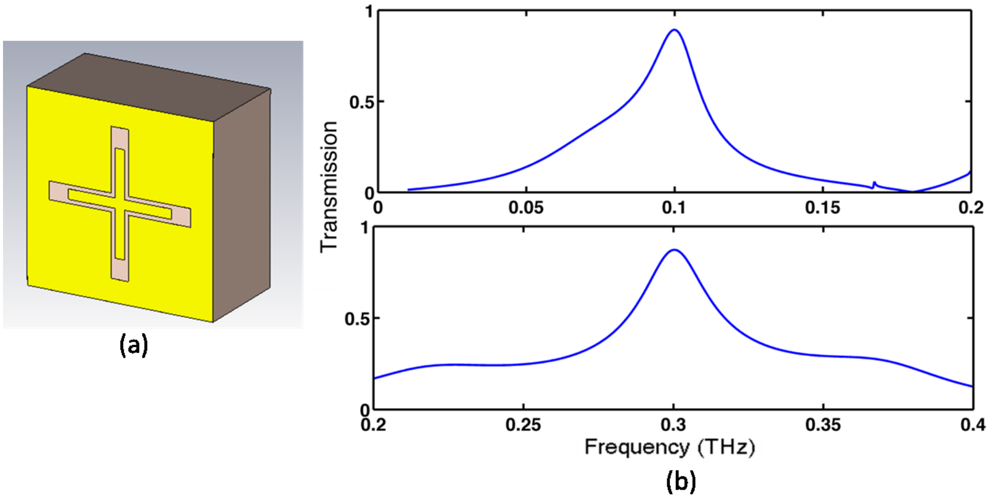


**Figure 32 Simulated unit cell (left) and results of 0.1, 0.3 and 0.3 THz trapped mode filters (right)**

## 3.2 Fabrication Method [*Int. Conf. (3)*]

Figure 33 shows the fabrication method for the filters. Firstly, a fused silica substrate is cleaned and then sputter coated with 35 μm of chrome. This layer acts as an adhesion promoting seed layer for the 150 μm gold layer, which is also sputtered coated. Without the seed layer the gold is likely to peel away from the substrate. Sputtering was chosen as it allows accurate control over the layer thickness, repeatability and smooth surface, when compared to using evaporation deposition. To pattern the metal layers, a 1 μm thickness S1813 photoresist is then spun on the wafer, soft baked and then exposed and developed using standard photolithographic techniques. With this photoresist mask properly developed, the two metal layers are selectively etched separately, using gold and chrome wet etchants, respectively. The filters were then initially inspected under a standard optical microscope, to confirm that the metal layers were etched. Figure 34 shows the final filter

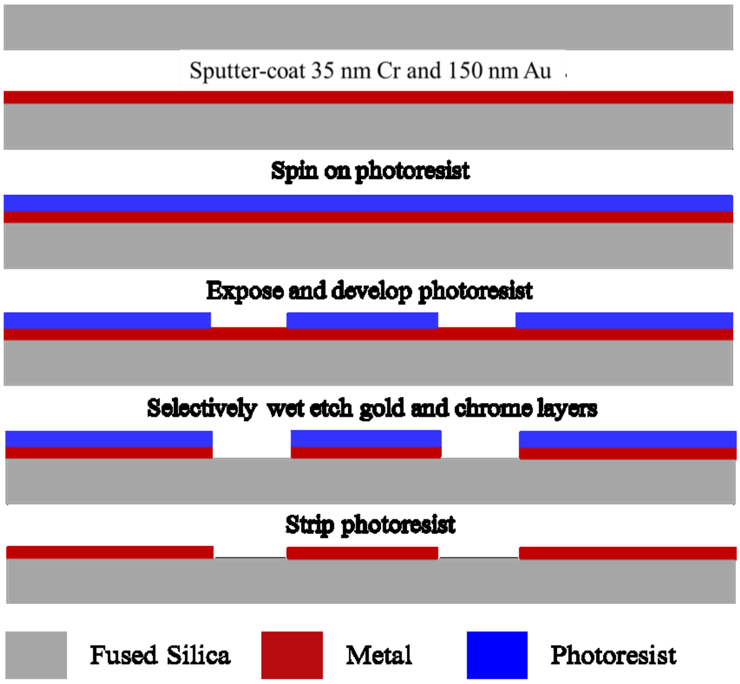


**Figure 33: Micro fabrication processing steps for metal mesh filters**

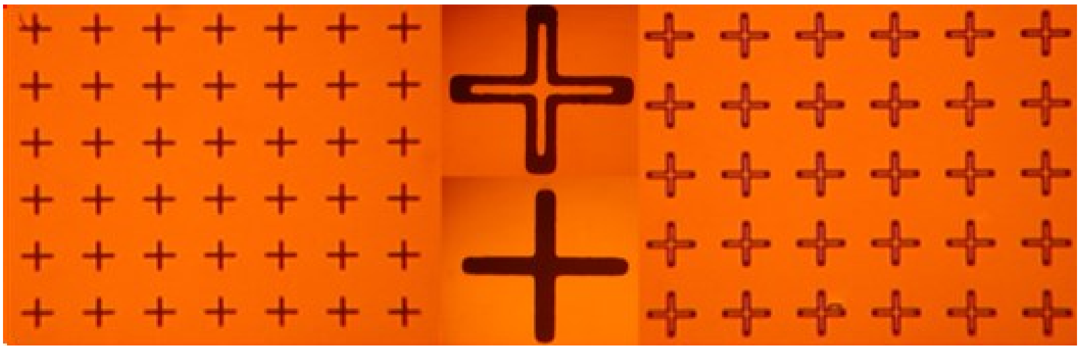

**Figure 34: Microscope image of manufactured filters.**

## 3.3 Measurement Results [*Int. Conf. (3)*]

To measure these filters, the TeraView Spectra 3000 terahertz time-domain spectroscopy (THz-TDS) system was used. The sample were measured within a nitrogen purged chamber, to remove the effects of atmospheric absorption on the measured results [94]. A reference was established by measuring the transmission in the chamber when no sample was present and then the 0.4 THz conventional cross-shaped filter and 0.3 THz trapped-mode design were measured from 0.06 – 3 THz, as shown in Fig. 35. As expected, the conventional 0.4 THz cross-shaped filter shows a pass band at 0.4 THz; however, a second mode at 0.5 THz is also observed. The improved 0.3 THz trapped-mode filter shows better out-of-band rejection, as well as an increase in pass band transmittance.

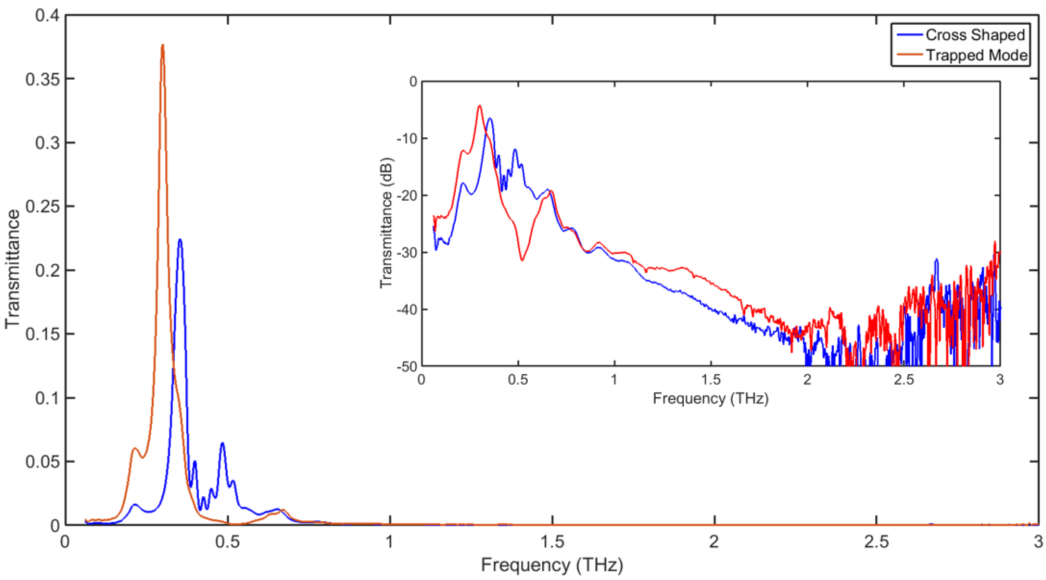


**Figure 35: Transmittance measurements of 0.4 THz cross-shaped and 0.3 THz trapped-mode metal mesh filters in linear unit and insert in decibels.**

## 3.4 Stress Sensor [*Int. Conf. (2)*]

Through simple modification of the THz mesh filter structure, it is possible to produce a THz stress sensor. Figure 36 shows the initial proposed theoretical device for a THz stress sensor [95]. The structure consists of a cross-shape filter embedded within a silicon substrate. Between the rows of filters, at the top and bottom of the unit cell a layer of polyethylene is added, which can compress under stress. This unit cell then forms a 3D array to realise the sensor. The predicted results show that when stress is applied to the structure the filter response is detuned to a lower frequency. If a single frequency is monitored, the change in transmittance is a measure of the stress applied.

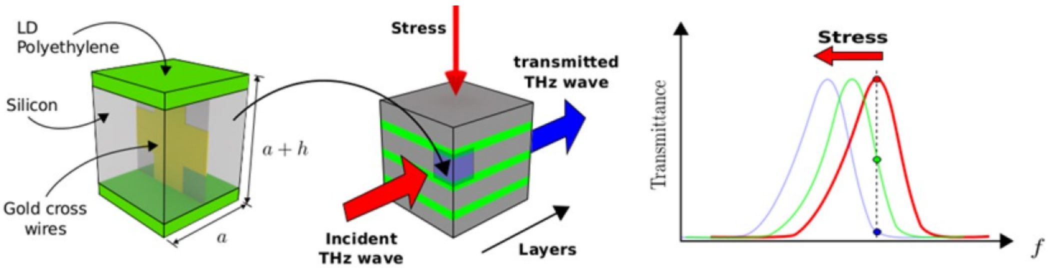


**Figure 36 Proposed THz stress sensor**

Based on this concept, the prototype device shown in Fig. 36 was simulated. This device is designed to be easy to manufacture, to act as a proof of concept. The prototype is designed to operate at approximately 315 GHz. An array of 30 x 30 x 1 unit cells employs 525 μm thick high resistivity silicon substrates with a metal cross filter on one side. The 30 rows of 30 cells are separated by a compression region (having an effective compressive range from ~10 to 60 μm) made from benzocylcobutene (BCB); with BCB also encapsulating the front and back of the complete array. The simulated structure shown in Fig. 37. Compared to the proposed device in [94] this removes the need for silicon wafer bonding to encapsulate the filters in silicon.

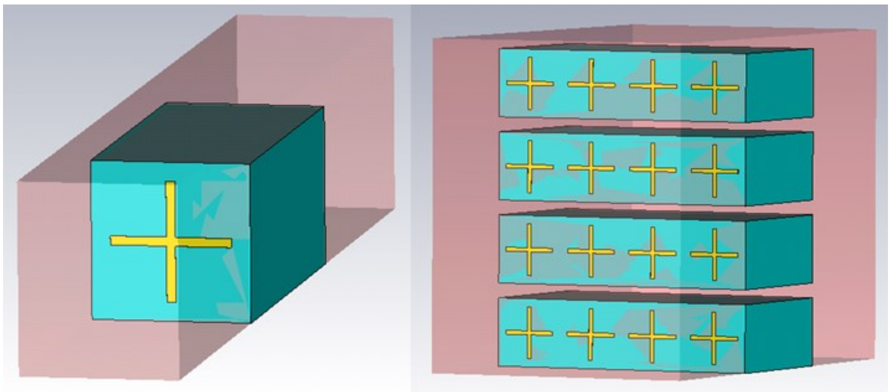

**Figure 37: Simulated single cell (left), small sub-array (right)**

Compression of the BCB, caused by an applied stress, is simulated by reducing the thickness of the BCB region. When the device is compressed, the metal crosses come closer together in the vertical direction; shifting the frequency response of the filter down in frequency, which causes a change in the magnitude of the transmission, as shown by the curve in Fig. 38. An alternative method of measuring stress is to monitor the maximum transmission frequency as the stress is applied; the change in frequency will be proportional to the stress applied.

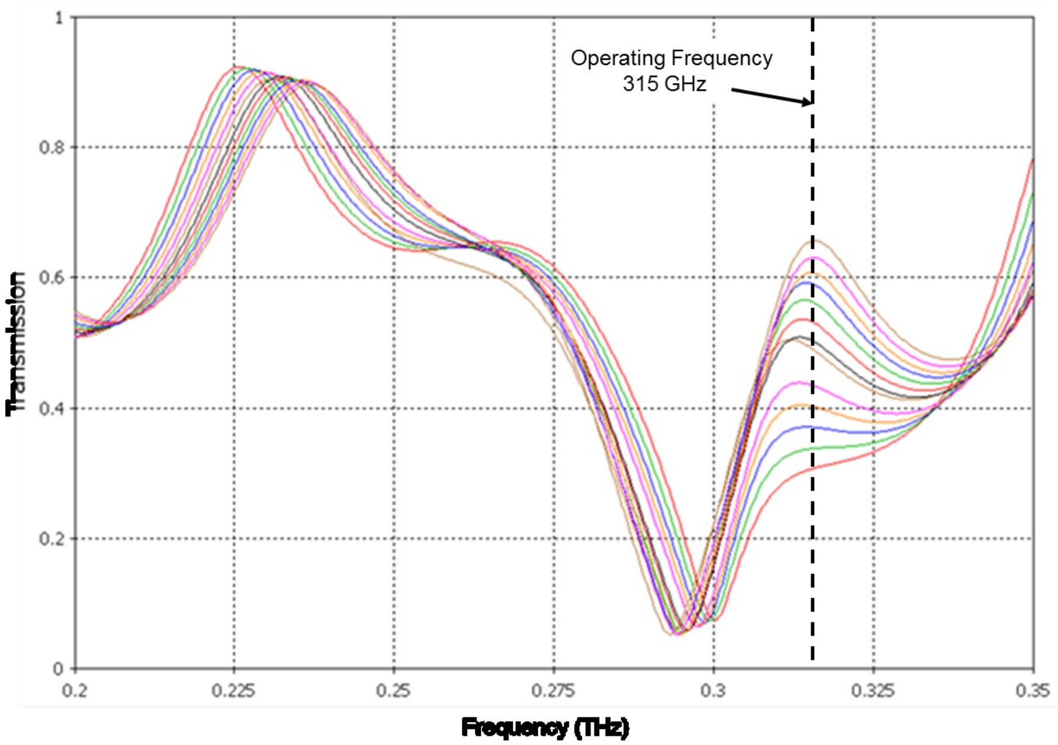


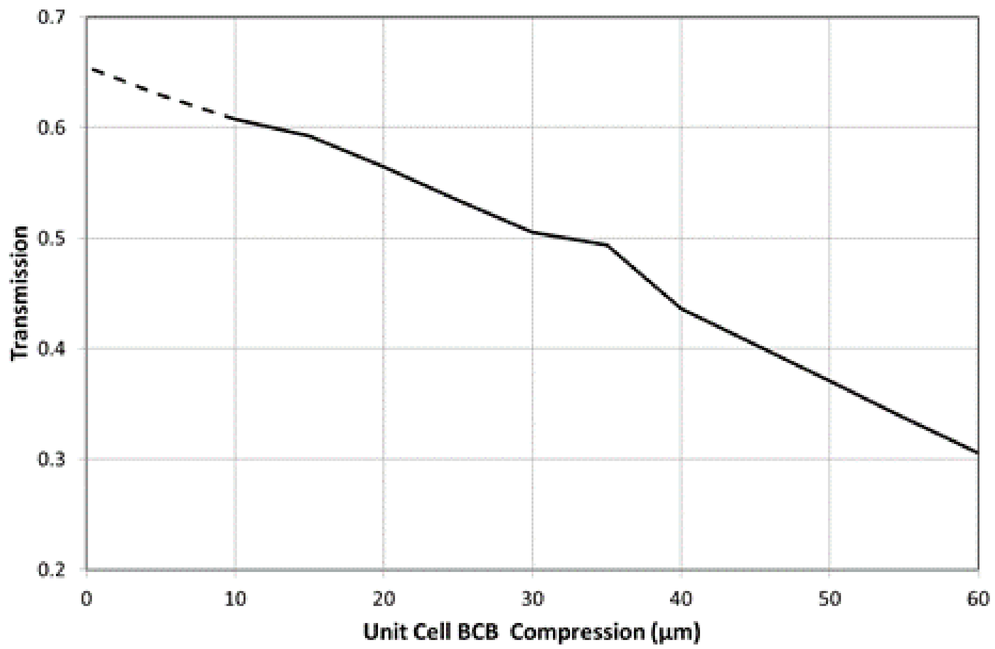


**Figure 38: (top) Simulated frequency response as BCB is compressed and (bottom) Change in transmission at 315 GHz due to compression of BCB**

## 3.5 Further Work

The results shown in this chapter show that a small decrease in the performance of the filter can be traded for a simpler manufacturing method and an increase in the mechanical strength of the filters. This makes them ideal for ubiquitous applications.

A stress sensors has been explored theoretically and requires experimental verification. This will lead to measurement of a prototype device. It is expected that, due to the complimentary nature of the metal mesh filters, the sensor will work in reflection mode as well as transmission, leading to a wide variety of applications. For example the small sensor is embedded within a surface and then a handheld scanner is passed over the surface to map the stress in the surface (e.g. in walls before and after earthquakes).

# 4 Photonic Crystals

## 4.1 Introduction

A photonic crystal is a structure that has an electromagnetic bandgap through an engineered periodic change in permittivity. This could be a 1-D, 2-D or 3-D structure as shown in Fig. 39.

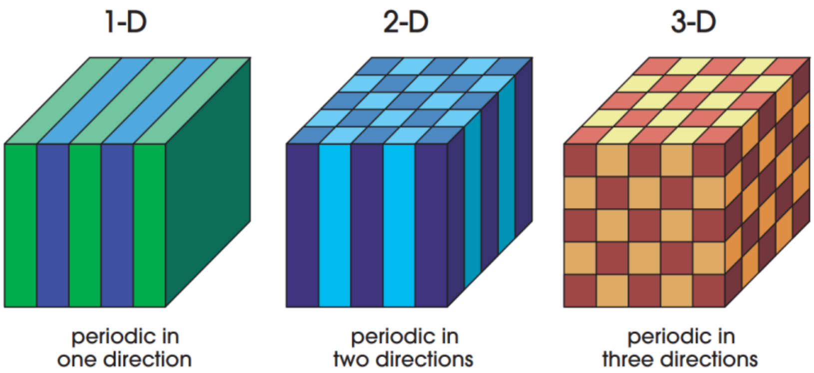


**Figure 39: Examples of 1-D, 2-D and 3-D photonic crystals where the colours represent differing dielectric constant [96]**

The term photonic crystal was coined in the 1980's by E. Yablonovitch [97] and S. John [98], however, the ideas behind photonic crystals have been studied for many years, starting with Bragg mirrors [99]. During the early 1990's initial research was carried out in the microwave frequency band [100], where the capability to easily manufacture devices to prove the theory proposed by Yablonovitch and John [97]-[98]. These structures were large compared to competing technologies and there was no performance advantage to be gained over the then state of the art. As micromaching techniques developed, there was a move to create optical and infrared photonic crystals. A variety of different structures have been demonstrated at optical frequencies, such as waveguides [101], resonant cavities [102] and splitters [103].

The work presented in this chapter brings photonic crystals back down in frequency. The devices demonstrated, waveguides, attenuators, switches and resonators have state-of-the-art performances when compared to current commercial components. These devices provide the basic building blocks required to create more complex THz systems. Conceptual designs to give an idea how the photonic crystals can be used in a future monolithically integrated THz architecture, intended for front-end systems and also show the possibility of photonic crystal biosensors.

## 4.2 Design of Bandgap Structure [*J. (1)*]

The basis for creating high performance photonic crystal devices in the THz band is through the use of a low loss tangent substrate, which also has a high $\varepsilon_r'$. This is to minimize substrate losses in the dielectric and maximize the confinement due to total internal reflection, respectively. A second consideration for the material choice is that devices should be realized using our inhouse microfabrication facilities. This leaves two possible candidates, alumina or high resistivity silicon. An alternative, if there was no limit in manufacturing, would be sapphire, although this is a very expensive substrate choice.

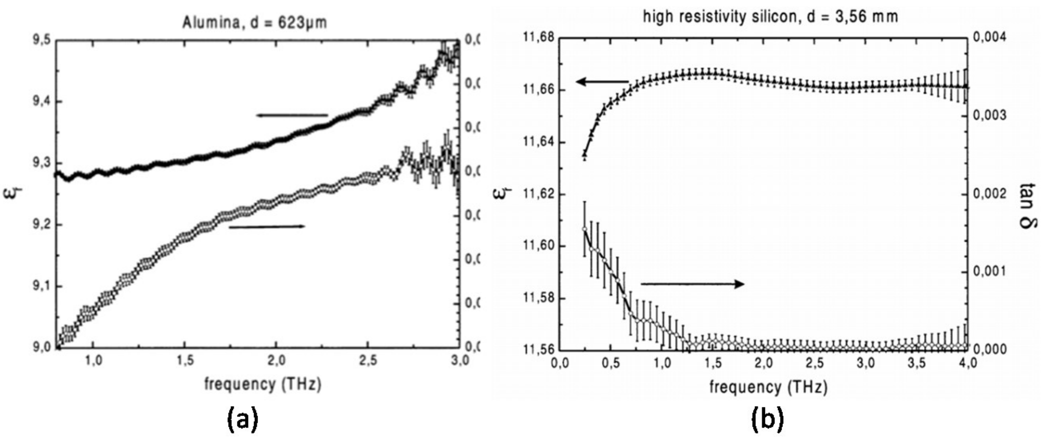


**Figure 40: Measured $\varepsilon_r'$ and $tan\delta_e$ of (a) alumina and (b) high resistivity silicon [104]**

Figure 40 shows $\varepsilon_r'$ and $tan\delta_e$ for both alumina and HRS across the THz band [104]. Both have a high $\varepsilon_r'$ but HRS has a lower $tan\delta_e$ that also decreases as the frequency increases.

This means that as designs are scaled up in frequency (down in size) there will be an improvement in performance due to reduce loss in the substrate.

A second consideration in the choice of material is how the photonic crystals are manufactured. The type of photonic crystal considered are 2D, with a lattice of cylindrical air holes created within the substrate. A trial of laser machined alumina, to create photonic crystals with cylindrical air holes, had previously been performed by Dr S. Hanham. Figure 41 shows that this process causes significant curvature in the sidewall profile. This curvature causes a reduction in the size of the bandgap, as more modes are able to propagate. In contrast deep reactive-ion etching (DRIE) using the Bosch process of a HRS substrate provides an extremely vertical side walled cylindrical air holes, with a similar thickness etch as previously demonstrated in [105].

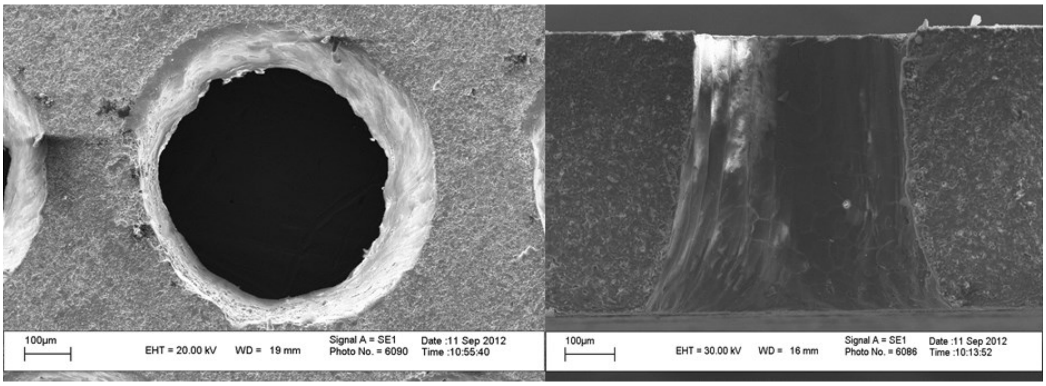


**Figure 41: Photonic crystal holes produced via laser machining alumina**

The choice of HRS as the substrate and the use of the available facilities meant that devices were manufactured from a 100 mm wafer. Without using any thinning processes, thus gives a 525 µm device thickness. From [96], it is determined that using the hexagonal lattice of air holes in the substrate, the devices will operate at around 100 GHz.

To demonstrate that HRS photonic crystals have the potential to operate through the THz band devices would initially be made at W-Band (75-110 GHz), as this is the lower limit of the THz band. As shown in Fig. 40, this is where the material properties for HRS are at their worst, so device performance will only improve as they are scaled up through the THz band.

A hexahedral lattice was chosen for the photonic crystal lattice, as it gives a 'TE like' bandgap [96]. The results of a simulation of an infinite photonic crystal lattice calculated using [106] is given in Fig. 42. The photonic crystal is simulated to be 525 µm thick with 235 µm diameter air holes spaced with a lattice constant of 780 µm. The bandgap for TE like modes lies between 97 and 127 GHz, with a centre frequency at 112 GHz and a fractional bandwidth of 26%. However, TM like modes can still propagate, if excited, as seen in Fig. 42.

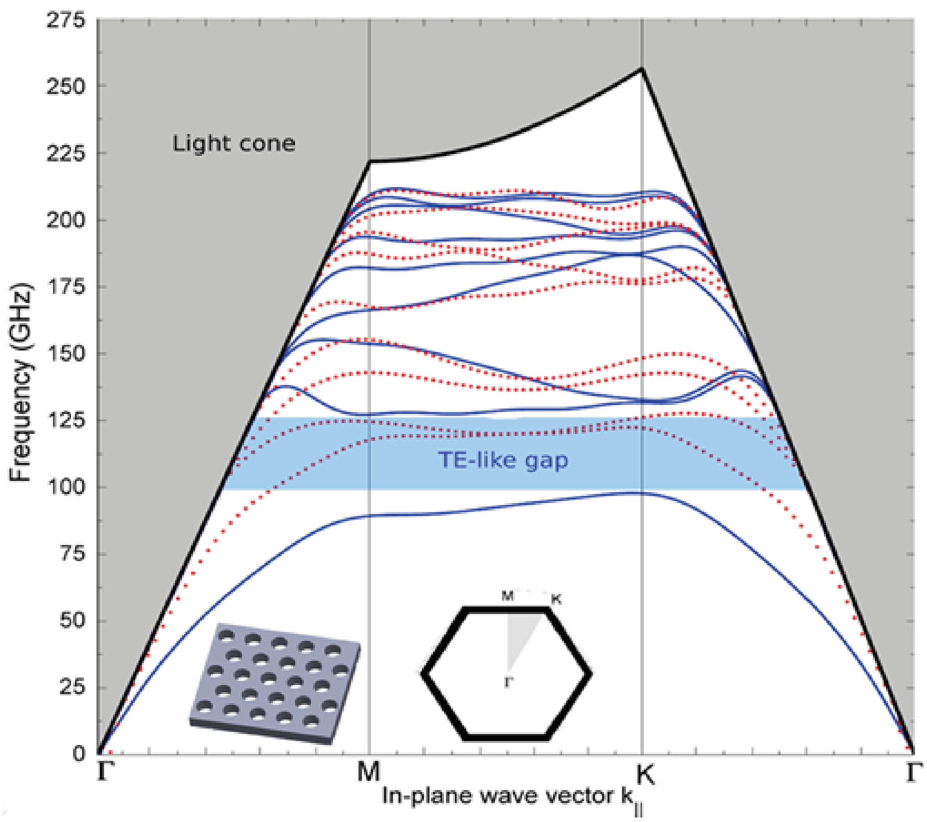


**Figure 42 Band diagram for the photonic crystal design showing the TE-like modes (blue) and TM-like modes (red dashed). The bottom left inset shows the crystal lattice structure and the central bottom inset shows the lattice Brillion zone with the irreducible region shaded grey.**

To experimentally verify the simulations, a method of coupling energy into the photonic crystal needs to be created to interface with the measurement equipment. To measure the device at these frequencies a vector network analyser (VNA) with W-band (WR10) waveguide multiplier heads is required. This means that a transition from MPRWG to photonic crystal needs to be created. As the mode within the photonic crystal is ‘TE like’, the PC should be mounted centrally and vertically at the MPRWG flange to obtain the correct field alignment. A triangular taper that protrudes inside the MPRWG was designed to reduce this mismatch, as seen in Fig. 43, which is 2.1 mm long and 1.2 mm high.

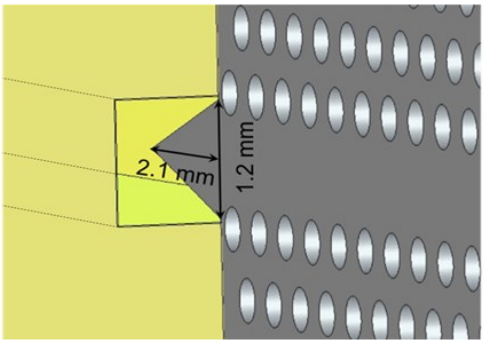


**Figure 43: Illustration showing how the solid triangular silicon taper fits inside the WR10 waveguide in the E-plane at the centre of the aperture.**

A photonic crystal lattice consisting of 11 rows of 20or21 holes, triangular coupling tapers and MPRWG with associated flanges was simulated within CST MWS. This was to confirm that it was possible to measure the predicted bandgap using the VNA. The simulated transmission is shown in Fig. 44, along with E-field magnitude plots. The simulated transmission confirms the bandgap is from 96 to 126 GHz and the E-field plots show that there is transmission above and below the bandgap; there is no transmission in the bandgap, with a noise floor of -50 dB (to be expected).

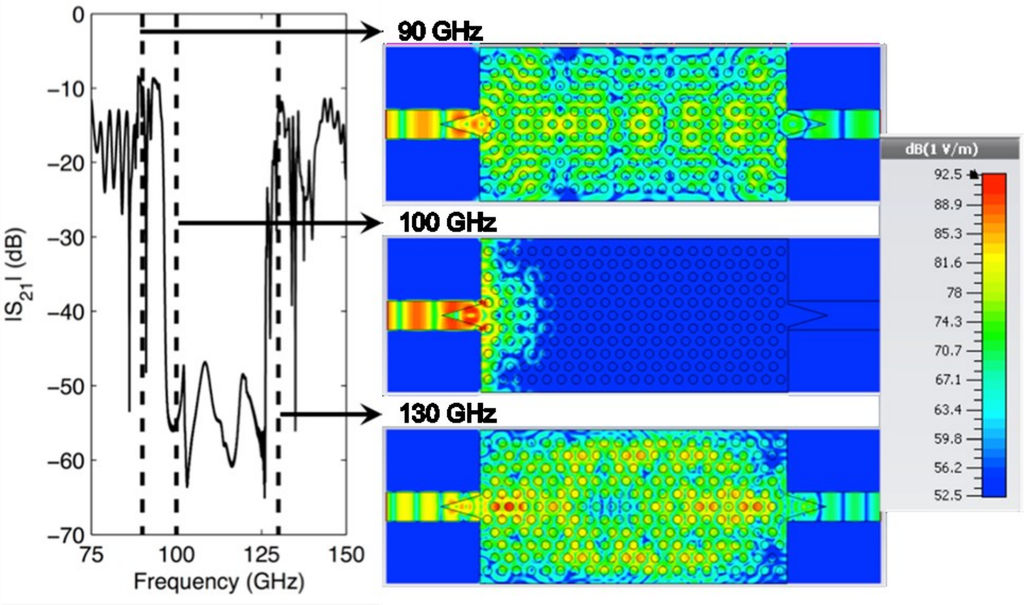


**Figure 44: Simulated transmission demonstrating the band gap with corresponding electric field plots.**

## 4.3 Fabrication Method [*J. (1)*]

The photonic crystals were manufactured using the method outlined here for the bulk micromachining of a 100 mm diameter HRS wafer that was 525 µm ± 5 µm with a resistivity > 10 kΩ·cm. Figure 45 shows the process flow for the fabrication. The first step is to ensure the wafer is clean and all surface contaminants are removed. An adhesion promoting layer (TI PRIME) is then spun on, followed by a ~10 µm thick layer of photoresist (AZ9260); 10 µm is a sufficiently thick layer of photoresist to be used as a soft mask for the 525 µm thru-wafer DRIE, as there is a preferential etch selectivity of 80:1 [105]. The pattern of the photonic crystals to be fabricated was transferred into the photoresist, using standard photolithographic techniques utilizing a low cost acetate mask.

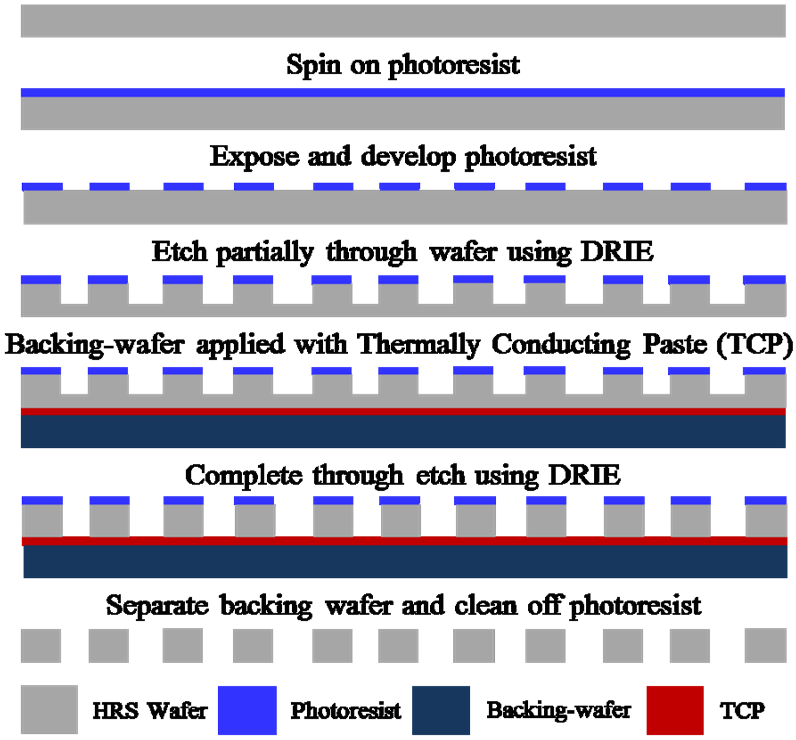


**Figure 45 Microfabrication processing steps for the PC.**

When the photoresist has been fully developed the wafer is then etched within the DRIE system, using the standard Bosch process. This involves an alternating cycle of a plasma etch of $SF_6$ and deposition of a passivation layer of $C_4F_8$. The etch/passivate cycle was continuously repeated until an etch depth of approximately two thirds of the wafer thickness was achieved. At this stage, a backing wafer needs to be applied to the wafer to protect the DRIE systems chuck. The backing wafer used is a low cost single side polished 100 mm diameter silicon wafer. It is attached to the HRS wafer using a thermally conducting paste (TCP) that will dissolve in isopropyl alcohol (IPA). TCP is used to ensure that that the heat generated by the DRIE process is transferred away from the HRS wafer avoiding unnecessary degradation of the selectivity of the photoresist mask.

When the HRS is fully etched through, it is initially visually inspected with the backing wafer still attached, to confirm all holes have been fully etched through. Due to the loading effects of DRIE it is found, as expected, that the holes near the centre of the wafer are etched faster than those at the edge. Once it is confirmed that all holes have been etched through the TCP and remaining photoresist are removed by cleaning with isopropanol, acetone and deionized water.

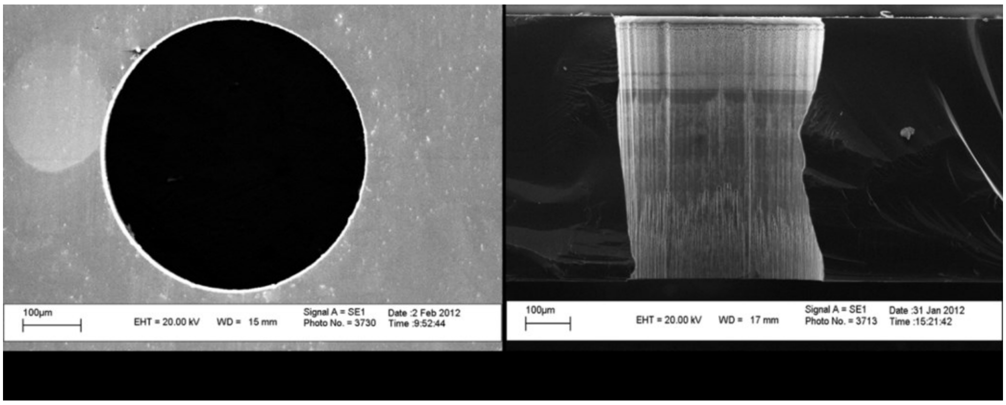


**Figure 46: (a) Etched hole viewed from above; and (b) typical sidewall profile (right).**

Figure 46 shows SEM images of a cylindrical airhole after the etching process. It can be seen in Fig. 46 (a) that the holes exhibit good roundness. Figure 46 (b) shows an image of one of the holes' sidewall. To do this, a samples was cleaved in half through one of the cylindrical holes. The jagged edge in the foreground is due to an imperfect cleave process, but looking at the rest of hole one can see that the sidewall is extremely vertical; however, some surface roughness exists, as expected. This is due to the imperfect circular definition of the acetate mask used, where any defect is propagated down the sidewall of the structure. In future, this could be improved through the use of a more expensive chrome-on-glass mask. When comparing Fig. 46 and Fig. 41, it is clear that the holes created through the DRIE process have achieved a superior sidewall profile, when compared to laser machining.

Various other fabrication methods have been proposed for the creation of photonic crystals. For example, in [107] an alternate approach uses a silicon oxide mask, as it is more selective for DRIE than a soft baked AZ9260 mask. However, this adds further processing steps to grow, pattern and remove the oxide. Moreover, the high temperatures required to grow a thick thermal oxide layer can potentially introduce significant unwanted charge carriers and, thus, compromise the high resistivity nature of the HRS and in so doing reduce the performance of the photonic crystal.

## 4.4 W1 Defect Waveguide

Introducing defects within the PC lattice gives the ability to guide and manipulate the electromagnetic waves within the bandgap region. The simplest and most useful defect is a waveguide. In the photonic crystal lattice, a waveguide is created by the omission of a row of air holes. This form of waveguide is known as a W1 defect waveguide [96].

The device simulated in Fig. 44 was modified to include a W1 defect waveguide by removing the central row of air holes. The results were then recalculated for the W1 defect waveguide structure. These results are shown in Fig. 47. The W1 defect waveguide operates from 102 to 127 GHz. The E-field plots clearly demonstrate that, when compared with Fig 44, transmission still exists through the lattice when the input frequency is below the bandgap. There is still a region of no transmission in the bandgap below the W1 defect cut-off frequency. Finally, it is seen that a mode is guided through the defect, for example at 112.5 GHz. It is of note that there is a standing wave superimposed, seen in $|S_{21}|^2$. This caused by the imperfect impedance match between the triangular tapers of the photonic crystal and the WR-10 waveguides; the waveguide length acts as a weak resonant cavity between the two tapers..

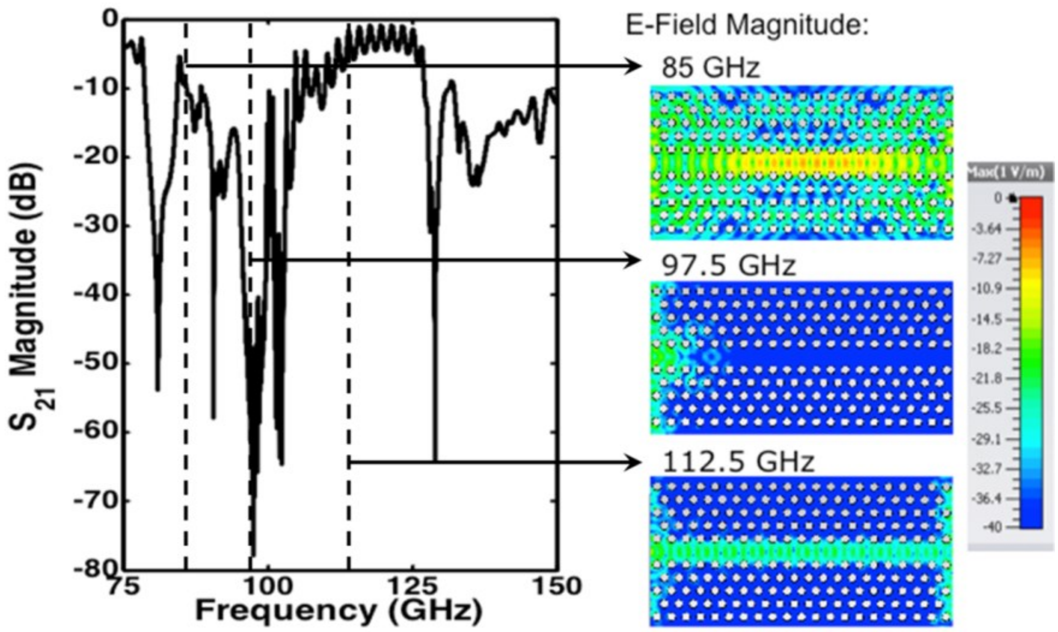


**Figure 47: Simulated W1 defect waveguide demonstrating transmission with corresponding electric field plots.**

A W1 defect waveguide was manufactured and is shown in Fig. 48. The manufactured photonic crystal has more rows of cylindrical air holes than the one simulated. This is due to the size of the simulated structures being limited by the available memory on the workstations (at that time 24 GB of RAM).

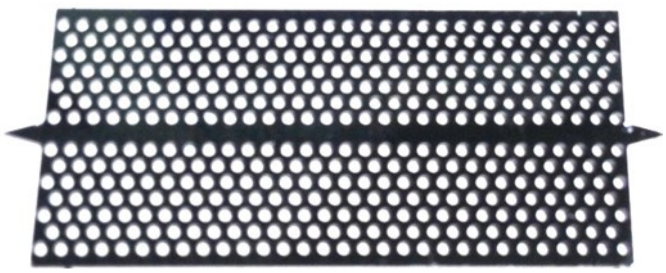

**Figure 48: Photograph of photonic crystal with W1 waveguide defect**

The PC was then measured using the Rohde and Schwarz ZVA-24, with a pair of W-Band (WR-10) frequency multiplier heads attached and calibrated using the TOSM method. This involves measurement of a ‘thru’, where both output waveguide flanges of the multiplier heads are connected to each other so they act as the reference planes of the calibration. A short is then measured on each port, followed by an offset-short, where a shim that is a quarter of a wavelength long at the centre of W-band is added, and finally a match load is measured on both ports. This calibration was performed from 80 to 110 GHz for measurement of the photonic crystal waveguide.

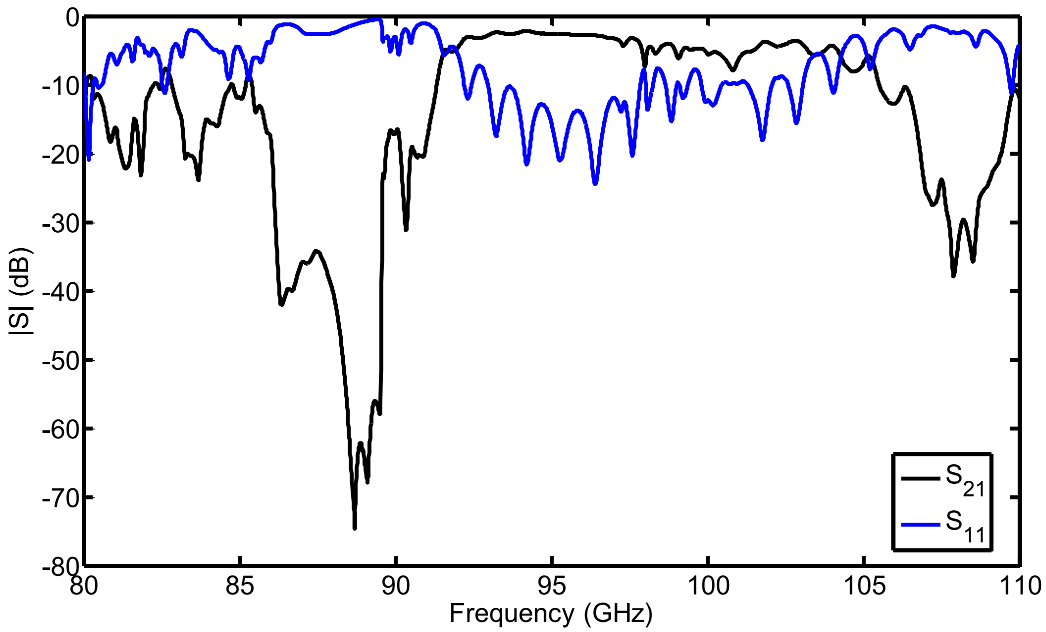


**Figure 49: Measured performance of W1 defect waveguide**

Figure 49 shows the measured results for the photonic crystal W1 defect waveguide. It is seen that the waveguide operates from 92-105 GHz. Measured performance is better than the simulations predict, due to the simulated structures having fewer rows of air holes due to the limited computational power available at the time. It has previously been shown that as the number of rows in a photonic crystal lattice increases there is a better confinement of the waves, due to having more Bragg reflections increasing the confinement of the waves.

## 4.5 Switch/Attenuator [*Int. Conf. (4, 9)*]

To create compact front end systems, for applications such as RADAR that have a single antenna connected to the transmit and receive circuitry, requires RF switches [108]. There are currently two types of millimetre-wave switches that exist commercially: electromechanical switches [109] and PIN diode switches [110]. An electromechanical switch generally provides low insertion loss and high power handling capabilities, but suffers from a limited lifetime due to mechanical fatigue of its moving parts. In contrast, a PIN diode switch has a higher insertion loss and lower power handling capabilities, but as it is a solid-state device it has a theoretically infinite lifetime. As an example of commercially available performance, a Millitech PSP-10 W-band switch has a 10 GHz switchable bandwidth and 25 dB isolation [111].

The HRS substrate of the photonic crystal is photoconductive. This means that the local conductivity can be modulated by optical illumination. The illumination source needs to have a free-space wavelength $\lambda_0 \leq hc/E_g$, where $h$ is Planck's constant, $c$ is the speed of light and $E_g$ the band gap energy of silicon. Such a source will generate free carriers (i.e. electron-hole pairs) within the silicon and hence increase its conductivity [112].

Simulations of the structure were carried out using the commercial electromagnetic modelling software HFSS™. The illumination was modelled as a 2 $mm^2$ circular spot on both sides of the W1 defect waveguide. The 3D conductivity profile of the spot was calculated using numerical simulations from *Silvaco*. The simulated laser operates at 808 nm, with a power density of 80W/$cm^2$. The photonic crystal for these experiments has a slightly lower bandgap than other designs. This is because the initial proof of principle experiments were to be carried out using a Gunn diode source that has an operating frequency of 91.898 GHz. This meant the cut-off frequency of the PC W1 defect had to be reduced. The air holes have a radius of 270 µm and lattice spacing of 900 µm with a standard 525 µm thick HRS substrate. This provides a band gap from 85 GHz to beyond 110 GHz.

Figure 50 shows the simulation results. It is clearly seen that a band gap extends from 85 GHz upwards, and the W1 defect waveguide operates over a range of 88 to 98 GHz with less than 1.5 dB of insertion loss predicted. When the laser is illuminating the substrate, the insertion loss increases to over 44 dB, which represents a greater than 40 dB reduction in power transmission through the crystal.

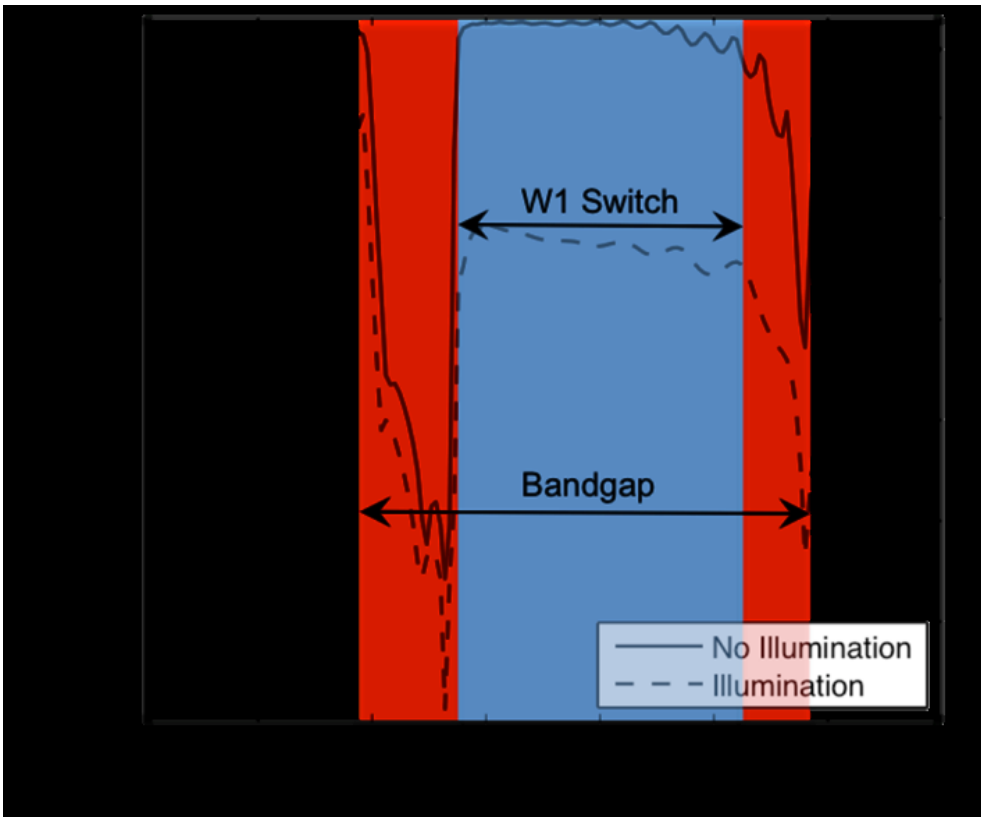


**Figure 50: Simulated results across W-Band for the switch in the 'ON' (no illumination) and 'OFF' (illuminated) states.**

To experimentally verify theses simulations, the setup shown in Fig. 51 was used. It consists of a 91.898 GHz Millitech GDM-10-0-17H WR10 Gunn diode source with an external isolator attached. The PC is then inserted between the isolator and a Millitech DXP-10 Schottky barrier beam lead diode detector. As with all the experimental setups using the PC, it sat centrally within the waveguide so it is at the field maximum and the coupling tapers protrude fully inside the MPRWG. The output of the detector is measured using a Marconi Instruments VSWR meter, having an internal variable attenuator. The laser illumination is provided by a pair of IPG Photonics PLD-33 laser diodes, which produce a spot diameter of ~1.5 mm on each side of the PC, as shown in Fig. 52.

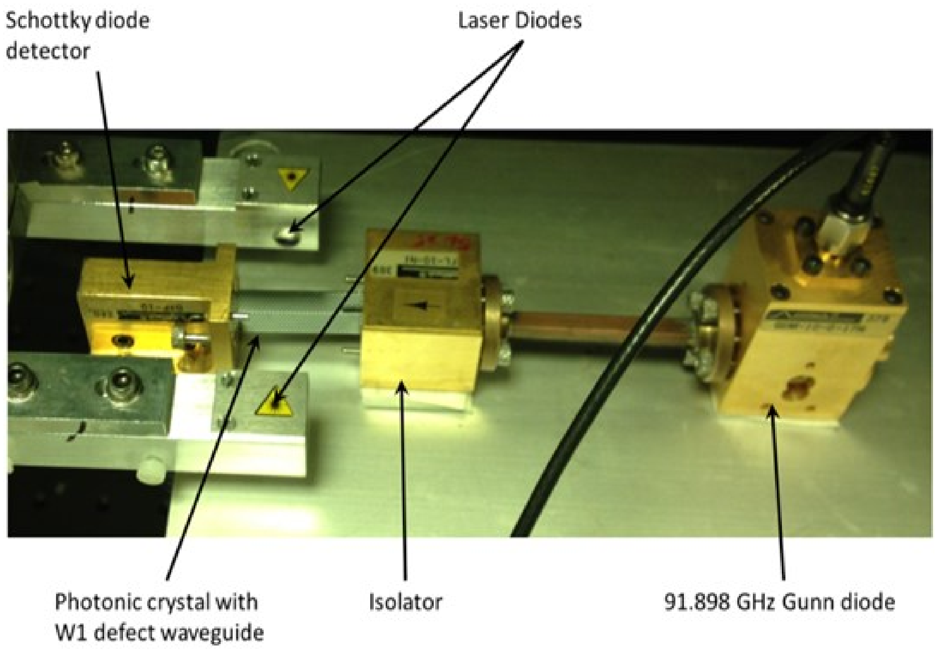


**Figure 51: Measurement Setup**

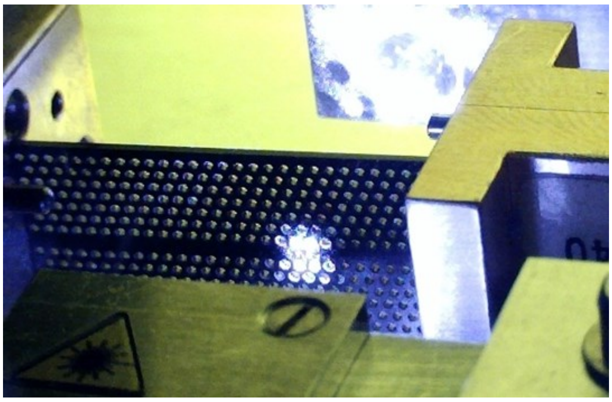

**Figure 52: Laser illumination spot on one side of the photonic crystal (as seen through an infrared/optical camera)**

A reference for transmission measurements was established by removing the PC and connecting the isolator directly to the detector.

The laser current was swept from 0 to 1 A, to obtain the switching performance of the PC, with the measured results shown in Fig. 53. It can be seen that an extinction ratio of

40.1 dB exists between the ON and OFF states, which is in good agreement with the simulation data presented in Fig. 50. Figure 53 also shows that the illuminating power required from the laser, to significantly switch the PC waveguide, is ~100 mW. It can be seen that as the laser power increases beyond this, the transmission drops further, as the local conductivity in the silicon increases further, but then saturates at -40.1 dB. This represents the background level of the other leakage radiation paths through the PC.

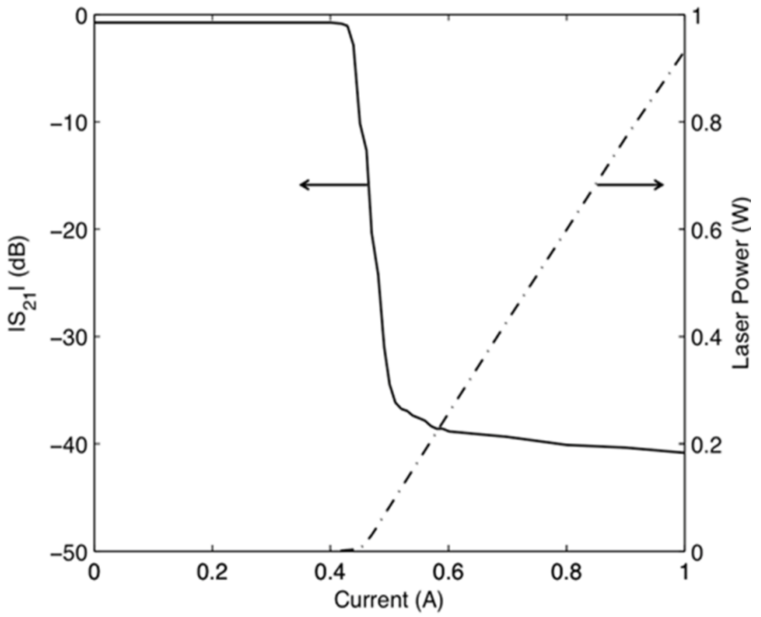


**Figure 53: Measured data showing how transmission through the W1 defect waveguide and laser power vary as the current through the laser increases.**

Equation (17) in [113] describes the profile of the free carriers generated by the laser illumination within the silicon at the centre of the beam spot. This was plotted with several different laser illumination powers in Fig. 54 for the dual-sided illumination used in experiments. It is clearly seen that as the illumination power density increase a larger number of free carriers is generated. This means that the conductivity increase is greater within the silicon and a better isolation of the switch can be expected, thus creating an attenuator. However, as seen with the W1 defect PC waveguide, the noise floor of the photonic crystal is around -50 dB.

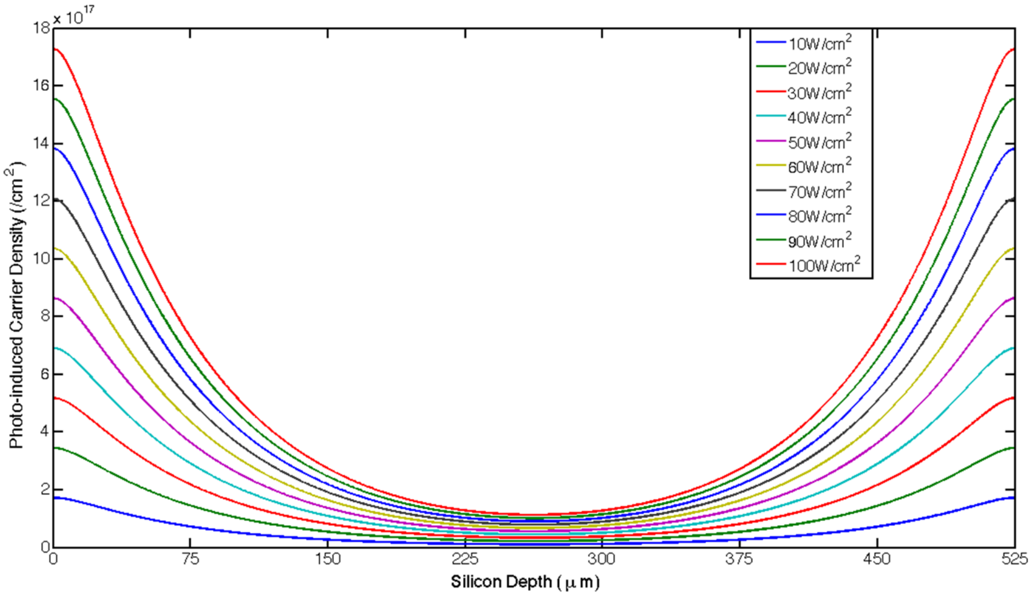


**Figure 54: Photo induced carrier density for a dual-side illumination at the centre of the illumination spot as the laser power increases.**

The measurement setup in Fig. 55 was used to demonstrate the photonic crystal attenuator by gradually increasing the illumination power of the laser from 80-110 GHz. As with the W1 defect PC waveguide, the VNA was calibrated across this range using a TOSM calibration.

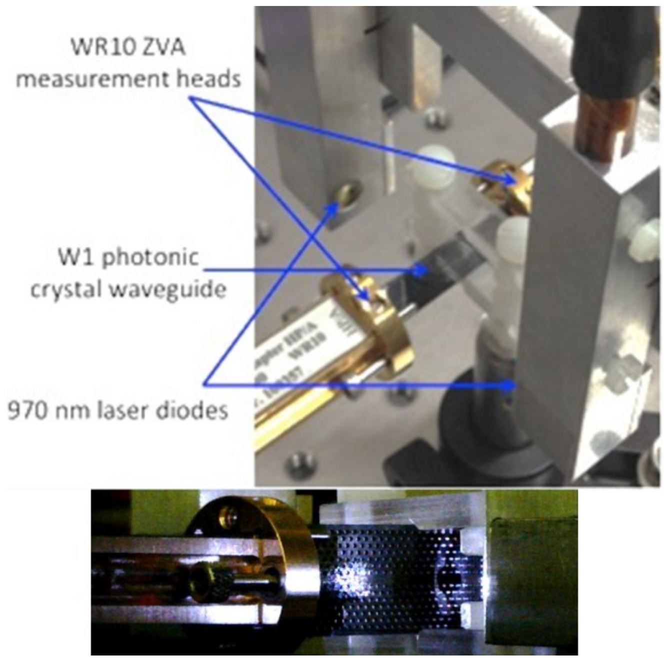


**Figure 55: Measurement setup and laser spot seen through an infrared camera**

The measured S-parameters for the PC are shown Fig. 56. It can be seen that >45 dB of attenuation is achieve across the operating band of the W1 defect PC waveguide, from 92 to 102 GHz and >60 dB from 92 to 94 GHz. This attenuation is greater than that predicted in simulation having a smaller spot size. The S-parameters indicates a standing-wave resonance when there is no illumination; this was also seen in simulations. This phenomenon is caused by the electromagnetic impedance mismatch between the WR10 and W1 defect waveguides. This is not seen when the W1 defect is illuminated, because the signal energy is scattered from the plasma through the lattice, rather than reflected back to the input port. As a result, |S11| does not change significantly under illumination.

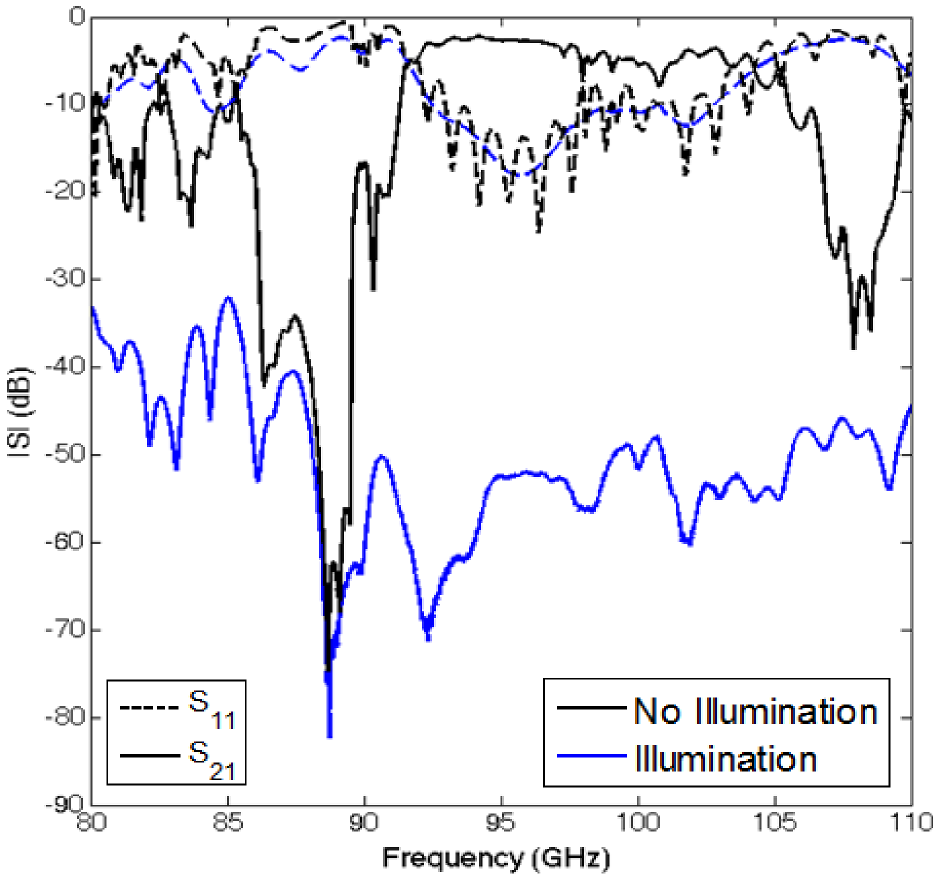


**Figure 56: Measured S-parameters for the attenuator with no illumination (inherent insertion loss) and with illumination (maximum insertion loss).**

Figure 57 shows the measured performance of the variable attenuator. It can be seen that the insertion loss gradually increases as the laser power is increased; this characteristic is relatively uniform across the operating band, until undesirable free-space transmission paths between the ports dominate the measurements. For example, Fig. 58 shows the performance of the variable attenuator at 93 GHz. Here, the inherent insertion loss is 2.79 dB (without illumination) and the maximum insertion loss is 64.32 dB (with a combined laser power of 150 mW, illuminating both sides of the W1 defect waveguide), yielding a variable attenuator having a dynamic range of >61 dB.

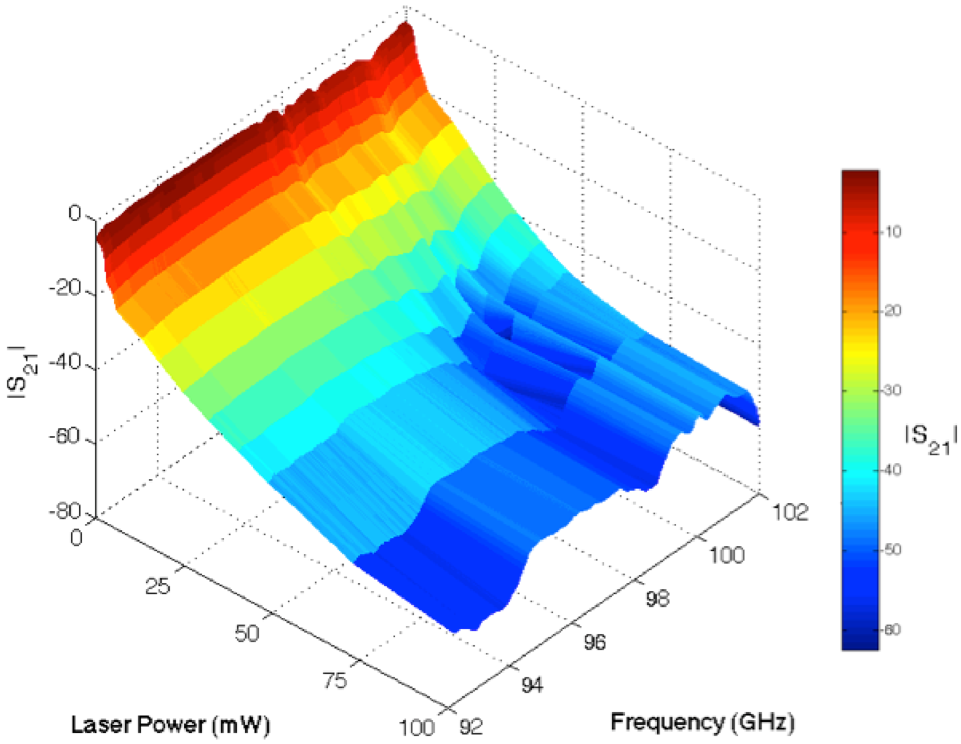


**Figure 57: Measured insertion loss across the 92-102 GHz operating band as laser power is increase from 0 to 100 mW.**

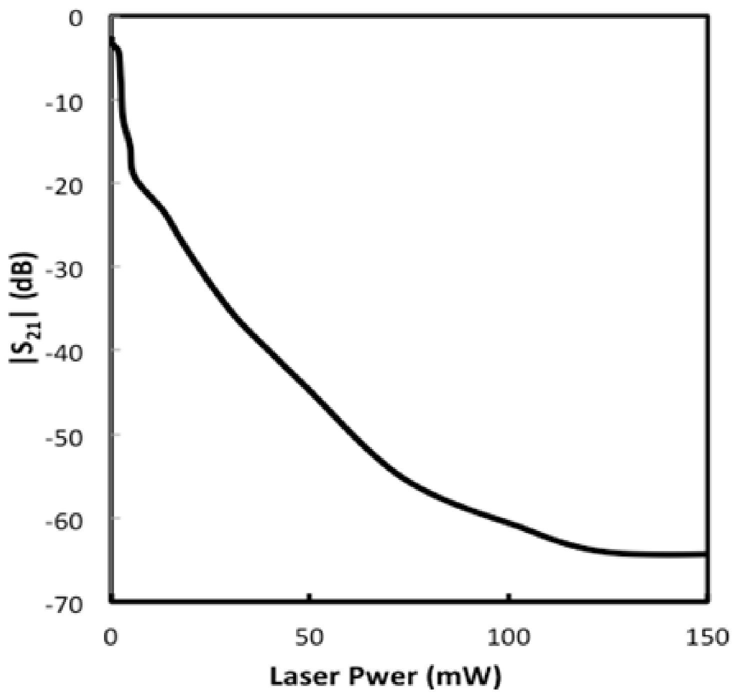


**Figure 58: Measured insertion loss at 93 GHz.**

## 4.6 Resonator [*J. (1)*]

Waveguides, switches and attenuators a have been demonstrated. The next logical component is a high Q-factor resonator. High Q-factor resonators can be used to realize important components for future millimetre-wave and terahertz communication and radar systems, such as low phase noise oscillators and band pass filters.

A number of approaches for realizing a sharp resonance in an integrated terahertz system have been reported in the open literature, including: whispering gallery resonators, PCs, parallel-plate waveguide with periodic grooves, micro-cavity resonators side-coupled to waveguides and metamaterial approaches. A comparative summary of the associated Q factors reported by others at a similar frequency is given in Table 4. It should be noted that the methodology used to calculate Q is often not described within references and, therefore, care must be taken in their interpretation.

**Table 4 Comparable (sub)-millimetre-wave resonator technologies**

| *Resonator Technology* | *Frequency(GHz)* | *Q-factor* |
|---|---|---|
| Quasi-metallic silicon PC [114] | 90 | 25 |
| Whispering gallery mode [115] | 240 | 3,000 |
| Grooved parallel-plate waveguide [116] | 491 | 240 |
| Split-ring array [117] | 1,000 | 10 |
| Antenna array [118] | 1,000 | 20 |
| Waveguide micro-cavity [119] | 1,300 | 40 |
| PC filled waveguide [120] | 1,460 | 133 |

This section describes how an L3 defect cavity [121] (removal of three air holes), can be introduced within the photonic crystal structure to achieve a high Q-factor resonator through simulation and measurement.

### 4.6.1 Design and Simulation

The aim is to create a resonant cavity at ~100 GHz. To achieve this the hexagonal lattice of air holes within a 525 μm HRS substrate was used, with a radius of 235 μm and a lattice constant of 780 μm. These dimensions give a band gap with a centre frequency of ~112 GHz with a 26% fractional bandwidth, as previously shown in Fig 42.

The resonant cavity is produced by the removal of three air holes, creating what is known as an L3 defect. It has previously been shown at infrared frequencies that by shifting the position of the holes near the cavity it is possible to achieve extremely high Q-factors by reducing the out-of-plane radiation losses [121]. The hole positions A, B, and C in Fig. 59 are moved away from the cavity by 156 μm, 19 μm and 156 μm, respectively, allowing the fields to penetrate further into the crystal cavity, thus confining them more gently. It can be shown that, through a plane-wave expansion of the fields within such a cavity, this delocalisation of the fields results in a narrowing of the spatial spectral domain. This narrowing greatly reduces the components of the in-plane wavevector vector $k_{||}$ that do not satisfy the condition for TIR (i.e. $0 < k_{\|} \leq 2\pi/\lambda_0$, where $\lambda_0$ is the free-space wavelength) and, therefore, contribute to radiation loss. Further details of this effect can be found in [121] and [122].

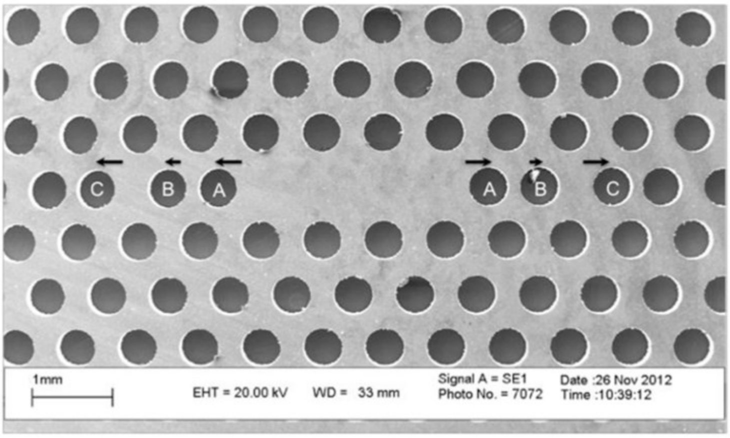


**Figure 59: Fabricated L3 cavity defect. Holes A, B and C are shifted away from the cavity by 156 µm, 19 µm and 156 µm, respectively.**

To couple energy into the cavity, a W1 defect feed waveguide was created by omitting a partial row of adjacent holes in the PC lattice. Three different W1 defect waveguide configurations were considered – one with the W1 defect feed waveguides inline below the cavity. The other two have the feed waveguides offset above and below the cavity, to reduce mutual coupling. With the offset configuration, two different lengths of W1 waveguide were considered, to provide weak and strong coupling to the cavity, as shown in Fig. 60. A weak coupling provides a better estimation of the unloaded Q-factor as $Q_0 = Q_L/(1-\kappa)$ [123], where $Q_L$ is the loaded Q-factor and $\kappa$ is the coupling factor. This means that, for the weakly coupled PC with a resonant peak at -40 dB $Q_L$ will be within 1% of $Q_0$. As with the previous experiments, a triangular taper is added to the W1 waveguide defect to enable coupling from the MPRWG to the W1 defect mode.

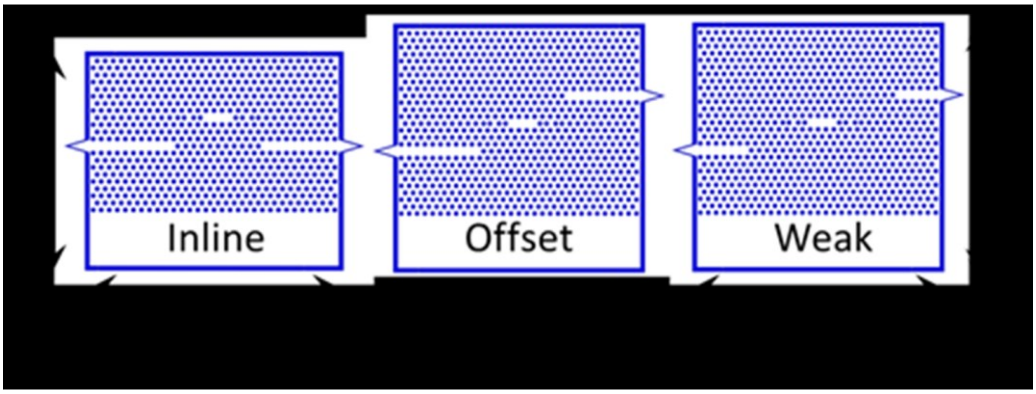


**Figure 60: Three PC resonator designs with the blue dots denoting air holes in the white HRS substrate. The left design has the excitation W1 defect feed waveguides inline and the other two have the offset configuration. The resonator on the right is weakly coupled**

Numerical simulations were run with both strongly coupled PC designs for the entire structure; although sufficient computing power was not available to run the weakly coupled designs. The simulations were initially performed with the silicon having a loss tangent of zero. The resulting S-parameters, shown in Fig. 61, show the sharp resonances (as expected). A frequency shift is observed between the two resonator designs, despite the cavities having the same dimensions. This is caused by the different meshes created by the simulation solver. This could not be further refined, due to our limitations in computational resources (currently having twelve 3 GHz cores and 128 GB of RAM). The introduction of dielectric losses, having an effective loss tangent of $tan\delta_e \sim 10^{-4}$ for a HRS resistivity of 10 kΩ·cm [124], causes the insertion losses to increase and a broadening of the resonant peaks, as shown in Fig. 62. This demonstrates that the Q-factor of these structures will be ultimately limited by dielectric losses.

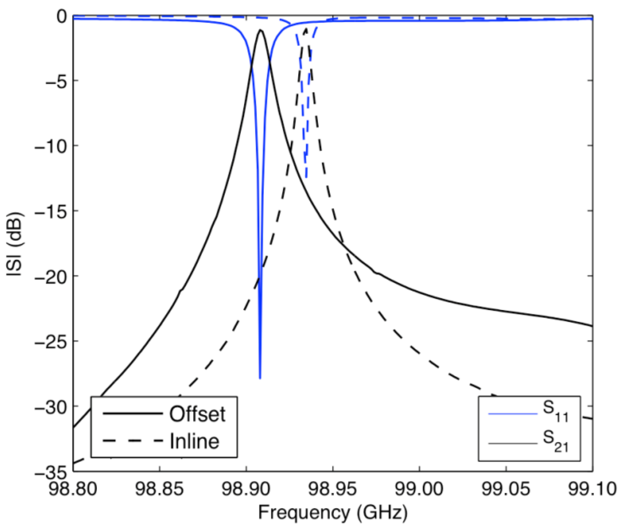


**Figure 61: Simulated S-parameters for strongly coupled PC resonators having zero effective loss tangent silicon.**

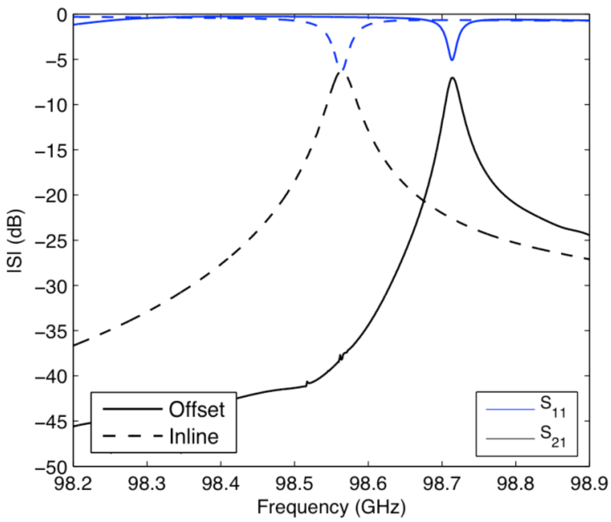


**Figure 62: Simulated S-parameters for strongly coupled PC resonators with tanδ$_e$ = 10$^{-4}$**

The Q-factor for both sets of simulations were calculated using two methods derived from the circuit analysis of RLC tuned circuits for the loaded Q-factor ($Q_L$) of a resonator, and a basic formula to determine the unloaded Q-factor ($Q_0$) from $Q_L$. Equation (34) describes how $Q_L$ is derived from the -3 dB bandwidth, where $f_0$ is the resonance frequency, $f_u$ and $f_l$ are the upper and lower frequencies, respectively, defined where the power of a signal drops 3 dB below that at resonance. Equation (35), defines how $Q_L$ is obtained from $\angle S_{21}$, transmission phase, where $\omega = 2\pi f$. Finally, Equation (36) is used to extract $Q_0$

$$Q_L(f_0) = \frac{f_0}{f_u - f_l} \tag{34}$$

$$Q_L(f_0) = \frac{\omega_0}{2}\left|\frac{\delta\angle S_{21}}{\delta\omega}\right|_{\omega=\omega_0} \tag{35}$$

$$Q_0(f_0) = \frac{Q_L(f_0)}{1 - |S_{21}(f_0)|} \tag{36}$$

Table 5 shows the calculated Q-factors for the simulations. As can be seen from the S-parameters for the lossless case, the unloaded Q-factors are up to ten times greater than for the simulations that include the substrates dielectric losses. It is well known that for dielectric only resonators, the associated dielectric material loss $Q_D \propto (\varphi\ tan\delta_e)^{-1}$, where $\varphi$ is the dielectric filling factor. If it is assumed that the dielectric filling factor is close to unity and $tan\ \delta_e = 10^{-4}$, this gives a fundamental limit on the Q factor at 100 GHz of ~10,000. As seen from the lossy simulations, the cavity Q factor is approaching this limit.

**Table 5: Simulated Q-Factors**

| *Resonator* | *3 dB $Q_L$* | *Phase $Q_L$* | *3 dB $Q_0$* | *Phase $Q_0$* |
|---|---|---|---|---|
| Lossless Offset | 8 830 | 8 860 | 72 330 | 72 550 |
| Lossless Inline | 10 370 | 10 440 | 91 750 | 92 370 |
| Lossy Offset | 4 550 | 4 800 | 8 190 | 8 640 |
| Lossy Inline | 4 840 | 5 010 | 9 420 | 9 750 |

Figure 63 shows the E-field magnitude within the PC resonator at 99.4 and 98.755 GHz, with the cavity being off-resonance and at resonance, respectively. It clearly illustrates how the energy is coupled through the cavity from the input to the output W1 defect waveguide and the enhancement of the field inside the cavity.

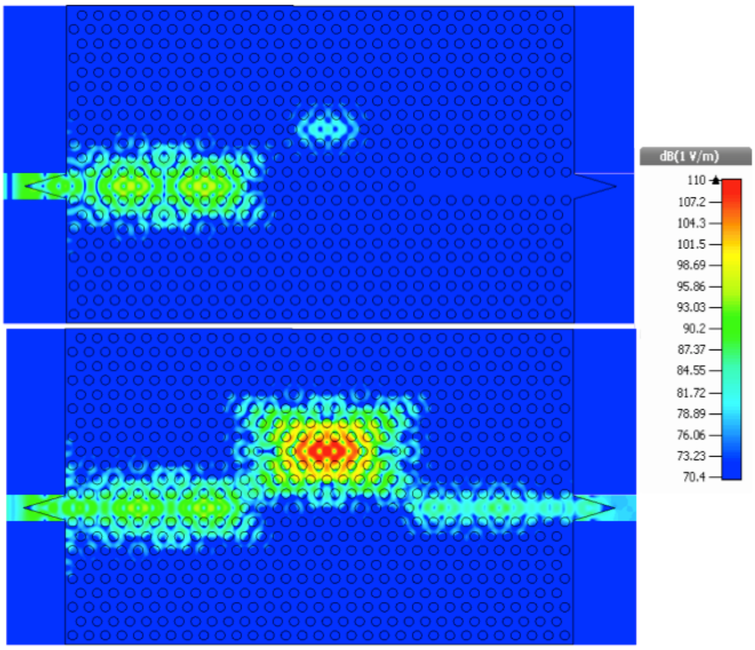


**Figure 63: E-field magnitude plots showing the cavity excited away from resonance (above) and at resonance (below).**

### *4.6.2 Experimental Measurement*

S-parameter measurements were carried out using a vector network analyser configured with a pair of WR10 waveguide frequency multiplier heads that cover the complete W-band (i.e. from 75 to 110 GHz) at the UK's National Physical Laboratory

Measurements were undertaken by first performing a Thru-Reflect-Line (TRL) calibration [125] with the waveguide flange of the frequency multiplier heads defining the reference planes. The calibration employs WR10 waveguide standards: a thru connection; a quarter-wavelength section of line, to provide a 90° phase change in the middle of the waveguide band (with a waveguide length of approximately 1.08 mm); and a flush short-circuit as the reflect standard connected in turn to each reference plane. The calibration was performed using an external calibration algorithm, employing a seven-term error-correction routine [126]. The overall set-up used (i.e. VNA, primary standards and calibration algorithm) is referred to as the NPL Primary Impedance Microwave Measurement System (PIMMS) [127], [128]. This is the UK's primary national standard system for S-parameter measurements and is described in [129] for millimetre-wave waveguide measurements.

For resonator device measurement, the PC coupling taper was aligned with the centre of each waveguide frequency multiplier head, penetrating inside the waveguide aperture, so that the PC sat flush with the waveguide flange, as shown in Fig. 64. The fabricated resonators differ slightly from the simulated structures. An extra extension of bulk HRS substrate was added to the bottom of the PC, so that the structure could be physically held in position and accurately aligned using a micrometre-controlled linear stage.

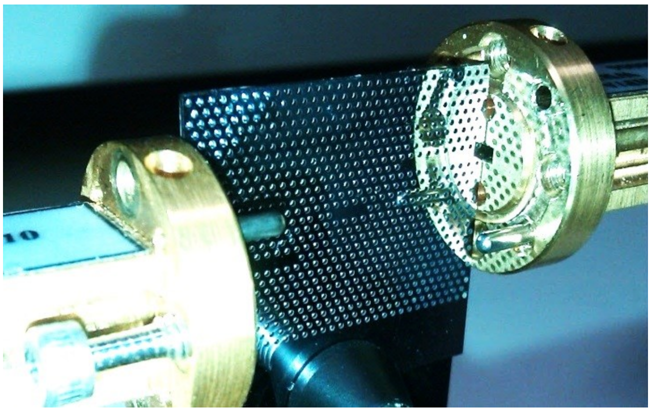

**Figure 64: Experimental measurement setup showing how the PC resonator devices are mounted between two WR10 rectangular waveguide frequency multiplier heads.**

The first measurement undertaken was a broadband transmission sweep of a single PC resonator, from 85-110 GHz with a frequency sample interval of 100 MHz. This was to prove the expected band gap of the PC. From Fig. 65, it can be seen that there is a 20 dB drop in transmission above 96 GHz, extending to the 110 GHz recommended measurement limit for the WR10 waveguide VNA. A peak at approximately 99 GHz is seen, which corresponds to the resonance caused by the cavity; the full peak cannot be resolved due to the coarse frequency sampling interval.

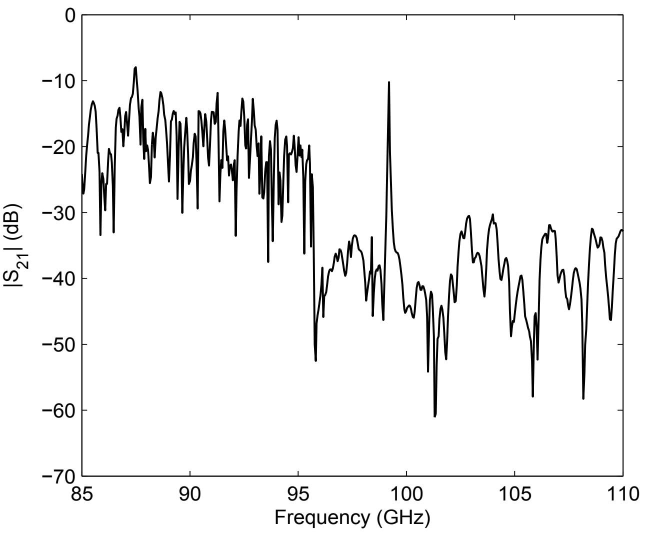


**Figure 65: Broadband transmission response showing the resonance of a strongly coupled 99 GHz offset PC resonator.**

Fig. 66 and Fig. 67 show the measured $|S_{11}|$, $|S_{21}|$ and $\angle S_{21}$ responses between 99.05 and 99.25 GHz, with 1 MHz resolution, for the three manufactured resonators illustrated in Fig. 60. It is seen that there are variations in the insertion and return losses of the two strongly coupled PC resonators. This is caused by the mechanical alignment between the PC tapers and the centre of the WR10 waveguide apertures. Therefore, this is not an inherent limitation, as there is a great deal of scope to create mechanically and electromagnetically optimal transitions between the calibration reference planes and the associated W1 defect feed waveguide for such ultra-high Q-factor DUTs (devices under test). For example, a housing could be machined to hold the photonic crystal which includes the interface with the flanges. However, moving forward beyond the prototype device to the goal of a fully monolithically integrated technology, MPRWG to W1 defect transitions will not be used; instead focus on stripline or microstrip to W1 defect transitions would be of greater use.

The weakly coupled resonator has a resonance peak and phase slope that are differing in shape, when compared to the strongly coupled resonators. This is because the peak at

-45 dB is the result of the superposition from the resonant cavity and other coupling paths, which are at a comparable level (as seen in Fig. 65). These alternate coupling paths are the free space paths between the two-waveguide heads.

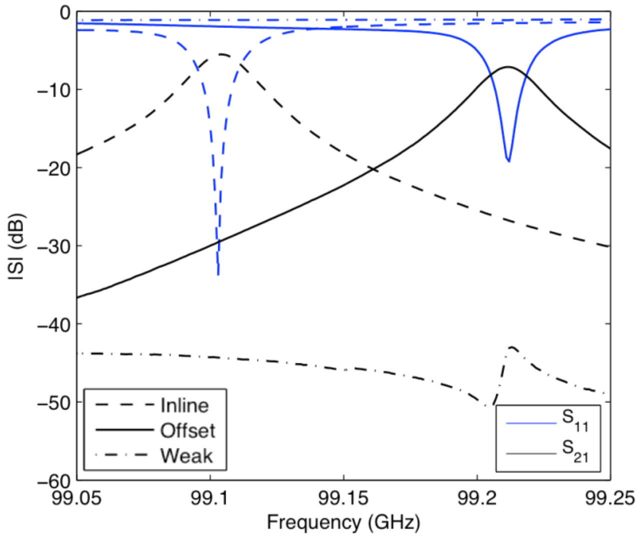


**Figure 66: Measured S-parameter magnitude responses for the PC resonators close to the resonant frequency.**

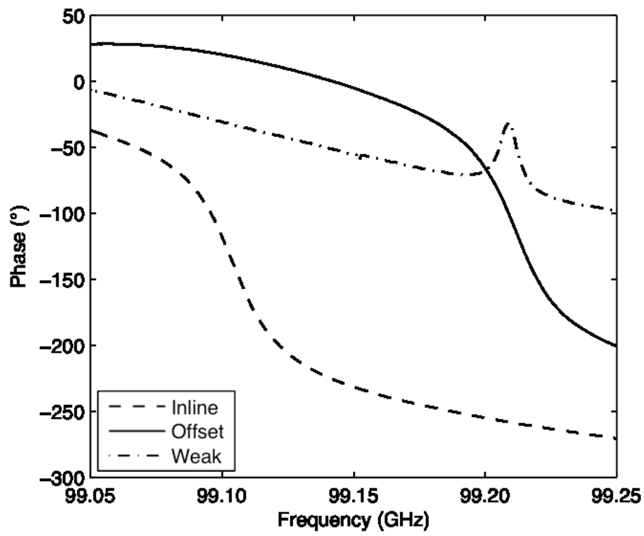


**Figure 67: Measured transmission phase responses for the PC resonators close to the resonant frequency.**

There is a slight variation of resonant frequency across the fabricated PCs, from 99.10 to 99.22 GHz (i.e. 0.12%). There are two causes for this variation; the first is that the

DRIE etch is possibly not completely consistent across the wafer and secondly, the definition of the acetate mask lithography is not within tolerance. Both of these could cause a minute variation in hole size; simulations show that an increase in hole diameter will increase the resonant frequency upwards. To minimize this variation in future work, the bulk micromachining process could be modified. For example, a chrome-on-glass mask or packing pieces could be employed. The former has a greater resolution, giving better defined circles [105]. The second cause of this variation could be variation of the material properties across the wafer. As the wafers are produced by the float zone method, the resistivity is not consistent across the whole wafer. Figure 68 shows a typical resistivity profile of a commercial Topsil HRS wafer, where there can be ± 6% variation across the wafer [130].

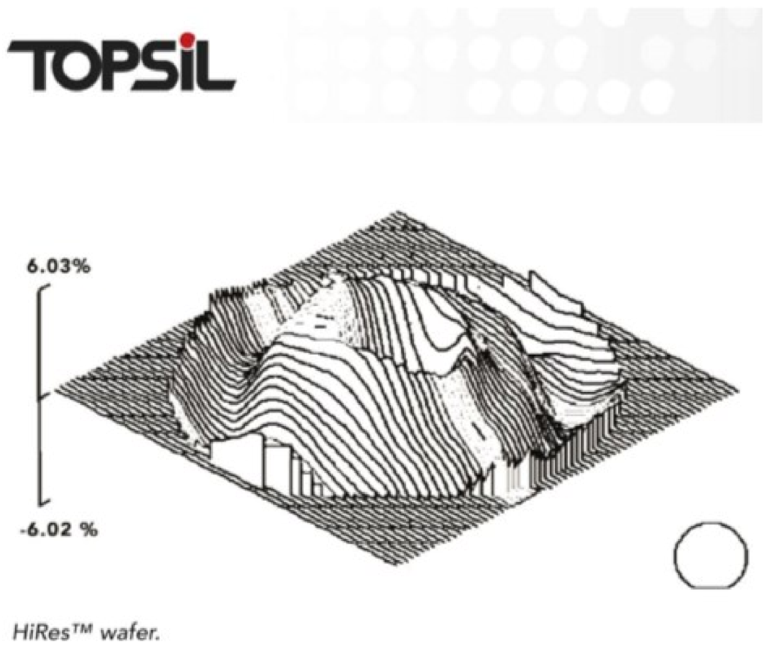


**Figure 68: Typically HRS wafer resistivity variation [130].**

Table 6 shows the measured Q-factors calculated using the methods described by (34)-(36). The measured unloaded Q-factor varies from 7,140 to 10,200. This variation is to be expected; as previously mentioned, due to the variation in coupling alignment at the

WR10 waveguide heads and also the variation of HRS resistivity, which can vary by ±6% [130]. It should be noted that, as expected, for the weakly coupled resonators the loaded and unloaded Q-factors are within <1%. These values match the simulated predictions in Table 5 and demonstrate that the dielectric Q-factor limit of the resonator is being approached.

**Table 6 Measured Q-Factors**

| *Resonator* | *3 dB $Q_L$* | *Phase $Q_L$* | *3 dB $Q_0$* | *Phase $Q_0$* |
|---|---|---|---|---|
| Strong Offset | 5 220 | 5 600 | 10 050 | 10 200 |
| Strong Inline | 4 130 | 4 310 | 8 790 | 9 180 |
| Weak Offset | 7 090 | 8 720 | 7 140 | 8 780 |

### *4.6.3 Q-factor Uncertainty*

To understand the variation in the determination of Q-factor, the overall uncertainty in the measurement setup was evaluated. This was achieved through repeated measurement of the strongly-coupled inline PC resonator. The measurement process involved performing a TRL calibration of the VNA and then measuring the PC resonator DUT, this process is repeated six times to provide a statistically significant dataset, shown in Fig. 69. This data, along with information describing the performance of the measurement system is used to calculate the overall uncertainty in the measurements [131].

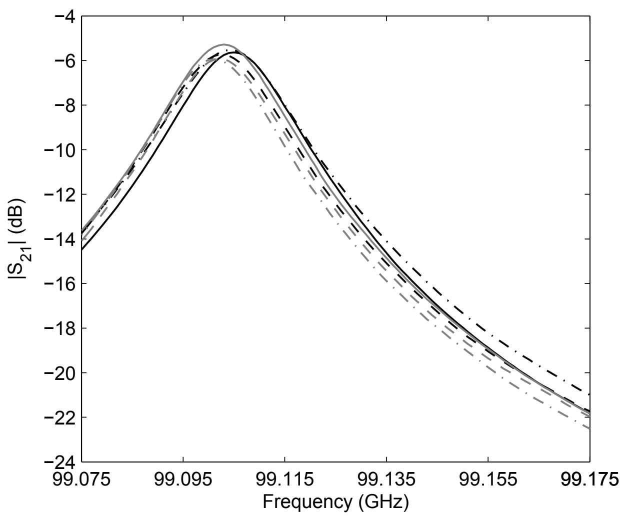


**Figure 69: Six repeated measurements of $|S_{21}|$ for the strongly coupled inline resonator.**

The overall uncertainty represents the uncertainty arising from random effects and from imperfect corrections due to systematic effects. The former is due to the repeatability of connections of the PC to the VNA test ports. It is evaluated by a statistical analysis of a series of observations, i.e. the repeated measurements shown in Fig. 69. This method of evaluating uncertainty is called a Type A evaluation of uncertainty [132]. The latter is due to the VNA linearity, isolation and mismatch between the test ports and the PC DUT. It is evaluated by means, other than a statistical analysis, of a series of observations. These (non-statistical) methods of evaluating uncertainty are called Type B [132]. Specifically, the linearity of the VNA is determined by measuring the transmission of a calibrated step attenuator, seen in Fig. 70, over a range of different attenuator settings. The VNA isolation is determined by observing the measured transmission when no physical connection is made between the test ports, i.e. they both have matched loads connected. Finally, the mismatch between the VNA and the PC resonator is determined from the measurements of the S-parameters of the PC DUT [131].

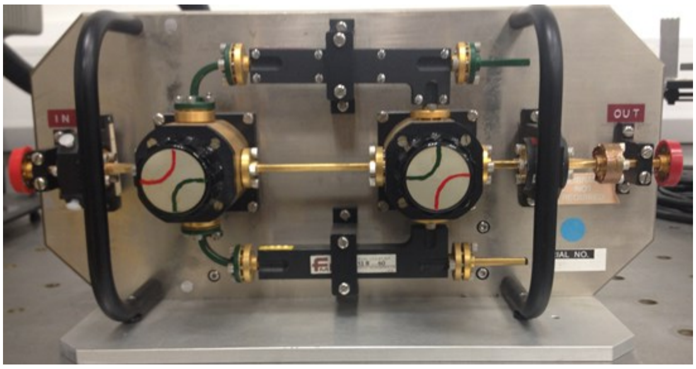


**Figure 70: Calibrated step attenuator**

The measurements were taken using the PIMMS software which calculates the expanded uncertainty $U$ and the corresponding coverage factor, $\varsigma$. From this data it is possible to decompose both Type A and Type B standard uncertainties using (37) – (40).

$$U = \varsigma u \tag{37}$$

$$u = \sqrt{u(a)^2 + u(b)^2} \tag{38}$$

$$a = \sqrt{\frac{\sum_{i=1}^{6} |S_i - \bar{S}|}{n(n-1)}} \tag{39}$$

$$\bar{S} = \frac{\sum_{i=1}^{6} S_i}{n} \tag{40}$$

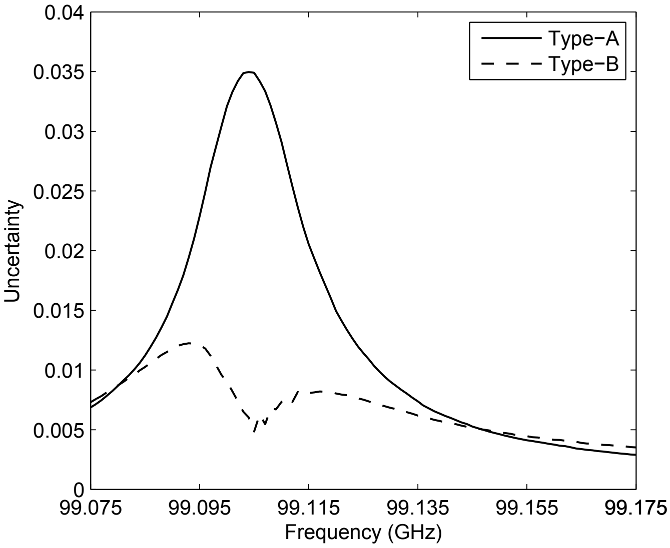


**Figure 71: Type A and Type B uncertainties**

Figure 71 shows the relative sizes for both Type A and combined Type B components of uncertainty, as a function of measurement frequency. This figure demonstrates that the Type A component of uncertainty dominates the overall uncertainty of the measurements, particularly in the region of the centre frequency, $f_0$. This, as previously mentioned, is due to the misalignment of the PC DUT within the WR-10 waveguide aperture. This component of uncertainty is considered to be representative of the mechanical and electromagnetic quality of the MPRWG-to-PC DUT interconnect, rather than the inherent quality of the PC resonator. For future applications, the focus is on the creation of monolithically integrated photonic crystal devices therefore, this type of interconnect will not be used as a result, it is appropriate to neglect the Type A uncertainty components, when evaluating the uncertainty in the Q-factor of just the PC resonator, and only consider the Type B components of uncertainty.

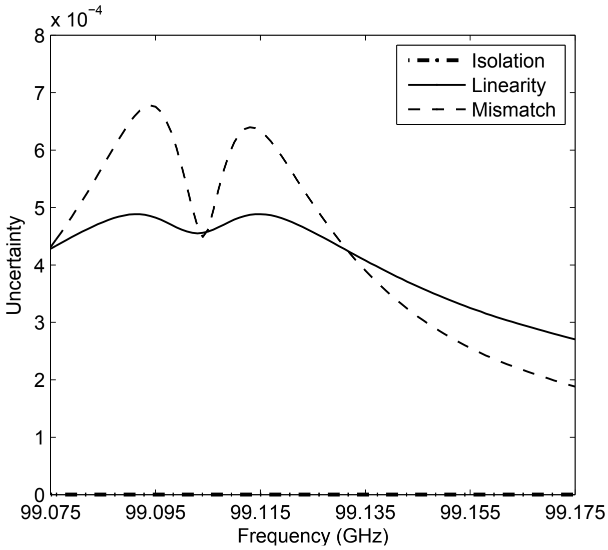


**Figure 72: Type B uncertainty components. The uncertainty in mismatch and linearity dominate while the isolation uncertainty is almost zero.**

Figure 72 shows the sizes of each of the three Type B uncertainty components – linearity, isolation and mismatch, as a function of frequency. It is seen that, for this measurement set-up, the contribution due to isolation is negligible, (compared with the uncertainty due to linearity and mismatch) and random effects are also considered negligible. This is due to significant transmission through the PC and so the detected signal level is well above the VNA noise floor. The contributions to uncertainty due to linearity and mismatch are combined to give the overall uncertainty in the S-parameter measurement results at each measurement frequency.

$$u(b) = \sqrt{u(L)^2 + u(I)^2 + u(M)^2 + u(R)^2} \tag{41}$$

### *Uncertainty Analysis for 3 dB Q-factor Determination*

The uncertainty in the S-parameter measurements is propagated to the uncertainty in Q-factor determination, using the following technique. Firstly, plots of $|S_{21}|$, in the vicinity of $f_0$ and $f_l$, are presented. These plots show (i) the mean value of $|S_{21}|$; (ii) the maximum value of $|S_{21}|$, where the maximum value is derived from the mean value plus its standard uncertainty [132]; and (iii) the minimum value of $|S_{21}|$, where the minimum value is derived from the mean value minus its standard uncertainty [132]. These plots are shown in Figs. 73 and 74 for $f_0$, and $f_l$ respectively, with $f_u$ calculated the same way as $f_l$ but from the upper 3 dB point.

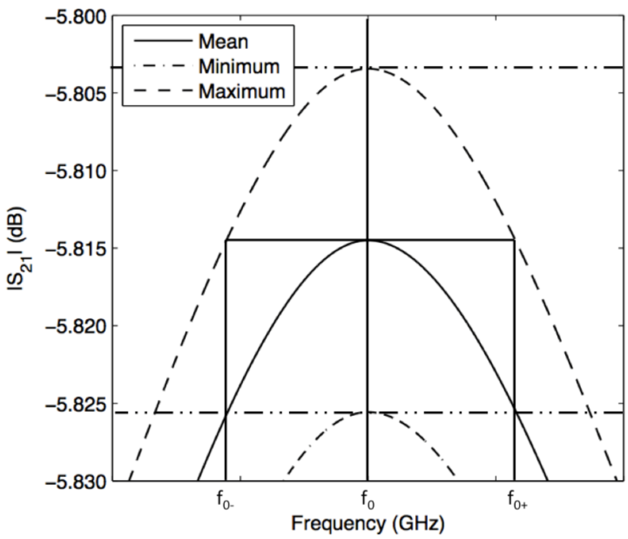


**Figure 73: Impact of uncertainty in $|S_{21}|$ on the determination of $f_0$ for the strongly-coupled inline PC resonator**

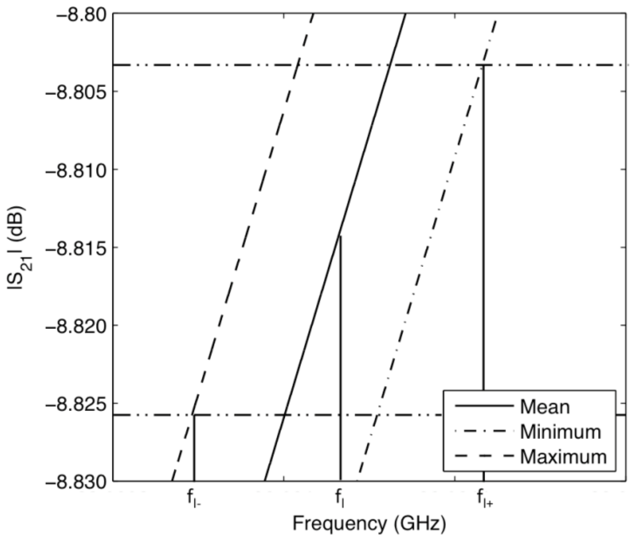


**Figure 74: Impact of uncertainty in $|S_{21}|$ on the determination of $f_l$ for the strongly-coupled inline PC resonator.**

Following the methods described in [132] the mean values and standard uncertainties in $f_0$, $f_l$ and $f_u$ are used in (42)-(45) to obtain the standard uncertainty in $Q_L$, $u(Q_L)$. This gives a value of $Q_L = 4{,}129 \pm 58$; which gives an uncertainty in $Q_L$ of 1.4%.

$$u(Q_L) = \sqrt{\left(\frac{\partial Q_L}{\partial f_0}\right)^2 u(f_0)^2 + \left(\frac{\partial Q_L}{\partial f_l}\right)^2 u(f_l)^2 + \left(\frac{\partial Q_L}{\partial f_u}\right)^2 u(f_u)^2} \tag{42}$$

$$\frac{\partial Q_L}{\partial f_0} = \frac{1}{f_u - f_l} \tag{43}$$

$$\frac{\partial Q_L}{\partial f_u} = \frac{-f_0}{(f_u - f_l)^2} \tag{44}$$

$$\frac{\partial Q_L}{\partial f_l} = \frac{f_0}{(f_u - f_l)^2} \tag{45}$$

The mean values and standard uncertainties for $Q_L$ and $|S_{21}|$ are then used in (46)-(48) to obtain the standard uncertainty in $Q_0$, $u(Q_0)$.

$$u(Q_0) = \sqrt{\left(\frac{\partial Q_0}{\partial Q_L}\right)^2 u(Q_L)^2 + \left(\frac{\partial Q_0}{\partial |S_{21}|}\right)^2 u(|S_{21}|)^2} \tag{46}$$

$$\frac{\partial Q_0}{\partial Q_L} = \frac{1}{1 - |S_{21}|} \tag{47}$$

$$\frac{\partial Q_0}{\partial |S_{21}|} = \frac{Q_L}{(1 - |S_{21}|)^2} \tag{48}$$

This gives a value of $Q_0 = 8{,}460 \pm 120$; which gives an uncertainty in $Q_0$ of 1.4%

### *Uncertainty Analysis for Phase Q-factor Determination*

A second method of propagating the uncertainty in the S-parameter measurements is considered, where the Q-factor is determined using the phase of $S_{21}$, as described by (35). The maximum and minimum values of $\omega_0$ are found using the same method as described using Fig. 73 (with the value of $f_0$ found by converting to angular frequency $\omega_0$). Uncertainty in the phase gradient is determined by plotting the mean, maximum and minimum values of $\angle S_{21}$, as shown in Fig. 20. These minimum and maximum curves are found by taking the mean and then adding or subtracting the standard uncertainty in the measurement of the phase. To establish the uncertainty in the phase gradient, three gradients are taken, using a finite difference method: (i) from the mean value curve at $f_{0-}$, and $f_{0+}$; (ii) the maximum curve at $f_{0-}$ and minimum curve at $f_{0+}$; and (iii) the minimum curve at $f_{0-}$ and maximum curve at $f_{0+}$, where $f_{0-}$, and $f_{0+}$ are the measured values either side of the peak $f_0$.

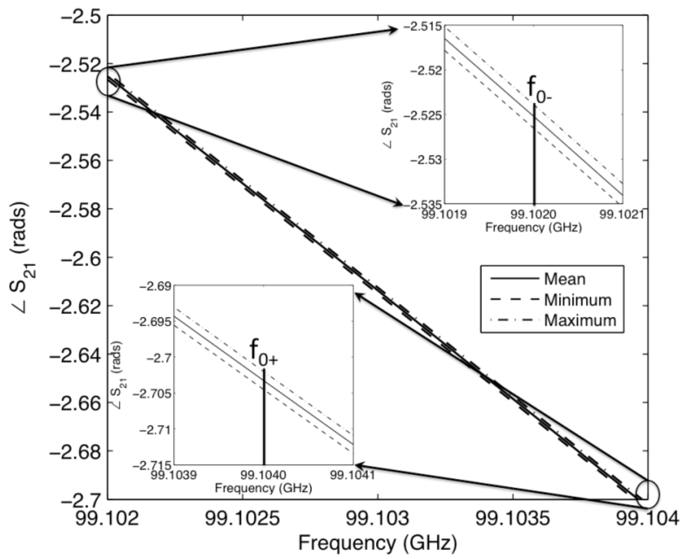


**Figure 75: Impact of uncertainty in ∠S 21 on the determination on $\left|\frac{\delta\angle S_{21}}{\delta\omega}\right|$ from $f_{0+}$ and $f_0$ for the strongly-coupled inline PC resonator.**

These values are then applied to (35), to find the mean $Q_L$ from the mean values of $\omega_0$ and $\left|\frac{\delta\angle S_{21}}{\delta\omega}\right|$. The standard uncertainty in $Q_L$, due to $\omega_0, u(Q_{L\omega_0})$, is calculated using the maximum and minimum of $\omega_0$, whilst keeping $\left|\frac{\delta\angle S_{21}}{\delta\omega}\right|$ at its mean value, giving $u(Q_{L\omega_0})$ = ± 37. The same method is employed to calculate the standard uncertainty in $Q_L$ due to $\left|\frac{\delta\angle S_{21}}{\delta\omega}\right|, u(Q_{L\angle})$, keeping $\omega_0$ constant at its mean value and then applying the maximum and minimum values for $\left|\frac{\delta\angle S_{21}}{\delta\omega}\right|$. This gives $u(Q_{L\angle})$ = ± 63.

Finally, (49) is used to obtain $u(Q_L)$ = ± 72, thus, giving $Q_L$ = 4,412 ± 72.

$$u(Q_L) = \sqrt{u(Q_{L\omega_0})^2 + u(Q_{L\angle})^2} \tag{49}$$

To obtain $Q_0$ and $u(Q_0)$ the same method, as used previously in (46)-(48), is used to give $Q_0$ = 9,040 ± 150; this gives an uncertainty in $Q_L$ of 1.6% and 1.7% in $Q_0$. As with all the calculated Q-factors presented, the deviation from the numbers given in Tables 5 and 6 may be slightly larger than the uncertainties calculated. This is due to Type A uncertainties being disregarded, as it quantifies alignment limitations in our experimental setup and not the underlying performance of the PC resonators.

## 4.7 Future Work

The photonic crystal work described in this chapter shows state-of-the-art performance. However, all the devices are modular and interface with MPRWG. To take this work further, firstly the different components: waveguides, switches, attenuators and resonators must be integrated onto a single substrate.

### *4.7.1 Monolithic Integration*

The next design step for this technology is for monolithic integration of the photonic crystal and electronics onto a single silicon substrate. To achieve this a new transition needs to be designed from the photonic crystal W1 defect waveguide to slot line or microstrip. This is not a trivial transition to design, as initial investigations showed that creating the transition on the surface of the silicon would lead to a lot of radiation into free space, rather than the silicon substrate. A proposed concept is shown in Fig. 76. The transition is from slotline to the W1-defect mode using a tapered Vivaldi shaped transition. This transition is located at half the depth of the waveguide and would be coated with a dielectric, with similar properties to the silicon substrate so that a symmetrical field is created. This transition could be fabricated by DRIE of the silicon to thin the substrate then sputter coating and patterning of the metal, followed by spin coating of the dielectric onto the transition.

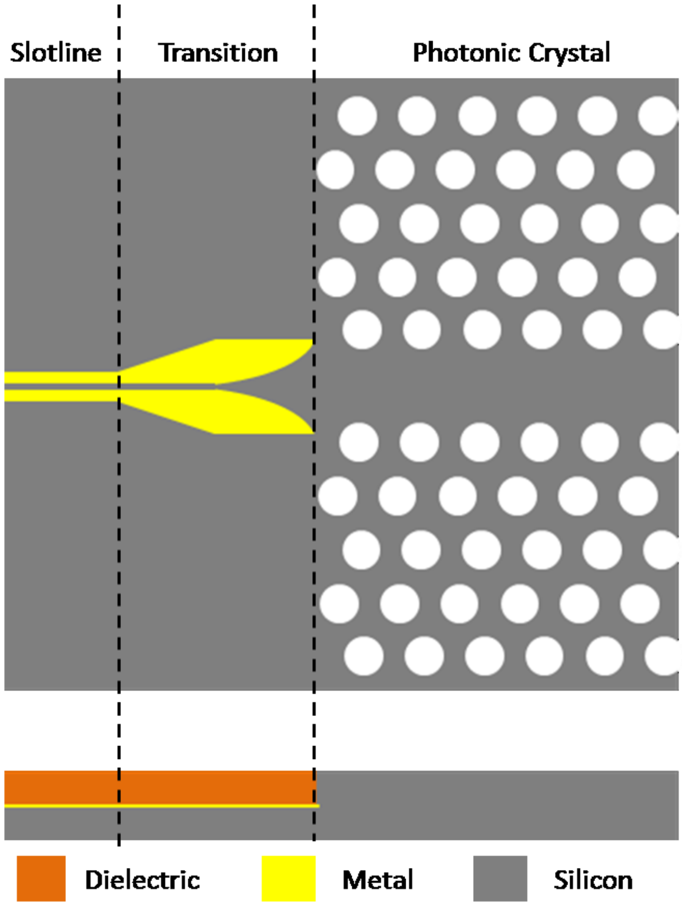


**Figure 76: Conceptual idea for a slot line to PC W1 waveguide defect transition**

### *4.7.2 Liquid Sensing*

High Q-factor resonators have been shown to be ideal tools for liquid sensing. A proof of principle experiment was undertaken to demonstrate the concept. A 280/300 μm inner/outer diameter quartz capillary tube was inserted through a hole, adjacent to the resonant cavity. Various solutions of water and ethanol were pumped through the capillary tube. This experimental setup is shown in Fig 77. The S-parameters were then measured for each solution and also the empty capillary tube as a reference.

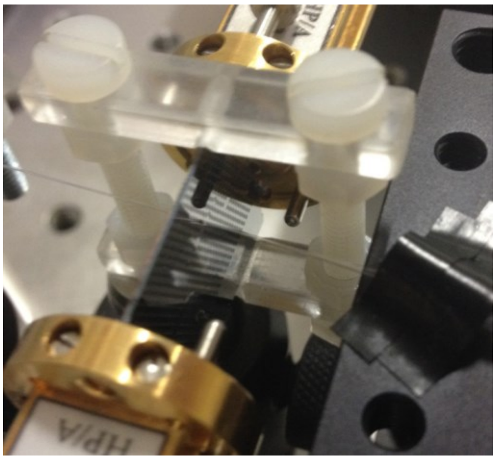

**Figure 77: Measurement setup for microfluidic experiment**

Figure 78 shows the transmission resonance changes for different concentrations of ethanol/water solutions. As the water content increases there is a downwards frequency shift, due to the increase in $\varepsilon_r'$ and decrease in Q-factor due to an increase $\varepsilon_r''$. It is estimated that the interaction volume is 40 nl and shows potential for future application is liquid detection and biosensing.

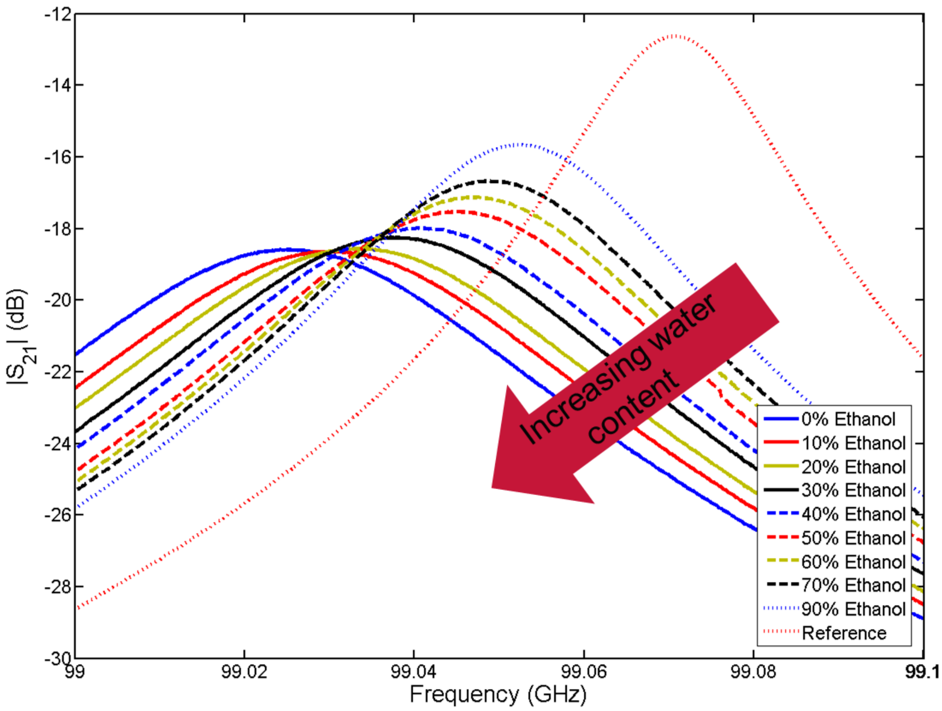


**Figure 78: Measured $|S_{21}|$ for different ethanol/water mixture concentrations**

### 4.7.3 Optoelectronic Devices

The optoelectronic devices demonstrated shows the potential for the photonic crystal switch and attenuator. Further work to complete the current work requires an investigation into the laser beam profile, how the spot size and single-sided laser illumination affects the attenuator and switch performance. A second experiment will also take place to look at how the resonator detunes when it is illuminated, creating the possibility of tuneable filters.

To profile the laser beam, a pinhole aperture will be scanned across it in 2 dimensions. Measuring the power across the beam enables its shape to be accurately modelled, as it has previously been assumed to provide a top hat profile, rather than Gaussian, in current simulations. A study of the effect of the spot size can be undertaken via two methods. Firstly, the focus of the optics associated with the laser can be modified to reduce or increase the size of the laser spot. Alternatively an iris aperture could be used to vary the spot size.

### 4.7.4 Higher Frequency Devices

All the devices currently operate at ca. 100 GHz, the lower end of the THz frequency range as the material losses were most significant at this frequency (as shown in Fig. 40). The fabrication of devices working at higher frequency will demonstrate how the device losses change with frequency. The expectation is that the resonators appear to be limited by the dielectric losses, so higher Q-factors should be achieved. Moving to higher frequency will mean a scaling down in size of all dimensions, a thinner substrate and smaller width of the W1 defect waveguide. This will mean that a lower power laser with a smaller spot size is required for switches.

### *4.7.5 Filter Banks*

The realisation of single frequency filters has been demonstrated through the resonator technology. It can be shown that by changing the method of coupling, to the resonant cavity, that bandreject as well as bandpass filters can be created. Moreover, it possibility to include multiple resonant cavities on a single PC as illustrated in Fig. 79 for: (a) bandpass and (b) bandreject filters. This architecture makes it possible to create multiplexer and demultiplexers, illustrated in Fig. 79 (c). Multi-frequency microfluidics is another application, where a channel is etched in the silicon passes through each cavity.

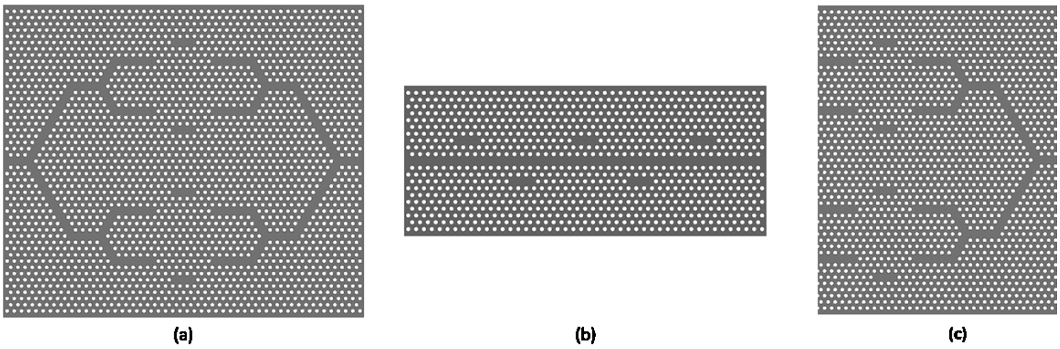


**Figure 79: Photonic crystal filter banks; (a) bandpass and (b) bandreject; and (c) multiplexer**

# 5 Conclusion and Further Work

Within this thesis several unique sensing structures have been shown, surface plasmonics, metal mesh filters and photonic crystals. They all have their own unique properties that make them ideal for different applications, however they all represent immature technologies.

This work has demonstrated that researchers need to be careful in using commercial solvers, as it is not always obvious which material models are being applied as laid out in Chapter 1 and if the correct modes are being excited as demonstrated with the spoof plasmonic structure in Chapter 2. Chapter 2 also discusses semiconductor plasmonics where doped silicon wafers can be used directly for THz sensing. Calculations and simulations show promising results for future sensing applications.

Chapter 3 describes metal mesh filters and how with careful design pass band filters can be created with extremely good out of band rejection is achieve using electrically thick substrates that are lower cost and more durable than the current electrically thin substrates, although, with a small trade off in pass band filters. A novel metal mesh filter stress sensor has been simulated and shows that small compressions of the device can be measured. It has the potential to be a ubiquitous THz device as it can be mass produced or even embedded within building materials (such as plaster, carbon fibre etc) to monitor determination over time e.g. a wall before and after earthquakes.

Chapter 4 shows the real promise of photonic crystal technology that has state-of-the-art performance. Several building block components for a future THz photonic crystal architecture have been experimentally tested: resonators were measured and the associated measurements uncertainties rigorously analysed giving unloaded Q-factors of 9,040 ± 150 at ~100 GHz, attenuators that have >40 dB of attenuation across the band of operation and up to 60 dB of attenuation with no moving parts and initial results for use of the photonic crystal as a liquid sensor.

## 5.1 Further Work

Beyond these research highlights that have already been undertaken there are many ways in which the research within this thesis can be continued.

### 5.1.1 Surface Wave Filters

Within 2.3, theoretical work and simulations demonstrate coupling of a surface plasmon mode on a silicon dielectric interface at THz frequencies. The logical progression of this work is experimental verification of these results, where n-Type and p-Type silicon wafers of the same resistivity have different dispersion curves verify Fig. 17. This would be done through a similar setup employed with Comsol simulations

Beyond this, there are a wide variety of sensors already available using surface plasmon modes in the optical range. These sensor are all constrained by the conductivity of the metal, which is not easy to modify. Therefore, to interrogate a different frequency, the angle of the light incident on the base of the prism has to change, to get a different k-vector. However, at THz the conductive substrate is a semiconductor. It is well understood that the local conductivity of a semiconductor can be modified by biasing or illumination. By undertaking such a process, it will be possible to sweep the frequency as the change in conductivity causes a shift in the dispersion diagram; changing the frequency that is coupled to the surface plasmon mode. This was seen by looking at different wafers.

#### *Electrostatic Sensor*

The first method of locally modifying the conductivity of the silicon is to electrically bias the silicon. This has already been shown in many electronic devices and the simplest structure is the MOS capacitor. Figure 23 shows a concept device that has two top contacts and a bottom contact. By biasing the contacts, an electrostatic field will be generated. This will cause a movement of the free charges within the silicon which will oppose the field created. Using [82] to calculate the depth need to completely screen the field versus the silicon wafer resistivity, as shown in Fig. 24, it shows that this is a possible method to shift the frequency. For this sensor, a coupling grating would be integrated to couple to the surface plasmon mode, as seen in Fig. 18.

#### *Photoconductive Sensor*

The second method to locally modify the conductivity of the silicon is to illuminate it with an electromagnetic wave, as silicon is a photoconductive material. This means that illuminating an area of silicon with an electromagnetic wave that has an energy greater than the silicon’s bandgap energy will generate electron-hole pairs in the silicon, which will locally increase the conductivity. A conceptual diagram of such a sensor is shown in Fig. 25. A prism is used to couple to the surface plasmon mode, using the Otto coupling method. A laser beam incident from the side illuminates a spot under the prism, where the surface plasmon mode will couple. This sensor has the potential to become a ubiquitous THz sensor, in applications such as bio-sensing where disposable sensors are needed to avoid cross contamination; one only has to replace the silicon substrate, as everything else is isolated from the sample.

### 5.1.2 Metal Mesh Filters

The results shown in this chapter 3 show that a small decrease in the performance of the filter can be traded for a simpler manufacturing method and an increase in the mechanical strength of the filters. This makes them ideal for ubiquitous applications.

A stress sensors has been explored theoretically and requires experimental verification. This will lead to measurement of a prototype device. It is expected that, due to the complimentary nature of the metal mesh filters, the sensor will work in reflection mode as well as transmission, leading to a wide variety of applications. For example the small sensor is embedded within a surface and then a handheld scanner is passed over the surface to map the stress in the surface (e.g. in walls before and after earthquakes).

### 5.1.3 Photonic Crystals

The photonic crystal work described in chapter 4 shows state-of-the-art performance. However, all the devices are modular and interface with MPRWG. To take this work further, firstly the different components: waveguides, switches, attenuators and resonators must be integrated onto a single substrate.

#### *Monolithic Integration*

The next design step for this technology is for monolithic integration of the photonic crystal and electronics onto a single silicon substrate. To achieve this a new transition needs to be designed from the photonic crystal W1 defect waveguide to slot line or microstrip. This is not a trivial transition to design, as initial investigations showed that creating the transition on the surface of the silicon would lead to a lot of radiation into free space, rather than the silicon substrate. A proposed concept is shown in Fig. 76. The transition is from slotline to the W1-defect mode using a tapered Vivaldi shaped transition. This transition is located at half the depth of the waveguide and would be coated with a dielectric, with similar properties to the silicon substrate so that a symmetrical field is created. This transition could be fabricated by DRIE of the silicon to thin the substrate then sputter coating and patterning of the metal, followed by spin coating of the dielectric onto the transition.

#### *Liquid Sensing*

High Q-factor resonators have been shown to be ideal tools for liquid sensing. A proof of principle experiment was undertaken to demonstrate the concept. A 280/300 µm inner/outer diameter quartz capillary tube was inserted through a hole, adjacent to the resonant cavity. Various solutions of water and ethanol were pumped through the capillary tube. This experimental setup is shown in Fig 77. The S-parameters were then measured for each solution and also the empty capillary tube as a reference.

Figure 78 shows the transmission resonance changes for different concentrations of ethanol/water solutions. As the water content increases there is a downwards frequency shift, due to the increase in $\varepsilon_r'$ and decrease in Q-factor due to an increase $\varepsilon_r''$. It is estimated that the interaction volume is 40 nl and shows potential for future application is liquid detection and biosensing.

### *Optoelectronic Devices*

The optoelectronic devices demonstrated shows the potential for the photonic crystal switch and attenuator. Further work to complete the current work requires an investigation into the laser beam profile, how the spot size and single-sided laser illumination affects the attenuator and switch performance. A second experiment will also take place to look at how the resonator detunes when it is illuminated, creating the possibility of tuneable filters.

To profile the laser beam, a pinhole aperture will be scanned across it in 2 dimensions. Measuring the power across the beam enables its shape to be accurately modelled, as it has previously been assumed to provide a top hat profile, rather than Gaussian, in current simulations. A study of the effect of the spot size can be undertaken via two methods. Firstly, the focus of the optics associated with the laser can be modified to reduce or increase the size of the laser spot. Alternatively an iris aperture could be used to vary the spot size.

### *Higher Frequency Devices*

All the devices currently operate at ca. 100 GHz, the lower end of the THz frequency range as the material losses were most significant at this frequency (as shown in Fig. 40).

The fabrication of devices working at higher frequency will demonstrate how the device losses change with frequency. The expectation is that the resonators appear to be limited by the dielectric losses, so higher Q-factors should be achieved. Moving to higher frequency will mean a scaling down in size of all dimensions, a thinner substrate and smaller width of the W1 defect waveguide. This will mean that a lower power laser with a smaller spot size is required for switches.

### *Filter Banks*

The realisation of single frequency filters has been demonstrated through the resonator technology. It can be shown that by changing the method of coupling, to the resonant cavity, that bandreject as well as bandpass filters can be created. Moreover, it possibility to include multiple resonant cavities on a single PC as illustrated in Fig. 79 for: (a) bandpass and (b) bandreject filters. This architecture makes it possible to create multiplexer and demultiplexers, illustrated in Fig. 79 (c). Multi-frequency microfluidics is another application, where a channel is etched in the silicon passes through each cavity.

# List of Publications from this PhD

## Journals

1. W. J. Otter, S. M. Hanham, N. M. Ridler, G. Marino, N. Klein, and S. Lucyszyn, "100 GHz ultra-high Q-factor photonic crystal resonators", *Sensors and Actuators A Physical*, vol. 217, pp. 151-159, Sep. 2014.
2. E. Episkopou, S. Papantonis, W. J. Otter and S. Lucyszyn; "Defining Material Parameters in Commercial EM Solvers for Arbitrary Metal-Based THz Structures", *Terahertz Science and Technology, IEEE Transactions on*, vol.2, no.5, pp.513-524, Sep. 2012.

## International Conferences

1. N. Klein, S. Hanham, T. H. Basey-Fisher, C. Watts, O. Shaforost , W. J. Otter, S. Lucyszyn, "Micro- and Millimetre Wave Measurements of Nanolitre Biological Liquids by Dielectric Resonators", *IMWS-Bio 2014*, London, UK, Dec. 2014.
2. W. J. Otter, F. Hu, S. Lucyszyn and M. A. Ribeiro, "Prototype Design of THz Metallic Mesh Stress Sensor" *MPNS COST Action MP1204 STSM Workshop*, Warsaw, Poland, Nov. 2014.
3. W. J. Otter, F. Hu, J. Hazell and S. Lucyszyn, "THz Metal Mesh Filters On Electrically Thick Fused Sillica Substrates", *39th International Conference on Infrared, Millimeter, and Terahertz Waves (IRMMW-THz 2014)*, Tucson, USA, Sep. 2014.
4. W. J. Otter, S. M. Hanham, N. Klein, S. Lucyszyn and A. S. Holmes, "W-band Laser-controlled Photonic Crystal Variable Attenuator", *IEEE International Microwave Symposium (IMS2014)*, Tampa Bay, USA, Jun. 2014.

5. W. J. Otter, F. Hu, and S. Lucyszyn, “Scalable Metal Mesh Filters for Low Cost THz applications”, *International Conference on Semiconductor Mid-IR Materials and Optics (SMMO2014)*, Marburg, Germany, Feb. 2014.
6. S. Lucyszyn, F. Hu and W. J. Otter, “Technology Demonstrators for Low Cost Terahertz Engineering”, *Asia Pacific Microwave Conference 2013 (APMC 2013)*, Seoul, South Korea, pp. 518-520, Nov. 2013 (Invited).
7. W. J. Otter, S. M. Hanham, N. Ridler, A. S. Holmes, N. Klein and S. Lucyszyn, “Sub-THz Photonic Crystal Devices”, *International Conference on THz and Mid Infrared Radiation and Applications to Cancer Detection using Laser Imaging*, Sheffield, UK, Oct. 2013.
8. F. Hu, W. J. Otter and S. Lucyszyn, “THz Metal Mesh Filters on Thick Fused Silica Substrate”, *International Conference on THz and Mid Infrared Radiation and Applications to Cancer Detection using Laser Imaging,* Sheffield, UK, Oct. 2013.
9. W. J. Otter, S. M. Hanham, E. Episkopou, Y. Zhou, N. Klein, A. S. Holmes and S. Lucyszyn, “Photoconductive Photonic Crystal Switch”, *38th International Conference on Infrared, Millimeter, and Terahertz Waves (IRMMW-THz 2013)*, Mainz, Germany, Sep. 2013.
10. N. Klein, O. Shaforost, K. Wang, G. Zhexi, M. Adabi, S. M. Hanham, P. K. Petrov, W. J. Otter, M. Navarro-Cia, S. Lucyszyn and L. Hao, “Microwave-to-Terahertz Investigation of CVD Graphene: Towards Sensor and Communication Applications” *39th International Conference on Micro and Nano Engineering (MNE 2013)*, London, UK, pp. 223, Sep. 2013.
11. N. Klein, T. H. Basey-Fisher, W. J. Otter, N. Guerra, C. Triulzi, A. Gregory, S. M. Hanham and S. Lucyszyn, “Towards Microwave and Millimeter Wave Biosensors” *Physics and Engineering of Microwaves, Millimeter and Submillimeter Waves (MSMW ‘13),* 2013 International Kharkov Symposium on, Kharkov, Ukraine, pp. 510-511, Jun. 2013.

12. W. J. Otter, S. M. Hanham, N. Klein and S. Lucyszyn, “Photonic Crystal Band Reject and Band Pass Filters”, *MPNS COST Action Training School – MP1204*, Cortona, Italy, May 2013.
13. E. Episkopou, S. Papantonis, W. J. Otter and S. Lucyszyn, “Material Parameters in Commercial EM Solvers for Arbitrary Metal-Based THz Structures”, *MPNS COST Action Training School – MP1204*, Cortona, Italy, May 2013.
14. E. Episkopou, S. Papantonis, W. J. Otter and S. Lucyszyn, “Demystifying Material Parameters for THz Electromagnetic Simulations”, *4th UK/EU-China Workshop on Millimetre Wave and Terahertz Technology*, Glasgow, UK, pp. 80-81, Sep. 2011.

## National Conferences

1. W. J. Otter, F. Hu, J. Hazell and S. Lucyszyn; “From mm-wave to THz: Scalable Filter Design for Ultra-low Cost Applications”, *ARMMS RF & Microwave Society Conference*, Nr Thame, Apr. 2014.
2. W. J. Otter, S. M. Hanham, N. M. Ridler, A. S. Holmes, N. Klein and S. Lucyszyn, “mm-Wave Photonic Crystal Technology”, *IET Colloquium on Millimetre-wave and Terahertz Engineering & Technology,* Liverpool, Mar. 2014.
3. W. J. Otter, S. M. Hanham, N. M. Ridler, A. S. Holmes, N. Klein and S. Lucyszyn, “100 GHz Photonic Crystal Devices”, *ARMMS RF & Microwave Society Conference*, Wyboston, Nov. 2013. (Runner-Up Prize)

# List of References


[1] D. D. Arnone, C. M. Ciesla, A. Corchia, S. Egusa, M. Pepper, J. M. Chamberlain, C. Bezant, E. H. Linfield, R. Clothier, and N. Khammo, "Applications of terahertz (THz) technology to medical imaging," *Proc. SPIE Terahertz Spectroscopy and Applications II*, vol. 3828, no. 1, pp. 209-219, Jun. 1999.

[2] http://www.rpi.edu/terahertz/about_us.html

[3] B. Ferguson, and X. C. Zhang, "Materials for terahertz science and technology," *Nature Mat.*, vol. 1, no. 1, pp. 26-33, Sep. 2002.

[4] K. Kawase, Y. Ogawa, Y. Watanabe, and H. Inoue, "Nondestructive terahertz imaging of illicit drugs using spectral fingerprints," *Opt. Express*, vol. 11, no. 20, pp. 2549-2554, Oct. 2003.

[5] http://www.teraview.com/products/thz-reflectometry/faultanalysis.html

[6] F. Rutz, M. Koch, S. Khare, M. Moneke, H. Richter, and U. Ewert,"Terahertz quality control of polymeric products," *Int. J. Infrared and Milli.*, vol. 278, no. 4, pp. 547-556, Apr. 2000.

[7] Z Yan, Y. Ying, H. Zhang, and H. Yu, "Research progress of terahertz wave technology in food inspection," *Proc. SPIE*. vol. 6373, Oct. 2006.

[8] K. Fukunaga, I. Hosako, Y. Kohdzuma, T. Koezuka, M.-J. Kim, T. Ikari, and X. Du, "Terahertz analysis of an East Asian historical mural painting," *J. Eur. Opt. Soc, Rapid Publ.,* vol. 5, May 2010.

[9] P. H. Siegel, "THz instruments for space," *IEEE Trans. Antennas Propag.*, vol. 55, no 11, pp. 2957-2965, Nov. 2007.

[10] http://www.teraview.com/applications/homeland-security-defense-industry/explosive-detection.html

[11] Z. Li, K. Wu, "24-GHz Frequency-Modulation Continuous-Wave Radar Front-End System-on-Substrate," *IEEE Trans. Microw. Theory Tech.*, vol. 56, no. 2, pp.278-285, Feb. 2008.

[12] K. K. Samanta, D. Stephens, I. D. Robertson, "Design and performance of a 60-GHz multi-chip module receiver employing substrate integrated waveguides," *IET Microw. Ant. & Prop.,* vol. 1, no. 5, pp.961-967, Oct. 2007.

[13] http://www.aoquntech.com/en/product_info.aspx?id=4

[14] J. Wiltse, "History of millimeter and submillimeter waves," *IEEE Trans. Microw. Theory Tech.*, vol. 32, no. 9, pp. 1118–1127, Sep. 1984.

[15] http://invaderxan.pbworks.com/f/1193264846/atmospheric-opacity.jpg

[16] G. Chattopadhyay "Technology, Capabilities, and Performance of Low Power Terahertz Sources," *IEEE Trans. Terahertz Sci. & Technol.,* vol. 1, no. 1, pp.33-53, Sep. 2011.

[17] E. Seok, D. Shim, C. Mao, R. Han, S.Sankaran, C. Cao, W. Knap, and K. O. Kenneth, "Progress and challenges towards terahertz CMOS integrated circuits," *IEEE J. Solid-State Circuits,* vol. 45, no. 8, pp. 1554-1564, Aug. 2010.

[18] H. Eisele, "480 GHz oscillator with an InP Gunn device," *Electron. Lett.*, vol. 46, no. 6, pp. 422-423, Mar. 2010.

[19] V. Radisic, K. M. K. H. Leong, X. B. Mei, S. Sarkozy, W. Yoshida, W. R. Deal, "Power Amplification at 0.65 THz Using InP HEMTs," *IEEE Trans. Microw. Theory & Tech.,* vol. 60, no. 3, pp. 724-729, Mar. 2012.

[20] R. Han, and E. Afshari, "A high-power broadband passive terahertz frequency doubler in CMOS*," IEEE Trans. Microw. Theory & Tech.*, vol. 61, no. 3, pp. 1150-1160, Mar. 2013.

[21] S. Preu, G. H. Döhler, S. Malzer, L. J. Wang, and A. C. Gossard, "Tunable, continuous-wave Terahertz photomixer sources and applications," *J. of Appl. Phys*., vol. 109, no. 6, May 2011.

[22] H.-J. Song, K. Ajito, Y. Muramoto, A. Wakatsuki, T. Nagatsuma, and N. Kukutsu, “Uni-travelling-carrier photo-diode module generating 300 GHz power greater than 1 mW,” *IEEE Microw. Compon. Lett.*, vol. 22, no. 7, pp. 363-365, Jul. 2012.

[23] I. S. Gregory, C. Baker, W. R. Tribe, I. V. Bradley, M. J. Evans, E. H. Linfield, G. Davies, and M. Missous, “Optimization of photomixers and antennas for continuous-wave terahertz emission,” *IEEE J. Quantum Electron.*, vol. 41, no. 5, pp. 717-728, May 2005.

[24] J. Shikata, K. Kawase, K. Karino, T. Taniuchi, and H. Ito, “Tunable terahertz-wave parametric oscillators using LiNbO3 and MgO:LiNbO3 crystals,” *IEEE Trans. Microw. Theory & Tech.*, vol. 48, no. 4, pp. 653-661, Apr. 2000.

[25] R. Köhler, A. Tredicucci, F. Beltram, H. E. Beere, E. H. Linfield, A. G. Davies, D. A. Ritchie, R. Iotti, and F. Rossi, “Terahertz semiconductor-heterostructure laser,” *Nature*, vol. 417, pp. 156-159, May 2002.

[26] B. S. Williams, “Terahertz quantum-cascade lasers,” *Nature Photon.*, vol. 1, no. 9, pp. 517-525, Sept. 2007.

[27] S. Fathololoumi, E. Dupont, C. W. I. Chan, Z. R. Wasilewski, S. R. Laframboise, D. Ban, A. Mátyás, C. Jirauschek, Q. Hu, and H. C. Liu, “Terahertz quantum cascade lasers operating up to ∼200 K with optimized oscillator strength and improved injection tunneling,” *Opt. Express*, vol. 20, no. 4, pp. 3866-3876, Feb. 2012.

[28] W. Knap, V. Kachorovskii, Y. Deng, S. Rumyantsev, J. Lü, R. Gaska, M. Shur, G. Simin, X. Hu, M. Asif Khan, C. Saylor and L. C. Brunel, “Nonresonant detection of terahertz radiation in field effect transistors,” *J. of Appl. Phys.*, vol. 91, no. 11, pp. 9346-9353, Jun. 2002.

[29] F. Schuster, H. Videlier, A. Dupret, D. Coquillat, M. Sakowicz, J. Rostaing, M. Tchagaspanian, B. Giffard, and W. Knap, “A broadband THz imager in a low-

cost CMOS technology," *2011 Dig. Tech. Pap. IEEE Int. Solid State Circuits Conf. (ISSCC)*, pp. 42-43, Feb. 2011.

[30] S. Komiyama, O. Astafiev, V. Antonov, T. Kutsuwa, and H. Hirai, "A single-photon detector in the far-infrared range," *Nature*, vol. 403, pp. 405-407, Jan. 2000.

[31] Shu, C. Qiu, V. Astley, D. Nickel, D. M. Mittleman, and Q. Xu, "High-contrast terahertz modulator based on extraordinary transmission through a ring aperture," *Opt. Express*, vol. 19, no. 27, pp. 26666-26671, Dec. 2011.

[32] H. T. Chen, W. J. Padilla, M. J. Cich, A. K. Azad, R. D. Averitt and A. J. Taylor, "A metamaterial solid-state terahertz phase modulator," Na*ture Photon*., vol. 3, no. 3, pp. 148-151, Aug. 2009.

[33] W. L. Chan, H. T. Chen, A. J. Taylor, I. Brener, M. J. Cich, and D. M. Mittleman, "A spatial light modulator for terahertz beams," *Appl. Phys. Lett.,* vol. 94, no. 21, pp. 213511-1-213511-3, May 2009.

[34] D. Wu, N. Fang, C. Sun, X. Zhang, W. J. Padilla, D. N. Basov, D. R. Smith, and S. Schultz, "Terahertz plasmonic high pass filter," *Appl. Phys. Lett*., vol. 83, no. 1, pp. 201-203, Jul. 2003.

[35] O. Paul, R. Beigang, and M. Rahm, "Highly selective terahertz bandpass filters based on trapped mode excitation," *Opt. Express*, vol. 17, no. 21, pp. 18590-18595, Oct. 2009.

[36] J. F. O'Hara, R. Singh, I. Brener, E. Smirnova, J. Han, A. J. Taylor, and W. Zhang, "Thin-film sensing with planar terahertz metamaterials: sensitivity and limitations," *Opt. Express*, vol. 16, no. 3, pp. 1786-1795, Feb. 2008.

[37] http://www.teraview.com/

[38] Rohde & Schwarz Product Brochure 06.02 "R&S®ZVA-Zxx Millimeter-Wave Converters Network analysis up to 500 GHz" http://cdn.rohde-

schwarz.com/pws/dl_downloads/dl_common_library/dl_brochures_and_datasheets/pdf_1/ZVA-Zxx_bro_en_5214-2033-12_v0602.pdf

[39] Virginia Diodes Inc. Product Brochure “Vector Network Analyzer Extension Modules” http://vadiodes.com/images/Products/VNA/vnabrochure201408.pdf

[40] QMC Insturments http://www.terahertz.co.uk/

[41] M. Hamdi, F. Garet, L. Duvillaret, P. Martinez, G. Eymin-Petot-Tourtollet, “New approach for chipless and low cost identification tag in the THz frequency domain,” *2012 IEEE Int. Conf. on RFID-Technologies and Applications (RFID-TA),* pp. 24-28, Nov. 2012.

[42] http://dl.z-thz.com/brochures/micro-Z.pdf

[43] H. Sherry, J. Grzyb, Y. Zhao, R. Al Hadi, A. Cathelin, A. Kaiser, and U. Pfeiffer, “A 1kpixel CMOS camera chip for 25fps real-time terahertz imaging applications,” *2011 Dig. Tech. Pap. IEEE Int. Solid State Circuits Conf. (ISSCC)*, pp. 252-254, Feb. 2011.

[44] C. P. Smyth, " Dielectric behavior and structure: dielectric constant and loss, dipole moment, and molecular structure ", 1st Edition, McGraw-Hill, 1955.

[45] F. A Grant, "Use of complex conductivity in the representation of dielectric phenomena", *Journal of Applied Physics* vol. 29, no. 1, pp. 76-80, Jan. 1958.

[46] K. L. Ngai and R. W. Rendell, "Interpreting the real part of the dielectric permittivity contributed by mobile ions in ionically conducting materials", *Physics Review B,* vol. 61 no. 14, Apr. 2000.

[47] T. W. Kim, W. P. Beyermann, D. Reagor and G. Gruner, "Complex conductivity measurements at several frequencies in the millimetre wave spectral range", *Rev. Sci. Instrum.,* vol. 59, no. 7, Jul. 1988.

[48] U. Kaatze, "Complex permittivity of water as a function of frequency and temperature", *Journal of Chemical & Engineering Data*, vol. 34, no. 4, pp. 371-374, Oct. 1989.

[49] Y. Zhou and S. Lucyszyn, "HFSS$^{TM}$ modelling anomalies with THz metal-pipe rectangular waveguide structures at room temperature", *PIERS Online Journal*, vol. 5, no. 3, pp. 201-211, 2009

[50] S. Lucyszyn and Y. Zhou, "Engineering approach to modelling frequency dispersion within normal metals at room temperature for THz applications," *PIER J.*, vol. 101, pp. 257-275, Feb. 2010.

[51] http://www.ansoft.com/products/hf/hfss/

[52] http://www.cst.com/

[53] http://www.home.agilent.com/agilent

[54] http://www.rsoftdesign.com

[55] E. Episkopou, S. Papantonis, W. J. Otter, and S. Lucyszyn, "Defining material parameters in commercial EM solvers for arbitrary metal-based THz structures," *IEEE Trans. Terahertz Sci. Technol.*, vol. 2, no. 5, pp. 513–524, Sep. 2012.

[56] K. A. Norton "The physical reality of space and surface waves in the radiation field of radio antennas", *Proc. of the IRE*, vol. 25, no. 9, pp.1192-1202, Sep. 1937.

[57] S. K. Ozdemir, G. Turhan-Sayan, "Temperature effects on surface plasmon resonance: design considerations for an optical temperature sensor," *J. Lightwave Technol.*, vol. 21, no. 3, pp.805-814, Mar. 2003.

[58] E. Wijaya, C. Lenaerts, S. Maricot, J. Hastanin, S. Habraken, J.-P.Vilcot, R. Boukherroub, S. Szunerits, "Surface plasmon resonance-based biosensors: From the development of different SPR structures to novel surface functionalization strategies", *Current Opinion in Solid State and Materials Science*, vol. 15, no. 5, pp 208-224, Oct. 2011.

[59] J. Vuckovic, M. Locar, O. Painter, A. Scherer, "Surface plasmon enhanced LED," *Conf. on Lasers and Electro-Optics, 2000. (CLEO 2000)*, pp.123-124, May 2000.

[60] S. A. Maier, “Plasmonics: Fundamentals and Applications,” Springer, May 2007, ISBN 0387331506.

[61] H. Raether, “Surface Plasmons on Smooth and Rough Surfaces and on Gratings”, Springer, Dec. 1988, ISBN 3540173633.

[62] S. Lucyszyn, “Investigation of anomalous room temperature conduction losses in normal metals at terahertz frequencies”, *IEE Proc. Microw., Ant. and Propag.*, vol. 151, no. 4, pp. 321-329, Aug. 2004.

[63] B. K. Juluri, Sz-chin S. Lin, T. R. Walker, L. Jensen, and T. J. Huang, “Propagation of designer surface plasmons in structured conductor surfaces with parabolic gradient index”, *Opt. Express,* vol. 17, no. 4, pp. 2997-3006, 2009.

[64] S. A. Maier, S. R. Andrews, L. Martin-Moreno, and F. J. Garcia-Vidal, “Terahertz surface plasmon-polariton propagation and focusing on periodically corrugated metal wires”, *Phys. Rev. Lett.,* vol. 97, no. 17, Oct. 2006.

[65] G. Kumar, S. Pandey, A. Cui and A. Nahata, “Planar plasmonic terahertz waveguides based on periodically corrugated metal films”, *New J. Phys.,* vol. 13, Mar. 2011.

[66] W. J. Otter, B. P. Pirollo, R. I. Henderson and R. A. Lewis, “Multi-Octave BAVA Radiating Elements for use in Modular Phased Array Antennas”, *European Conference on Antennas and Propagation (EUCAP 2009)* Berlin, Germany, Mar. 2009.

[67] M. Rutschlin, CST Microwave Studio®, Private Support Communication, Mar. 2012.

[68] E. Episkopou, S. Papantonis, W. J. Otter and S. Lucyszyn, “Demystifying Material Parameters for THz Electromagnetic Simulations”, *4th UK/EU-China Workshop on Millimetre Wave and Terahertz Technology*, Glasgow, UK, pp. 80-81, Sep. 2011.

[69] B. Ng, S. M. Hanham, J. Wu, A. I. Fernández-Domínguez, N. Klein, Y. F. Liew, M. B. H. Breese, M. Hong, and S. A. Maier, "Broadband Terahertz Sensing on Spoof Plasmon Surfaces", *ACS Photonics,* vol. 1 no. 10, pp. 1059-1067, Sep. 2014

[70] S. Li, M. Jadidi, T. Murphy, and G. Kumar, "Terahertz surface plasmon polaritons on a semiconductor surface structured with periodic V-grooves," *Opt. Express*, vol. 21, no. 6, pp. 7041-7049, Mar. 2013.

[71] J. Grant, X. Shi, J. Alton and D. R. S. Cumming, "Terahertz surface plasmon resonance of periodic silicon micro-dot arrays", *IEEE Photonics Society Winter Topical Meeting Series (WTM)*, pp.34-35, Majorca, Spain, Jan. 2010.

[72] G. Kumar, S. Li, M. M. Jadidi and T. E. Murphy, "Terahertz surface plasmon waveguide based on a one-dimensional array of silicon pillar", *New J. Phys*., vol. 15, no. 8, Aug. 2013.

[73] J. Grant, X. Shi, J. Alton and D. R. S. Cumming "Terahertz localized surface plasmon resonance of periodic silicon microring arrays", *J. App. Phys.*, vol. 109, no. 5, Mar. 2011.

[74] L. Shanshan, M. M. Jadidi, T.E. Murphy and G. Kumar, "Plasmonic Terahertz Waveguide Based on Anisotropically Etched Silicon Substrate," *IEEE Trans. Terahertz Sci. Technol*., vol.4, no.4, pp.454-458, Jul. 2014.

[75] Resistivity and Carrier Transport Parameters in Silicon, Virginia Semiconductors Inc. http://www.virginiasemi.com/pdf/resistivitycarriertransportinsilicon.pdf

[76] http://ecee.colorado.edu/~bart/book/effmass.htm

[77] A. Otto. "Excitation of nonradiative surface plasma waves in silver by the method of frustrated total reflection", *Z. Physik*, vol. 216 no. 4, pp. 398-410, 1968.

[78] E. Kretschmann, and H. Reather, "Radiative decay of nonradiative surface plasmon excited by light", *Z. Naturf.* vol. 23, pp. 2135–2136, Nov. 1968.

[79] W. Wood, “On a Remarkable Case of Uneven Distribution of Light in a Diffraction Grating Spectrum”, *Proc. Phys. Soc. London*, vol. 18, no. 1, pp. 269-275, Jun. 1902

[80] http://upload.wikimedia.org/wikipedia/commons/2/2a/Prism_Coupler.png

[81] F. Wahaia, G. Valusis, L. M. Bernardo, A. Almeida, J. A. Moreira, P. C. Lopes, J. Macutkevic, I. Kasalynas, D. Seliuta, R. Adomavicius, R. Henrique and M. Lopes, “Detection of colon cancer by terahertz techniques”, *J. of Molecular Structure*, vol. 1006, no. 1–3, pp. 77-82, Dec. 2011.

[82] M. Levinshtein and G. Simin, “Transistors: From Crystals to Intergrated Circuits,” World Scientific Publishing Co Pte Ltd, Oct. 1996, ISBN 9810227434.

[83] A. Poglisch, C. Waelkiens, O. Bauer, J. Cepa, H. Feuchtgruber, T. Henning, C. van Hoof, F. Kerschbaum, D. Lemke, E. Renotte, L. Rodriguez, P. Saraceno and B. Vandenbussche, “The photodetector array camera and spectrometer (PACS) for the Herschel Space Observatory” *Proc. SPIE,* vol. 6265, May 2006.

[84] P. Kaufmann, R. Marcon, A. Marun, A. S. Kudaka, E. Bortolucci, M. B. Zakia, J. A. Diniz, M. M. Cassiano, P. Pereyra, R. Godoy, A. V. Timofeevsky, V. A. Nikolaev, A. M. Pereira, Alves da Silva and L. O. T. Fernandes, “Selective spectral detection of continuum terahertz radiation,” *Proc. SPIE,* vol.7741, Jul. 2010.

[85] B. Voisiat, A. Bičiūnas, I. Kašalynas and G. Račiukaitis, “Band-pass filters for THz spectral range fabricated by laser ablation”, *Appl. Phys. A*, vol. 104, no. 3, pp. 953-958, May 2011.

[86] P. A. R. Ade, G. Pisano, C. Tucker and S. Weaver, “A review of metal mesh filters”, *Proc. SPIE,* Vol 6275, Jun. 2006.

[87] http://www.terahertz.co.uk/index.php?option=com_content&view=article&id=280&Itemid=628#BP

[88] http://www.lakeshore.com/documents/metal-mesh-optical-filter-technology.pdf

[89] F. Pavanello, F. Garet, M-B. Kuppam, E. Peytavit, M. Vanwolleghem, F. Vaurette, J-L. Coutaz and J-F. Lampin, "Broadband ultra-low-loss mesh filters on flexible cyclic olefin copolymer films for terahertz applications" *Appl. Phys. Lett.*, vol. 102, no. 11, Mar. 2013.

[90] B. A. Munk "Frequency Selective Surfaces: Theory and Design" *John Wiley & Sons Inc.,* Jan. 2005, ISBN: 9780471370475.

[91] Y. Wang, B. Yang, Y. Tian, R. S. Donnan, M. J. Lancaster, "Micromachined thick mesh filters for millimeter-wave and terahertz applications," *IEEE Trans. Terahertz Sci. Technol*., vol. 4, no. 2, pp. 247-253, Mar. 2014.

[92] A. M. Melo, A. L. Gobbi, M. H. O. Piazzetta, and A M. P. A. da Silva, "Cross-shaped terahertz metal mesh filters: Historical review and results", *Adv. in Opt. Technol.*, Jan. 2012.

[93] O. Paul, R. Beigang, and M. Rahm, "Highly selective terahertz bandpass filters based on trapped mode excitation", *Opt. Express*, vol. 17, no. 21, pp. 18590-18595, Oct. 2009.

[94] G. A. Siles, J. M. Riera and P. García-del-Pino, "THz propagation research within the TERASENSE project: Atmospheric gases attenuation", *European Conf. on Ant. and Prop. (EUCAP 2010)*, Barcelona, Spain, Apr. 2010.

[95] C. Duque, M. A. Ribeiro, "Effect of uniaxial compression in the transmittance of a novel terahertz sensor for structural health monitoring," *Loughborough Ant. and Propagation Conf.* (LAPC), Loughborough, UK, Nov. 2013.

[96] J. D. Joannopoulos, S. G. Johnson, J. N. Winn & R. D. Meade "Photonic Crystals: Molding the Flow of Light" Princeton University Press, Second edition, 2008, ISBN: 9780691124568.

[97] E. Yablonovitch, "Inhibited Spontaneous Emission in Solid-State Physics and Electronics", *Phys. Rev. Lett.*, vol. 58, no. 20, pp. 2059–2062, May 1987.

[98] S. John, "Strong localization of photons in certain disordered dielectric superlattices" *Phys. Rev. Lett.*, vol. 58, no. 23, pp. 2486–2489, Jun. 1987.

[99] J. W. S. Rayleigh, "On the remarkable phenomenon of crystalline reflexion described by Prof. Stokes", *Phil. Mag,* vol. 26, no. 160, pp. 256–265, 1888.

[100] E. Özbay, "Layer-by-layer photonic crystals from microwave to far-infrared frequencies," *J. Opt. Soc. Am. B*, vol. 13, no. 9, 1945-1955, Aug. 1996.

[101] W. Zheng, M. Xing, W. Chen, W. Zhou, A. Liu, H.Wang and L. Chen, "Demonstration of high efficient tunable lasing with one photonic crystal W1 waveguide," *Conf. on Lasers & Electro Optics & The Pacific Rim Conf. on Lasers and Electro Optics* (CLEO/PACIFIC RIM '09), Shanghai, China, Aug. 2009.

[102] K. Rivoire, S. Buckley, and J. Vučković, "Multiply resonant high quality photonic crystal nanocavities", *App. Phys. Lett*, vol. 99, Jul. 2011.

[103] S. Lin, E. Chow, J. Bur, S. Johnson, and J. Joannopoulos, "Low-loss, wide-angle Y splitter at approximately ~1.6- μm wavelengths built with a two-dimensional photonic crystal," *Opt. Lett*., vol. 27, no. 16, pp. 1400-1402, Aug. 2002.

[104] P.H. Bolivar, M. Brucherseifer, J. Gómez Rivas, R. Gonzalo, I. Ederra, A.L. Reynolds, M. Holker, P. de Maagt, "Measurement of the dielectric constant and loss tangent of high dielectric-constant materials at terahertz frequencies," *IEEE Trans. Microw. Theory & Tech.*, vol. 51, no. 4, pp.1062-1066, Apr. 2003.

[105] S. Kumar, "Design and Fabrication of Micromachined Silicon Suspensions", PhD Thesis, Imperial College London, 2007.

[106] S. G. Johnson, *MIT Photonics-Bands (MPB)*. Available: http://ab-anitio.mit.edu/wiki/index.php/MIT_Photonic_Bands

[107] S. Hadzialic, S. Kim, A.S. Sudbo and O. Solguard "Two-dimensional photonic crystals fabricated in monolithic single-crystal silicon" *IEEE Photon. Technol. Lett.,* vol. 22, no. 2, pp. 67–69, Jan. 2010.

[108] J. Schobel, T. Buck, M. Reimann, M. Ulm and M. Schneider, "W-band RF-MEMS subsystems for smart antennas in automotive radar sensors," *34th European Microwave Conference*, vol. 3, pp. 1305-1308, Amsterdam, Netherlands, Oct. 2004.

[109] G. M. Rebeiz and J. B. Muldavin, "RF MEMS switches and switch circuits," *IEEE Microw. Mag.*, vol. 2, no. 4, pp. 59-71, Dec 2001.

[110] L. Kwanhim D. Hanyi L. Xuefeng B. A. Orner, J. Rascoe, B. Dewitt, E. Mina, and B. Gaucher, "Wideband millimeter wave pin diode SPDT switch using IBM 0.13µm SiGe technology," *European Microwave Integrated Circuit Conference (EuMIC 2007*), pp. 108-111, Munich, Germany, Oct. 2007

[111] SERIES PSP Product Brouchure Millitech http://www.millitech.com/pdfs/specsheets/IS000043-PSP.pdf

[112] Y. Zhou and S. Lucyszyn, "Modelling of reconfigurable terahertz integrated architecture (RETINA) SIW structures", *PIER Journal,* vol. 105, pp. 71-92, Jun. 2010.

[113] Platte, Walter; Sauerer, B., "Optically CW-induced losses in semiconductor coplanar waveguides," *IEEE Trans. Microw. Theory & Tech.*, vol. 37, no. 1, pp. 139,149, Jan. 1989

[114] B. Temelkuran, M. Bayindir, E. Ozbay, J. Kavanaugh, M. Sigalas and G. Tuttle, "Quasimetallic silicon micromachined photonic crystals," *Appl. Phys. Lett.,* vol. 78, no. 3, Jan. 2001.

[115] G. Annino, M. Cassettari, I. Longo and M. Martinelli, "Whispering gallery modes in a dielectric resonator: Characterization at millimeter wavelength," *IEEE Trans. Microw. Theory Tech.*, vol. 45, no. 11, pp. 2025-2034, Nov. 1997.

[116] M. Nagel, P. H. Bolivar, and H. Kurz, "Modular parallel-plate THz components for cost-efficient biosensing systems," *Semiconduct. Sci. Technol.*, vol. 20, pp. S281–S285, Jun. 2005.

[117] T. Driscoll, G. O. Andreev, D. N. Basov, S. Palit, S. Y. Cho, N. M. Jokerst, and D. R. Smith, “Tuned permeability in terahertz split-ring resonators for devices and sensors”, *Appl. Phys. Lett.* vol. 91, no. 6, 062511, Aug. 2007.

[118] B. Ng, S. M. Hanham, V. Giannini, Z. Chen, M. Tang, Y. Liew, N. Klein, M. Hong, S. A. Maier, "Lattice resonances in antenna arrays for liquid sensing in the terahertz regime," *Opt. Express,* vol. 19, no. 15, pp. 14653-14661, Jul. 2011.

[119] P. George, C. Manolatou, F. Rana, A. L. Bingham and D. Grischkowsky, “Integrated waveguide-coupled terahertz microcavity resonators,” *Appl. Phys. Lett.,* vol 91, no. 19, p. 191122, Nov. 2007.

[120] Y. Zhao and D. Grischkowsky, “2-D terahertz metallic photonic crystals in parallel-plate waveguides,” *IEEE Trans. Microw. Theory Tech.,* vol. 55, no. 4, pp. 656-663, Apr. 2007.

[121] Y. Akahane, T. Asano, B. Song and S. Noda, “High-Q photonic nanocavity in a two-dimensional photonic crystal,” *Nature*, vol. 425, pp. 944-947, Oct. 2003.

[122] D. Englund, I. Fushman and J. Vučković “General recipe for designing photonic crystal cavities” *Opt. Express*, vol. 13, no. 16, pp. 5961–5975, Aug. 2005.

[123] D. Kajfez and P. Guillon “Dielectric Resonators” *SciTech Publishing Inc*. 2nd Edition, 1998, ISBN 1884932053.

[124] J.W. Lamb, “Miscellaneous data on materials for millimetre and submillimetre optics”, *Int. J. Infrared Millimet. Waves*, vol. 17, no. 12, pp. 1997–2034, Sep. 1996.

[125] G.F. Engen and C.A. Hoer “Thru-Reflect-Line: an improved technique for calibrating the dual six-port automatic network analyser”, *IEEE Trans. Microw. Theory Tech.*, vol. 12, no. 12, pp. 987–993, Dec. 1979.

[126] A. Rumiantsev and N.M. Ridler “VNA calibration”, *IEEE Microw. Mag.,* vol. 9, no. 3, pp. 86–99, Jun. 2008

[127] N.M. Ridler "A review of existing national measurement standards for RF and microwave impedance parameters in the UK", *IEE Colloq. (1999) Dig.,* no. 99/008, pp 6/1–6/6, Feb. 1999.

[128] N.M. Ridler "News in RF Impedance Measurement" *XXVIIth General Assembly of the International Union of Radio Science (URSI)*, Maastricht, Netherlands, 2002.

[129] G.J. French and N.M. Ridler "A primary national standard for millimetric waveguide S-parameter measurements" *Microw. Eng. Eur.*, pp. 29–32, Oct. 1999.

[130] "High Resistivity (HiResTM) Silicon for GHz and THz Technology", Application note version 1.1, Topsil, Jan. 2014.

[131] "Guidelines of the Evaluation of Vector Network Analysers (VNA)", *EURAMET* cg-12 Version 2.0, Mar. 2011.

[132] "JCGM 100:2008, Evaluation of measurement data – Guide to the expression of uncertainty in measurement" (First ed.) http://www.bipm.org, Sep. 2008.